Design and Investigation of the Use of TEM Cells in the Characterization ofUnderground Targets

Ali Al Takach

THÈSE

Pour obtenir le grade de

DOCTEUR DE L'UNIVERSITE GRENOBLE ALPES

Spécialité : **OPTIQUE ET RADIOFREQUENCES**

Arrêté ministériel : 25 mai 2016

Présentée par

Ali AL TAKACH

Thèse dirigée par **Fabien NDAGIJIMANA, Professeur, Université Grenoble Alpes**,
et codirigée par **Jalal JOMAAH**
et **Mohammed AL-HUSSEINI**

préparée au sein du **Laboratoire de Génie Electrique**
dans **l'École Doctorale Electronique, Electrotechnique, Automatique, Traitement du Signal (EEATS)**

Conception et enquête de l'utilisation de cellules TEM dans la caractérisation de cibles souterraines

Design and Investigation of the Use of TEM Cells in the Characterization of Underground Targets

Thèse soutenue publiquement le **6 décembre 2019,**
devant le jury composé de :

Madame Geneviève Duchamp
Professeur, IMS Université de Bordeaux, Présidente
Madame Geneviève Mazé-Merceur
Ph.D, CEA Cestas, Invitée
Monsieur Serge Verdeyme
Professeur, Université de Limoges, Rapporteur
Monsieur Moncef Kadi
HDR, ESIGELEC Rouen, Rapporteur
Monsieur Fabien NDAGIJIMANA
Professeur, Université Grenoble Alpes, Directeur de thèse
Monsieur Jalal Jomaah
Maître de Conférences, Grenoble INP, Co-directeur de thèse
Monsieur Mohammed Al-Husseini
Ph.D., Beirut Research and Innovation Center, Co-encadrant de thèse

Acknowledgments

First and foremost, I would like to thank God Almighty.

I would like to express my sincere gratitude to my advisors Prof. Fabien Ndagijimana, Prof. Jalal Jomaah and Dr. Mohammed Al-Husseini for the continuous support of my Ph.D. study and related research.

Besides my advisors, I would like to thank the rest of my thesis committee: Prof. Genevieve Duchamp, Prof. Serge Verdeyme, Dr. Genevieve Maze-Merceur, and Dr. Moncef Kadi for their insightful comments and encouragement. Also for the hard question which incented me to widen my research from various perspectives.

My sincere thanks also go to Prof. Hassan Ghaziri, who believed in my abilities and provided me an opportunity to join his research team. Without his precious support, it would not be possible to conduct this research.

Also, I thank my friends in the following institution: Beirut Research and Innovation Center (BRIC), CSTB Pheline and G2Elab.

Last but not least, I would like to thank my family: my parents, my sisters and my brother for supporting me throughout my life. I would like also to take the opportunity to express my love to my spouse who stood by my side during the good and the bad times.

Table of Contents

List of Figures

List of Tables

List of Abbreviations

BRIC: Beirut research and innovation center

HDRP: humanitarian demining research program

UXO: unexploded ordnances

GPR: ground penetrating radar

TEM: transverse electromagnetic

MAG: mine action center

NMR: nuclear magnetic resonance

NQR: nuclear quadrupole resonance

EM: electromagnetic

LIDAR: light detection and ranging

IR: infrared

MD: metal detector

CW: continuous wave

FMCW: frequency modulated continuous wave

SFMCW: stepped frequency modulated continuous wave

RF: radio frequency

MUT: material under test

VNA: vector network analyzer

SOLT: short open load thru

TRL: thru reflect line

SO: short open

WCM: wave cascading matrix

CST: computer simulation technology

NRW: Nicolson-Ross-Weir

MW: microwave

EMC: electromagnetic compatibility

ABS: acrylonitrile butadiene styrene

PLA: polylactic acid

IC: integrated circuit

EUT: equipment under test

RCTL: rectangular coaxial strip line

FDTD: finite difference time domain

DUT: device under test

VSWR: voltage standing wave ratio

TE: transverse electric

TM: transverse magnetic

FDM: fused deposition modeling

CNC: computer numerical control

PCB: printed circuit boards

General Introduction

Landmines are examples of the devastating consequences of war. Even if armed conflicts stop right now, it would take years before clearing the lands that have been contaminated with mines. This results in more human casualties, who fall indiscriminately, and in the hindering of the social and economic wellbeing of those living in these areas. Thousand of people killed and injured each year and hundreds of thousands of population are living under the risk of losing their life, their children or their limbs. Treatment of injuries is often costly, both psychologically and physically. On the other side, hundreds of kilometers around the world are still contaminated with landmines, and an increase in the contaminated area is expected due to the renewed conflicts in different zones. This issue deprives society of investing in these polluted lands. This humanitarian problem has necessitated the intervention of many countries, associations and non-governmental organizations involved in humanitarian work to help reduce the negative effects of the proliferation of mines through technical and logistical support for demining operations.

Since decades the scientific researchers are developing methods to detect the presence of landmines. These methods are belonging to a different field of sciences such as biology, chemistry, and physics. During the past years, the human succeeded to detect the explosives by trained several types of animals, uses a specific kind of plants, make use of the nuclear interaction. In addition, with the use of acoustic, infrared, and electromagnetic sensors he becomes able to image the gound subsurfaces in order to detect the landmines. In spite of the huge development in the methods of detection, there is no method that works ideally with all conditions, all of them have advantages and limitations.

Beirut Research and Innovation Center (BRIC) has launched in 2013 the humanitarian demining research program (HDRP). This research program aims to implement technologically-advanced solutions for the detection and localization of landmines and unexploded ordnances (UXO). The investigated solutions are based on the advanced usage of electromagnetic waves, networks of biosensors, and/or intelligent metal detectors, and are expected to be safer, faster, and less expensive compared to the conventional demining techniques. They should help decrease the number of mines/UXOs casualties and lead to the earlier recovery of the contaminated lands. So, the presented Ph.D. research work is a part of the HDRP project concerned in the enhancement of the electromagnetic technique for landmine detection.

Indeed, the electromagnetic methods represented by the metal detector and the ground penetrating radar are considered as the most efficient and practical methods. The metal detector can sense the metal part exists in the landmine or in the soil, but its detection ability fails when the landmine has no metal part or even has a very small amount of metal. Whereas, the GPR can sense any anomaly in the soil based on the variation in the relative permittivity of the material. The use of GPR for landmine detection is being more attractive and prove good performance. Despite their advantages, GPR has some limitations for example inability to detect buried landmine at shallow depth due to the signal masking by the soil surface effect, inefficient in inhomogeneous soil, and in wet soil.

In the fact that the GPR responses are directly related to the electrical properties of the material under-scan, the effective electrical properties of the buried landmines with its surrounding soil is studied for a better understanding of the interaction between an electromagnetic wave and material.

This thesis report is composed of five chapters, the first chapter is dedicated to literature review covering different aspects related to the presented research work. In order to show the motivation of this work the problem of landmines is reported, after that the potential solutions for landmines detection were presented, and due to the good reputation of the electromagnetic methods the brief description of the electromagnetic theory is stated followed by the general explanation of the GPR concept wich considered as one of the most advanced techniques in current use.

In the second chapter, and with the purpose of extracting the electrical properties of dielectric materials the microwave methods for material characterization are discussed. At the beginning of this chapter the different characterization methods are classified, then two different measurement calibrations are described and numerically validated. Furthermore, several conversion methods were presented in detail. In addition, two characterization methods are not required calibrated S parameters were written also in particulars. Afterward, a numerical comparison was made for extracted permittivity and their error based on various characterization methods. At the end of this chapter some materials related to our applications were characterized such as soil, sand, and plastic.

In the third chapter, the theoretical background of the transverse electromagnetic (TEM) cell and its traditional use were described. On the other side, the first 3D printed lightweight and low-cost TEM cell was fabricated in this work. As long as the effective permittivity of the landmine with its surrounding soils needs a relatively big test fixture with insertion easiness property for doing the characterization measurements, the closed TEM cell was attempted for the first time in material characterization applications. Subsequently, two different types of antipersonnel landmines were effectively characterized in the presence of different soil conditions.

In the fourth chapter, a nondestructive method for permittivity extraction is presented based on the use of the GPR. A numerical parametrical effects study was done to obtain the optimal parameters of the GPR system for accurate permittivity extraction including antenna types, operational frequency band, a separation distance between antennas and elevation distance of the antennas from the ground surface.

In the fifth chapter, a novel approach for landmine detection was proposed for covering some disadvantages that exist in the traditional use of the GPR system. The new concept uses the effective permittivity of landmine with its neighboring material as a signature for detection purposes. Relying on the development use of the TEM cell in material characterization and the homogenization concept the effective permittivity of the complex targets is possible to be measured. Furthermore, a detection scenario of buried landmine is presented using the GPR system as permittivity sensor.

In the end, a general conclusion for the research work achieved in this thesis is reported in addition to some perspectives.

Chapter 1: Literature Review

Contents

1.1 INTRODUCTION

This research work employs different technological fields of study in the enhancement of humanitarian demining labor. In this chapter the basics information to figure out the problem is presented. The landmine problem and its effect on human life is highlight in order to show the importance of this kind of humanitarian research work. Diverse methods for landmines detection are discussed in this chapter. The electromagnetic methods attract the most attention due to their efficiency in the detection comparing to other methods. The needed electromagnetic theory in this work is briefly reported. In addition, the GPR system is described since it will be used later in the landmine detection.

1.2 LANDMINE PROBLEM

Peace agreements may be signed and hostilities may cease, but landmines are an enduring legacy of conflict [1]. Antipersonnel landmines are explosive devices designed to be detonated by the presence, proximity, or contact of a person [2]. Whereas, Antivehicle (antitank) landmines are munitions designed to explode from the presence, proximity, or contact of a vehicle [1]. The Landmines can be placed under or on the ground, they can lie dormant for years and even decades [3]. Incapable of distinguishing between the footfall of a soldier and that of a child, antipersonnel mines cannot be aimed. They indiscriminately kill or injure civilians, aid workers, peacekeepers, and soldiers alike [3]. They pose a threat to the safety of civilians during conflicts and long afterwards [1].

The antipersonal landmine is basically made of plastic, metal, and explosives. They fit into three main types (i.e., Blast, Fragmentation, and Bounding Fragmentation). Blast landmines are buried close to the soil surface and required about 5 to 16 kg to be exploded. These mines aim to cut person’s leg and causing dangerous infections. Fragmentation landmines release metal or glass fragments in one or all directions for long distances in order to hit the victim with deep wounds. Bounding Fragmentation landmines are not buried totally in the ground, after their activation they spring up about 1 meter and then explode to cause injuries at the head and chest level [3][4].

These weapons can be found on roads, footpaths, farmers’ fields, forests, deserts, along borders, in and surrounding houses and schools, and in other places where people are carrying out their daily activities. They deny access to food, water, and other basic needs, and inhibit freedom of movement. They endanger the initial flight and prevent the repatriation of refugees and internally displaced persons, and hamper the delivery of humanitarian aid. These weapons instill fear in communities, whose citizens often know they are walking in mined areas, but have no possibility to farm other lands, or take another route to school. When land cannot be cultivated, when medical systems are drained by the cost of attending to landmine casualties, and when countries must spend money clearing mines rather than paying for education, it is clear that these weapons not only cause appalling human suffering but that they are also a lethal barrier to sustainable development and post-conflict reconstruction [1].

More than sixty countries suffer from landmines contamination as shown in Figure 1.1.

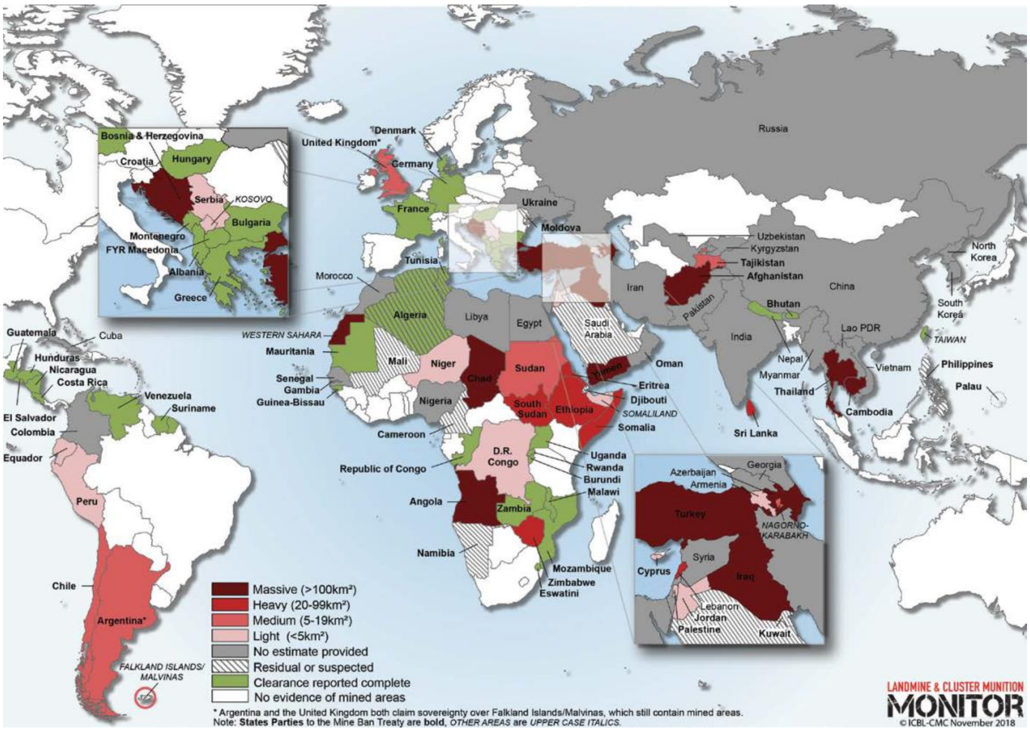

Figure 1.1 Worldwide mine contamination status 2018 [1]

According to the Mine Action Center (MAG) 20 people are killed or injured by these indiscriminate weapons every day and almost half of them are children.

Referring to the Landmine Monitor Report 2018, 168000 antipersonal mines were destroyed and the area of 128 km^2 was cleared in 2017. In addition, around 7239 casualties were identified. It is certain that there are additional casualties each year that are not captured. Nobody knows how many mines are in the ground worldwide but the actual number is less important than their impact [3].

1.3 LANDMINE DETECTION METHODS FOR HUMANITARIAN DEMINING

1.3.1 Explosive vapor sensors

In spite of burying the landmines in the ground, its explosive material still releases a very little amount of particles to the surrounding environment through landmine’s cracks or its plastic body (casing). Moreover, 95% of the leaked explosive will adsorb the surrounding soil while the remaining amount will dissolute in the existing water in the soil. Some of these explosive particles will flow to the soil surface in a vapor form [5]. Hence, the detection of the landmines is now possible by employing any sensor that can distinguish if the sensed vapors are belonging to explosive material or not.

This method can be divided into two main sensors category, including both biological or chemical.

The biological method is based on the detection of the explosive compound using the sensitive sniffing power of some animals such as dogs and rates. In addition, it is possible to train the insects (e.g., honey bees and ants) on the landmine detection. Furthermore, special bacteria or plants could be also employed for explosive detection [6][7].

The chemical methods mainly concentrate on the detection of vapors from the explosives like TNT, PET and RDX. By using techniques like molecular diffusion and turbulence processing, these vapors can be transported. The objective of this method is to create some sensors that can identify the explosive vapors by employing electromechanical, espectorpial or piezoelectric principles. But as the sensitivity towards vapor detection of such sensors is very low, detection of mines becomes very difficult [6].

1.3.2 Mechanical

The mechanical method can be divided into two main parts instrumented prodder and mine clearing machines.

Instrumented Prodder:

It is a manual method that rely on direct physical contact with the ground. The deminer uses a probe that could be inserted into the ground with an angle of 30^0. The probe is supported with acoustic or electromagnetic technology for making special measurements during the insertion. These measurements can give an idea about the nature of the object being investigated. This kind of method relies on the dexterity of the deminer [8].

Mine Clearing Machines:

In some situations, the minefield has to be cleared within a short time and usually that happens with the military forces. For this purpose, several machines can be employed to clear out or detonate mines by rolling through the minefield. The new machines are remotely controlled and that is an advantage in minimizing the risk of deminer life. This method has several limitations such as destroying the area under clearance, some mines can be missed, cannot achieve the humanitarian demining accuracy, and it is not environmentally friendly [8].

1.3.3 Nuclear

Nuclear Magnetic Resonance (NMR):

This technique is working properly if the target is located inside the detecting coil. Unfortunately, in buried mines case the NMR is not efficient in detection since the resulting DC and RF fields are relatively weak and non-uniform. Furthermore, this technique needs a cooling system and a source of high power, and that making this technique unsuitable for hand-held detectors. Also, NMR would not be able to detect metallic mines and would have to be used in conjunction with a metal detector [4].

Nuclear Quadrupole Resonance (NQR):

Based on the resulting oscillation in the spinning property (quadrupole moment) of the nitrogen atom nuclei which is existed in the explosives (e.g., TNT and RDX) if an EM pluses impinging on it, the presence of explosive is detected. Unfortunately, NQR is affected by EM interfering, distance between sensor and target, and temperature. In addition, the signal-noise-ratio is very low in this method [6][7].

Neutron-Based Technique:

This technique uses a continuous or pulsed neutron source to bombard the ground. Due to the interaction between the explosive material and the neutrons a gamma and X rays will be generated. The generated radiations are sensed by a detector in order to take the detection decision. The drawbacks of this technique are the high power consumption, the radiation hazards, and the weight the dense shielding required [8].

1.3.4 Acoustic

Acoustic technique uses a sound or ultrasound wave to penetrate the ground as a mechanical disturbance of molecules in the form of waves. The sound wave will be reflected on the interface between materials having different acoustical properties [8]. The reflected acoustic waves are collected to locate and identify the target. The wave penetration is related to the soil density. The main limitations of this technique are the attenuation at the air soil interface, measurement difficulty when there is a vegetation on the soil surface, and sometimes the pressure needed for better sensing of the reflected waves [7][8].

1.3.5 Optical

At optical wavelength band the penetration depth of the EM wave into the ground is very poor so the optical techniques can see the landmines influence at the soil surface. We will introduce briefly two methods used in the optical technique for landmines detection. The methods are the visible light and light detection and ranging (LIDAR) [8].

Visible Light:

The landmines detection can be achieved by capturing light waves of visible wavelengths using an imaging optical system. Large area can be scanned within a short time by mounting this system on an airborne setup. There are limitations for this method including the sensitivity to camouflage, foliage, and vegetation. In addition, it cannot detect buried targets [8].

LIDAR:

The LIDAR is an optical technology that based on the illumination of ground surface by pulses of light that is linearly polarized. The reflected energy can be used to extract information relating to the target such as location and absorption property. Furthermore, the LIDAR systems can detect the polarization changes in the received energy and consequently the landmine can be detected. As the visible light method the LIDAR method is not be able to detect buried object and its detection is inefficient in the ground with vegetation. In addition to that their range and sensitivity are limited due to the low reflected signal strength [8].

1.3.6 Infrared

The infrared (IR) range is a part of the EM spectrum located between the visible rays and microwave region with wavelengths between 0.75 μm and 1 mm [8]. Due to the fact that any object emits a specific IR radiation related to its temperature and thermal property [4], the detection of the landmines becomes possible if the IR radiation of mines is different enough from its surrounding medium. The IR radiation of the target can be affected by normal factors such as weather conditions, time of the day, and the background environment. Or it could be affected by an intended heat source that aims to raise the RI radiation contrast between the mine and its surrounding soil [4]. IR sensors have trouble to detect deep mines at depth more than 10 cm and its inefficient in the area that has vegetation [7].

1.3.7 Electromagnetic

Metal detector:

The metal detector (MD) technique uses the electromagnetic induction (EMI) principle to detect the buried landmines that having metal parts. The MD consist of two coils one to generate a magnetic field (transmitter) and the other to sense the resulting magnetic field (receiver) [8]. Due to the time-varying current in the main coil, an EM field will propagate in the environment. Once the EM field encounters any metal object an eddy current will be induced in the metal surface of the object. This current, in turn, will create a new EM field that will be sensed at the secondary coil as a time-varying current in the opposite direction. By amplifying and processing this current the metal target can be detected. The main advantages of the MD are: very efficient in detecting buried landmines made of metal, and it is impervious to the weather conditions and soil moistening. The MD disadvantages are the detection inability of modern plastic mines or mines with small amount of metal, the high rate of the false alarms due to the presence of metal clutters makes the landmine detection task to be slow and costly [6][7].

Ground penetrating radar:

The concept of this technique is to transmit short radio and microwave radiation pulses from an antenna into the ground and measuring the reflected returned signal versus time [8]. The reflections occur when the propagated EM wave goes through an interface of two different mediums having different electrical properties. The processing of these reflected signals can lead to detect and locate the buried targets. Indeed, lower frequencies provide deep penetration in the ground with low detection resolution whereas lower penetration and higher detection resolution provided using higher frequencies [4]. In addition to the operating frequency, the conductivity of the ground is the main factor that affects the detection depth (EM attenuation). The latest technology working on this principle is ground penetrating radar (GPR). It is a promising technology that can be used for the detection of metallic as well as plastic mines from a safe distance [6].

1.3.8 Detection methods comparison

There is no perfect method for all conditions, the selection of the method is related to different factors. In the table below the detection methods were compared in terms of different properties.

Table 1-1 Detection methods comparison [7]

Technique	**Sensors**	**Complexity**	**Cost**	**Speed**	**Safety**	**Environment effect**	**False alarm**
Electromagnetic	MD GPR	Low Medium	Low High	Low Medium	High High	Low Medium	High Low
Biological	Dogs Plants Bacteria	Low Medium Medium	Medium Medium Medium	Medium Low High	Medium High Low	Medium High High	Medium High Low
Optical	Light LIDAR	Low High	Low High	Medium Medium	High High	High Low	High Medium
Nuclear	NQR Neutron	High High	Medium High	Medium High	Medium Low	High Low	Low Medium
Acoustic	A/S US	Medium Medium	High Medium	Medium Low	High High	Medium Medium	Low High
Mechanical	Prodders Machine	Low Medium	Low Low	Medium High	Low Low	Low Low	High High

1.4 ELECTROMAGNETIC THEORY

1.4.1 Electromagnetic field

The Electric (E) field is generated by an electrical charge while the Magnetic (H) field is formed by the movement of an electric charge. The electromagnetic (EM) field is a combination of E and H fields orthogonal to each other propagated in the free space at the speed of light. The EM waves are mainly characterized by the frequency, period, and wavelength. The frequency which is the number of oscillations at a given point during one second, it is denoted by f and expressed in hertz (Hz). The period is denoted by T and expressed in seconds (s), and it is defined as the inverse of the frequency with the relation: T=1/ f. The wavelength is the distance that separates two corresponding points of oscillation. It characterizes, in particular, the distance between two nodes or two valleys of a wave. It is denoted by λ and expressed in meters (m). This quantity is inversely proportional to the frequency in the vacuum. It is related to the frequency and the speed of propagation of the light c by the relation: $\lambda = c / f$. The EM wave representation is shown in Figure 1.2.

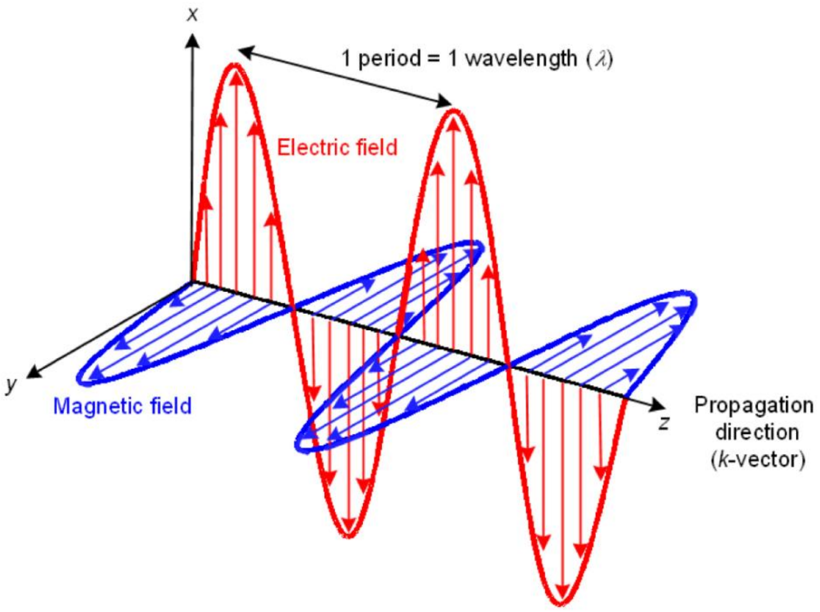

Figure 1.2 Schematic representation of an EM wave

The EM fields are all around us everywhere, these waves can be created by natural sources such as the sun, thunderstorms, and earth. Or from human-made sources such as TV antennas, Radars, mobile phones, and X-ray scanner. The EM filed radiations are basically divided into two categories non-ionizing radiations and ionizing radiations which are respectively the lower frequencies ending at ultraviolet range and the higher frequencies begin with the x-ray range. Ionizing radiation has enough energy to free electrons from the atoms or molecules they are attached to, and therefore ionizing them. Non-ionizing radiation lacks the energy to break these same molecular bonds and cannot free electrons from atoms or molecules [9]. InFigure 1.3, the electromagnetic spectrum and their range allocations are exhibited.

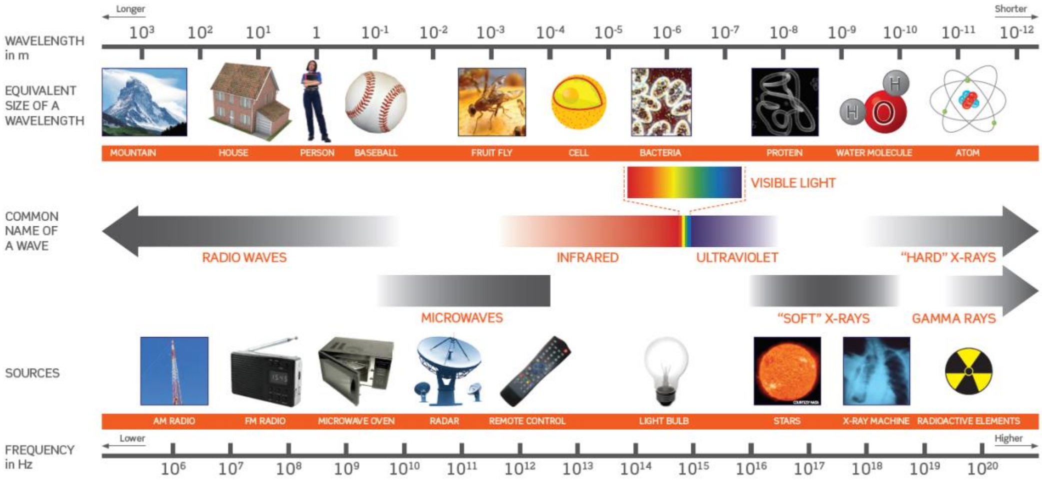

Figure 1.3 Electromagnetic spectrum [10]

1.4.2 Maxwell equations

In 1873 James Clerk Maxwell describe mathematically the electric and magnetic fields relation that explains the electromagnetic phenomena at macroscopic scale [11]. Based on Gauss, Ampere, and others' empirical and theoretical knowledge development, Maxwell uses his geniality in mathematics to write the fundamental equations of electromagnetic. The equations can be represented in several forms, below the differential form of Maxwell equations is presented.

$$\nabla \times \vec{E} = -\frac{\partial \vec{B}}{\partial t} \tag{1.1}$$

$$\nabla \times \vec{H} = \vec{J} + \frac{\partial \vec{D}}{\partial t} \tag{1.2}$$

$$\nabla \bullet \vec{D} = \rho \tag{1.3}$$

$$\nabla \bullet \vec{B} = 0 \tag{1.4}$$

Where $\vec{E}$ is the electric field, in volts per meter (v/m); $\vec{H}$ is the magnetic field, in amperes per meter (A/m); $\vec{D}$ is the electric flux density, in coulombs per meter squared (Coul/m^2); $\vec{B}$ is the magnetic flux density, in webers per meter squared (Wb/m^2); $\vec{J}$ is the electric current density, in amperes per meter squared (A/m^2); ρ is the electric charge density, in coulombs per meter cubed (Coul/m^3).

The material interaction with an electromagnetic field can be described by the following constitutive equations:

$$\vec{J} = \sigma \vec{E} \tag{1.5}$$

$$\vec{D} = \varepsilon \vec{E} = \left(\varepsilon_0 \varepsilon_r\right) \vec{E} \tag{1.6}$$

$$\vec{B} = \mu \vec{H} = \left(\mu_0 \mu_r\right) \vec{H} \tag{1.7}$$

Where ε_0 is the permittivity of vacuum, 8.89×10^{-12} farad/m; μ_0 is the permeability of the vacuum, $4\pi \times 10^{-7}$ henry/m; $\varepsilon_r = \varepsilon_r^{'} - j\varepsilon_r^{''}$ is the relative complex permittivity of the material; $\mu_r = \mu_r^{'} - j\mu_r^{''}$ is the relative complex permeability of the material, and σ is the electric conductivity of the material.

1.5 TWO PORT NETWORK

In general, the microwave system can have one, two, or multiport networks. In this section, we will focus on the two-port network since it is the most common case and its concept can be extended to apply for multiport networks.

Different matrixes parameters are used to deal with a two-port network such as impedance and admittance matrixes which are relating the voltages and currents of the network. But due to their limitations in measurement at higher frequencies another network representation can be used as the scattering matrixes parameters which link the incident and reflected voltage waves at the ports [11].

Figure 1.4 Two-port network representation with voltages and currents [12]

In Figure 1.4, the general configuration of a two-port network is displayed. Where V_1^+ and V_1^- are the forward and reverse traveling waves of a voltage signal associated with port 1. As well, for port 2.

$$\begin{pmatrix} V_1^- \\ V_2^- \end{pmatrix} = \begin{pmatrix} S_{11} & S_{12} \\ S_{21} & S_{22} \end{pmatrix} \begin{pmatrix} V_1^+ \\ V_2^+ \end{pmatrix} \tag{1.8}$$

Where S_{11}, and S_{22} are respectively the reflation parameters at port 1 and 2; S_{21}, and S_{12} are the transmission parameters from port 1 to port 2 and from port 2 to port 1 respectively. Then, any elements of the scattering parameters can be written as:

$$S_{ij} = \left. \frac{V_i^-}{V_j^+} \right|_{V_k^+ = 0; k \neq j} \tag{1.9}$$

1.6 GROUND PENETRATING RADAR

1.6.1 GPR principle

A GPR is a device equipped with a transmitting antenna and a receiving antenna aimed at detecting electromagnetic contrasts in the propagation medium. An EM wave is sent by the transmitting antenna, which propagates into the medium until it encounters a variation of its electromagnetic properties. When that happens, part of the wave is reflected back towards the surface (reflected wave), while the other part keeps propagating into the medium (transmitted wave). The reflected wave will be sensed by the receiving antenna and recorded by the GPR system in order to be processed for subsoil anomalies detection. Figure 1.5 summarizes the principle of GPRs and the wave propagation when applied in the area of landmine detection.

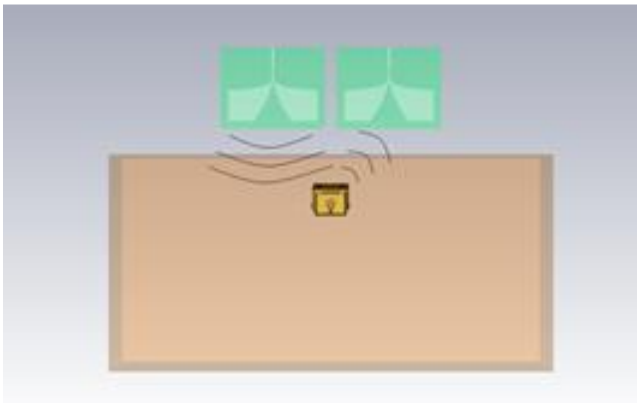

Figure 1.5 GPR system for landmine detection

The medium can have many effects on a GPR’s ability to detect an object inside it, and these effects are related to the medium’s electromagnetic properties [13]. The electromagnetic properties of a matter are mainly the permittivity, permeability, and conductivity which are related to the electric and magnetic field. Referring to Maxwell equations the electric field is affected directly by the relative permittivity and electrical conductivity of the material while the magnetic field is highly affected by the relative permeability of the medium of propagation [13]. Indeed, the relative permeability of the soil and non-magnetic dielectric materials that could be present in the soil is close to the air magnetic property and that is mean no reflections will occur in the EM wave due to the relative permeability homogeneity within these materials. Whereas a major reflection will happen during the propagation of the EM wave within the mediums due to the relative permittivity variation within the different dielectric materials. That explains why the electric field is the most dominant field in the GPR system [13].

It is known that the penetration depth of the EM wave in the soil decreases when the frequency increases, but the electrical conductivity plays an important role in growing the absorption rate for the propagated EM wave in the medium. Usually, the electrical conductivity increases in the soil due to the increase in its water content. For better detection efficiency, the designed GPR system should consider a trade-off between spatial resolution and depth penetration upon the target size and its location.

1.6.2 GPR system types

There are several types of GPR; the difference is the manner in which the data are acquired, either the time domain or the frequency domain. Impulse radar operates in the time domain while the continuous-wave (CW) radar operates in the frequency domain [14].

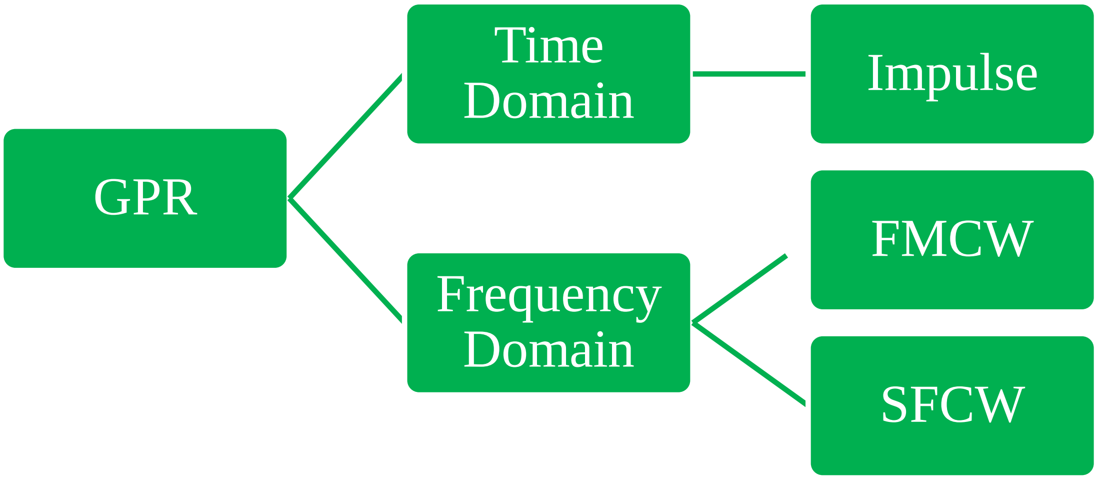

Figure 1.6 Common types of GPR

Impulse Radar:

Radars that acquire data in the time domain are generally known as an impulse. A time domain pulse is transmitted and the reflected energy is received as a function of time. The resulting waveform indicates the amplitude of energy scattered from subsurface objects versus time. Some advantages of impulse radar are the simplicity of generating an impulse waveform and low-cost parts. The disadvantages include undesirable ringing, inefficient use of transmit power (low duty cycle), and the resolution limited by pulse width. Other difficulties involve sampling of wideband signals with slow speed sequential digitizers [14].

Swept FMCW (Frequency-Modulated Continuous Wave) Radar:

Radars that acquire data in the frequency domain and transmit continuously (transmitter always on) are known as CW. If the carrier is frequency-modulated (FM), then it is referred to as FM-CW. The concept involves transmitting a frequency ‘‘sweep’’ over a fixed bandwidth, from a start frequency to a stop frequency. The reflected energy is received as a function of frequency and indicates the amplitude of energy scattered from subsurface objects. The sweep rate was inherently slow due to the nature of the test equipment and issues with data storage. The implementation of these prototype-swept FM-CW systems was limited by the state of technology at the time of development. Test equipment was used until lower-cost components such as frequency sources could be used (Oliver and Cuthbert, 1988), faster digital samplers were developed, and fast Fourier transforms (FFT) could be performed on digital signal-processing (DSP) boards or PCs [14].

SFMCW (Stepped Frequency-Modulated Continuous Wave) Radar:

A stepped-frequency radar is similar to a swept-frequency radar except that the transmitting frequency is stepped in linear increments over a fixed bandwidth, from a start frequency to a stop frequency. Several advantages of the stepped-frequency GPR are the controlled transmission frequencies, efficient use of power, and efficient sampling of wideband signals with low-speed ADCs. Disadvantages of stepped frequency include the complex electronics and the requirement of DSP, but it becomes practical with current technology. Also, time-varying gain cannot be applied to the return signal. A negative effect with the conversion from frequency to time is the introduction of sidelobes (from strong signals) that can mask out small signals from weak reflections. The advantages of swept-frequency over stepped are simpler design and lower cost for implementation. However, swept frequency may have a lower performance in some cases due to frequency ambiguities of the sweep, i.e., if the timing of the sample with the instantaneous frequency cannot be maintained throughout the entire sweep [14].

1.6.3 GPR data visualization

The GPR system can visualize the collected data in one, two, or three dimensions which are known as A, B, and C scans.

When the GPR placed above the soil and making a measurement at a single point the received signal can be plotted as voltage versus time as exhibited in Figure 1.7 and that what is called A-scan (one dimensional) visualization mode.

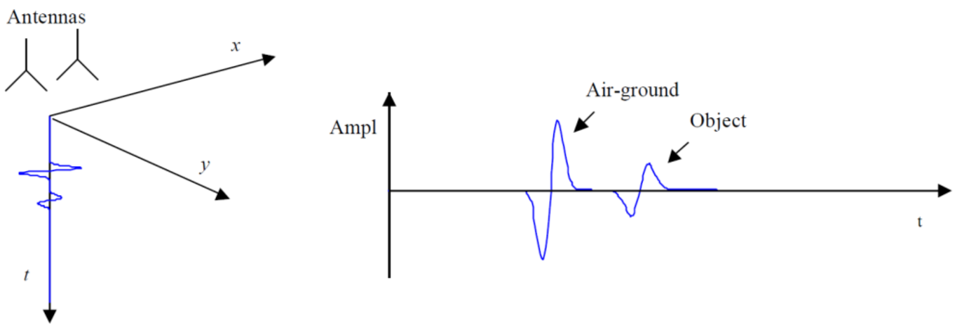

Figure 1.7 A-scan configuration and representation [15]

Moving the GPR along one horizontal direction and making A-scan measurement at multiple positions can form two dimensional data visualized in B-scan mode as displayed in Figure 1.8.

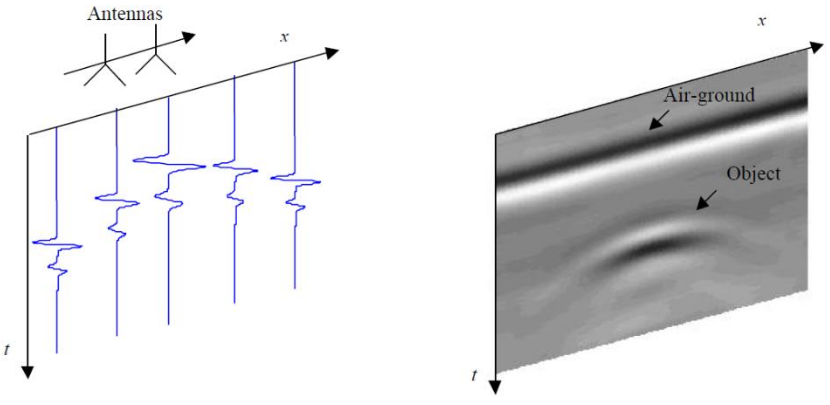

Figure 1.8 B-scan configuration and representation [15]

The three dimensional data can be formed by stacking multiple B-scan readings next to each other see Figure 1.9. In other words, the C-scan image can be formed by implementing a scanning scenario covering a rectangular area sliced into parallel lines and each line into several points.

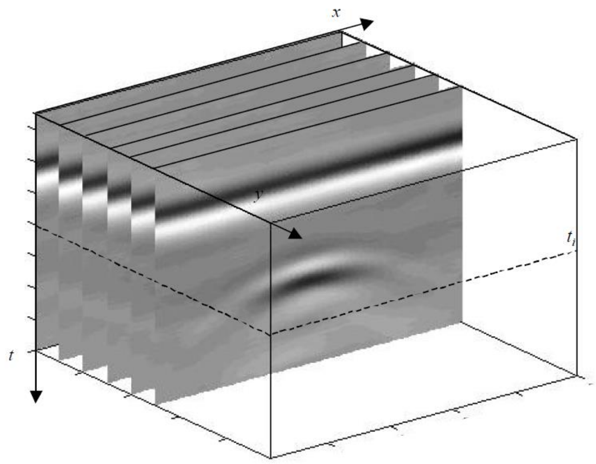

Figure 1.9 C-scan data visualization [15]

In the end, the target can be located from the noticed pic of the parabolic shape.

1.6.4 GPR applications

The wide applications and importance of ground penetrating radar (GPR) attract researchers and invite them to further develop this technology and work to enhance its efficiency and performance. In general, GPR is used for underground object detection and subsurface monitoring. GPR can be employed for different purposes in several fields of studies, for example, humanitarian demining [16][17], road pavement maintenance [18][19], snow depth estimation [20], water leakage detection [21] and other agriculture and archaeology applications [22] as shown in Table 1-2.

Table 1-2 Several applications of GPR in different areas

GPR applications	
Humanitarian Demining	Mines and Unexploded Bombs detection
Civil & Structural Engineering	Void Detection, Pavement Thickness, Reinforcing Bar Locating, Submarine Pipe and Cable Locating, Pipe Leak Detection (gas and water), Buried Pipe, and Cable Mapping
Geotechnical	Coal Mining, Hazardous Waste Mapping, Oil and Water Explorations, Geological Strata Profiling, and Ice Thickness Profiling
Transportation	Railroad Bed Profiling, Voids Under Pavement, and Runway Integrity Testing
Law Enforcement	Buried Body Detection, and Buried Weapons
Archaeology	Archaeological Prospecting: Cavity or Chamber Detection, and Treasure Prospecting

1.7 CONCLUSION

In this chapter, the humanitarian crisis resulting from the landmines contamination is pointed out. The state of the art for landmines detection methods is investigated. In addition, The basic electromagnetic theory behind the electromagnetic methods is introduced. The GPR concept and its use in the subsoil surface mapping are described also.

1.8 REFERENCES

[1] Landmine Monitor 2018 - 20th Annual Edition," 2018. [Online]. Available: http://the-monitor.org/media/2918780/Landmine-Monitor-2018_final.pdf.

[2] International Campaign to Ban Landmines." [Online]. Available: http://www.icbl.org/en-gb/home.aspx.

[3] Abujarad, Fawzy. "Ground penetrating radar signal processing for landmine detection." (2007).

[4] MacDonald, Jacqueline, J. R. Lockwood, John McFee, Thomas Altshuler, and Thomas Broach. Alternatives for landmine detection. No. RAND/MR-1608-OSTP. RAND CORP SANTA MONICA CA, 2003.

[5] Bhope, Pankaj C., and Anjali S. Bhalchandra. "Various Landmine Detection Techniques: A Review." *International Journal of Innovative Research in Science, Engineering and Technology* 4, no. 6 (2015).

[6] Cardona, Lorena, Jovani Jiménez, and Nelson Vanegas. "Landmine detection technologies to face the demining problem in Antioquia." Dyna 81, no. 183 (2014): 115-125.

[7] Kasban, H., O. Zahran, Sayed M. Elaraby, M. El-Kordy, and FE Abd El-Samie. "A comparative study of landmine detection techniques." *Sensing and Imaging: An International Journal* 11, no. 3 (2010): 89-112.

[8] "Difference Between Ionizing and Non-Ionizing Radiation." [Online]. Available: https://emfacademy.com/difference-ionizing-non-ionizing-radiation/.

[9] "The Electromagnetic Spectrum." [Online]. Available: http://www.ljcreate.com/posters/uk/electromagnetic-spectrum-poster.pdf.

[10] Pozar, David M. "Microwave engineering." *Wiley* (2012).

[11] "Introduction to s-parameters and ABCD Matrices Sub-module." [Online]. Available:http://www.waves.utoronto.ca/prof/svhum/ece422/labs/sdr/sparam.html.

[12] Druyts, P., Y. Yvinec, and M. Acheroy. "Relating soil properties to performance of metal detectors and ground penetrating radars." In *Using Robots in Hazardous Environments*, pp. 189-220. Woodhead Publishing, 2011.

[13] Jol, Harry M., ed. *Ground penetrating radar theory and applications*. elsevier, 2008.

[14] Daniels, Deborah J., David John Gunton and Howard F. Scott. “2 . Ground Penetrating Radar.” (2001).

[15] Sato, Motoyuki. "Principles of mine detection by ground-penetrating radar." *In Anti-personnel landmine detection for humanitarian demining*, pp. 19-26. Springer, London, 2009.

[16] Al Takach, Ali, Mohammed Al-Husseini, Ali El-Hajj, and Elias Nassar. "Linear to circular polarization transformation of vivaldi antennas and its use in GPR detection." *In IEEE Middle East Conference on Antennas and Propagation (MECAP)*, pp. 1-4., 2016.

[17] Guo, Chen, Li Zhao, Yan Chen, Wei Li, and Richard C. Liu. "Extraction of the pavement permittivity and thickness from measured ground-coupled GPR data using a ground-wave technique." *IEEE Geoscience and Remote Sensing Letters* 14, no. 3,pp. 399-403., 2017.

[18] Lalagüe, Anne. "Use of ground penetrating radar for transportation infrastructure maintenance." (2015).

[19] Liu, Hai, Kazunori Takahashi, and Motoyuki Sato. "Measurement of dielectric permittivity and thickness of snow and ice on a brackish lagoon using GPR." *IEEE journal of selected topics in applied earth observations and remote sensing* 7, no. 3, pp. 820-827, 2013.

[20] Hyun, Seung-Yeup, Yu-Sun Jo, Heon-Cheol Oh, and Se-Yun Kirn. "An experimental study on a ground-penetrating radar for detecting water-leaks in buried water transfer pipes." *In 6th International SYmposium on Antennas, Propagation and EM Theory, IEE Proceedings*, pp. 596-599, 2003.

[21] Pirri, M., P. Lombardo, and T. Bucciarelli. "Performance assessment of wide-band pulsed GPR for archaeological applications." *IEEE 2000 International Geoscience and Remote Sensing Symposium. Taking the Pulse of the Planet: The Role of Remote Sensing in Managing the Environment, Proceedings*, vol. 5, pp. 2385-2387, 2000.

[22] “Ground Penetrating Radars. Principles, Applications and Design Principle.” [Online]. Available: http://www.eltesta.com/Downloads/files/AN-1.pdf.

Chapter 2: Microwave Methods for Material Characterization

Contents

2.1 INTRODUCTION

The electromagnetic material characterization subject is a classical research topic in the electromagnetism area, this research matter derives its importance from the knowledge's need for material behavior when interacting in an electromagnetic wave. This interaction behavior can be represented by the permittivity ε and the permeability μ which are related to the electric and the magnetic fields respectively. The electromagnetic material characterization was and will remain the focus of attention for the researcher especially with the continued development of electronic technology and its expansion in different applications. The electromagnetic material properties are an essential factor in many traditional electronic applications (e.g., antennas, ground penetrating radar, circuit design and, etc.). Furthermore, innovative technologies can open new horizons in material characterization study. As an example of those technologies, the engineered material or what is called metamaterial that based on combining specific geometries of dielectrics and metals in a specific size to create unusual electromagnetic response at some frequencies of interest. Another technology example is the 3D-printing that becomes trending and frequently used in RF and microwave applications, it is of great value when traditional fabrication tools fail in terms of complexity and/or cost. This technology uses a specific material that has to be well-characterized in different conditions.

The electromagnetic characterization methods commonly fall into resonant and non-resonant methods. This chapter discusses the non-resonant microwave methods and techniques. The complete process including calibration and conversion methods are reported in detail in order to provide the upcoming researcher with the fundamental information needed for implementing their own conversion algorithm for different applications. Furthermore, simulation and measurement validation of the different material characterization methods have been presented in addition to the comparison study.

2.2 CHARACTERIZATION METHODS

We can divide material characterization methods into two main categories: resonant and non-resonant methods. The resonant method relies on the measurement of the resonant frequency and the quality factor while the non-resonant method relies on the transmission/reflection measurement of the electromagnetic wave [1]. The resonant method is applied by the resonator cavity with the greatest accuracy, but only at discrete frequencies. The non-resonant method is used by the transmission line with less accuracy, but it provides extraction over a wide bandwidth.

The method choice and its methodology depend on; the accuracy, the process, the sample insertion easiness, the kind of the test cell and, the bandwidth of interest.

In this study, our interest is the extraction of the intrinsic properties of different materials for GPR and demining application covering wide bandwidth. Due to that, the transmission/reflection method is selected.

2.2.1 Reflection method

In reflection methods, electromagnetic waves are propagated toward the MUT, and the properties of the MUT are obtained from the resulting reflection coefficient at a defined reference plane. Typically, one parameter is determined using the reflection method permittivity or permeability. The reflection method can be separated by tow reflection types: open circuit reflection and short circuit reflection.

The measurement fixture is usually made from a piece of transmission line which known as a measurement probe or sensor. The coaxial line is the most commonly used one as a test fixture among other types of transmission line for electromagnetic characterization measurement and that due to its advantage in the wide operational frequency bandwidth [1].

Open reflection method

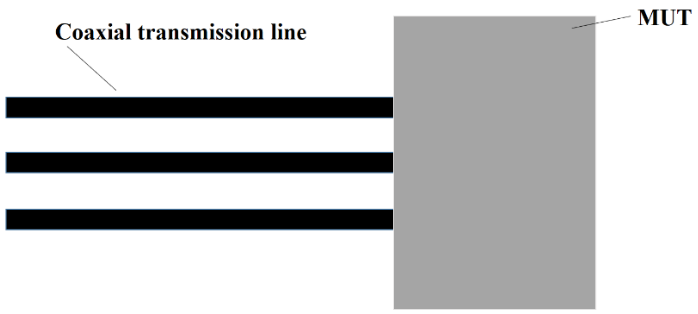

Figure 2.1 Open circuit reflection

The basic measurement configuration for the open reflection method is shown in Figure 2.1. The end of the coaxial probe is placed in direct contact with the MUT. When the propagated EM wave arrives at the MUT, a reflection occurs at the interface since each side has different impedance. The reflectivity at the interface is calculated from the impedances at both sides, and these impedances are related to the electromagnetic properties of the loaded material. Thus, the extraction of the electromagnetic properties of the MUT can be performed from the reflectivity.

This method has some assumptions: the first one is that the MUT is nonmagnetic material and the second one is that no reflection from the other side of the MUT sensed by the coaxial line. To achieve the second assumption, the thickness of the sample should be much larger than the diameter of the aperture of the open-ended coaxial line, and, meanwhile, the material should have enough loss [1].

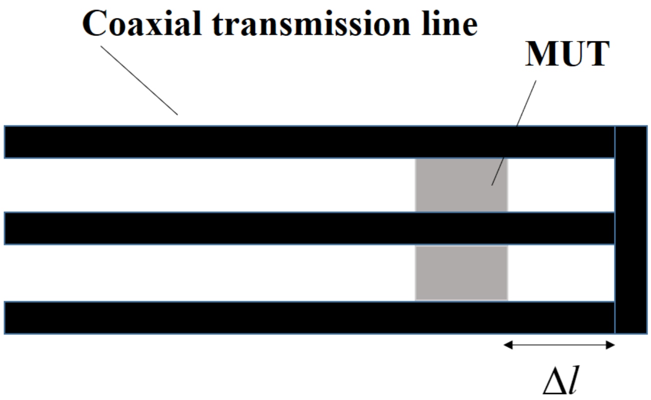

Figure 2.2 Short circuit reflection

Shorted reflection method

The general configuration of the short-circuit reflection method is exhibited in Figure 2.2. A piece of sample is fitted in a shorted circuit transmission line, the inserted sample is located at a distance $\Delta\ell$ from the short. In EM point of view, the short end area has a low electric field strength and high magnetic field strength, while the area located at $\lambda/4$ away from the short end has a high electric field strength and low magnetic field strength. So, the position of the MUT in the shorted transmission line depends on the parameter of interest. For computing the permeability the MUT should be placed near to the short end and, for computing the permittivity the MUT should be placed quarter wavelength away from the short end [1] [2].

2.2.2 Transmission/reflection method

The working principle for the transmission/reflection method has been systematically analyzed in literature [1][3]. In the transmission/reflection method, the MUT is placed in a transmission line to disrupt the structure field lines and measuring the material inherent properties using S-parameters. Once the transmission-line is defined, the use of the MUT in that fixture allows measuring the S-parameters along with those of the reference in utilizing the vector network analyzer (VNA).

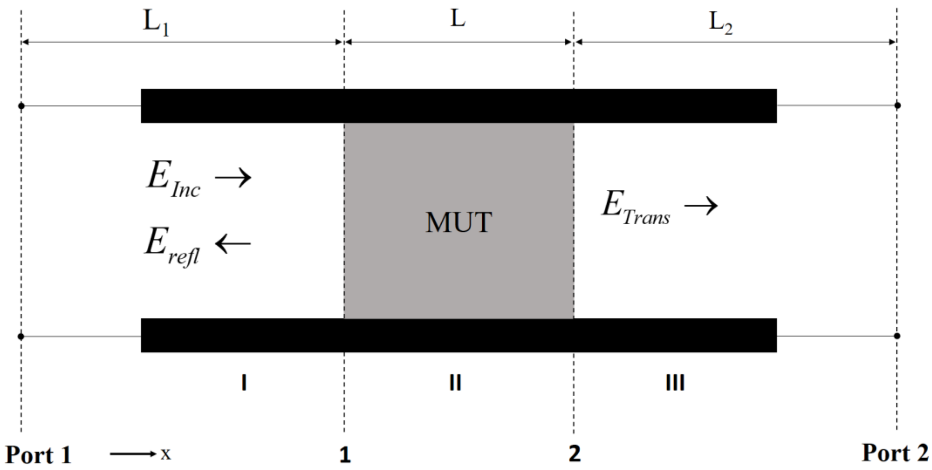

Figure 2.3 transmission and reflection EM wave from a MUT in transmission line

Figure 2.3 exhibits the general measurement configuration of two-port transmission line system. In this case, three sections are defined (I, II and, II) in order to analyze the electric field at the MUT interfaces. E_I, E_{II} and, E_{III} represent respectively the electric field at each zone.

$$E_I = e^{(-\gamma_0 x)} + C_1 e^{(\gamma_0 x)} \tag{2.1}$$

$$E_{II} = C_2 e^{(-\gamma x)} + C_3 e^{(\gamma x)} \tag{2.2}$$

$$E_{III} = C_4 e^{(-\gamma_0 x)} \tag{2.3}$$

With

$$\gamma = j\sqrt{\frac{\omega^2 \mu_r \varepsilon_r}{c^2} - \left(\frac{2\pi}{\lambda_c}\right)^2} \tag{2.4}$$

$$\gamma_0 = j\sqrt{\left(\frac{\omega}{c}\right)^2 - \left(\frac{2\pi}{\lambda_c}\right)^2} \tag{2.5}$$

where ω is the angular frequency, c is the speed of light in vacuum, γ_0 and γ are the propagation constants in the transmission lines filled with free space and the sample respectively. λ_c is the cutoff wavelength of the transmission line, and for a transmission line in TEM mode, for example, coaxial line, $\lambda_c = \infty$. The constants C_i (i = 1, 2, 3, 4) in Eqs. (2.1)-(2.3)can be determined from the boundary conditions on the electric field and the magnetic field. The boundary condition on the electric field is the continuity of the tangential component at the interfaces:

$$E_I \big|_{x=L_1} = E_{II} \big|_{x=L_1} \tag{2.6}$$

$$E_{II} \big|_{x=L_1+L} = E_{III} \big|_{x=L_1+L} \tag{2.7}$$

where L_1 and L_2 are the distances from the respective ports to the sample faces and L is the sample length. The total length of the transmission line is denoted as $L_{\text{total}} = L_1 + L_2 + L$. The boundary condition on the magnetic field requires the additional assumption that no surface currents are generated, so the tangent component of the magnetic field is continuous across the interface:

$$\frac{1}{\mu_0} \cdot \frac{\partial E_I}{\partial x}\bigg|_{x=L_1} = \frac{1}{\mu_0 \mu_r} \cdot \frac{\partial E_{II}}{\partial x}\bigg|_{x=L_1} \tag{2.8}$$

$$\frac{1}{\mu_0\mu_r}.\frac{\partial E_{II}}{\partial x}\bigg|_{x=(L_1+L)} = \frac{1}{\mu_0}.\frac{\partial E_{III}}{\partial x}\bigg|_{x=(L_1+L)} \tag{2.9}$$

The scattering parameters of the two-port network shown in Figure 2.3 can be obtained by solving Eqs. (2.1)-(2.3) subject to the boundary conditions (Eqs. (2.4)-(2.9)). As the scattering matrix is symmetric ($S_{12} = S_{21}$), we have [26][27]:

$$S_{11} = R_1^2.\frac{\Gamma\left(1-T^2\right)}{1-\Gamma^2T^2} \tag{2.10}$$

$$S_{22} = R_2^2.\frac{\Gamma\left(1-T^2\right)}{1-\Gamma^2T^2} \tag{2.11}$$

$$S_{21} = R_1R_2.\frac{T\left(1-\Gamma^2\right)}{1-\Gamma^2T^2} \tag{2.12}$$

where R_1 and R_2 are the reference plane transformations at two ports:

$$R_i = e^{-\gamma_0 L_i}, \left(i=1,2\right) \tag{2.13}$$

The transmission coefficient T is given by

$$T = e^{-\gamma L} \tag{2.14}$$

The reflection coefficient Γ is given by

$$\Gamma = \frac{\left(\frac{\gamma_0}{\mu_0}\right)-\left(\frac{\gamma}{\mu}\right)}{\left(\frac{\gamma_0}{\mu_0}\right)+\left(\frac{\gamma}{\mu}\right)} \tag{2.15}$$

For coaxial line, the cutoff wavelength is infinity, so Eq. (2.15) can be rewritten as

$$\boldsymbol{\Gamma} = \frac{\sqrt{\frac{\mu_r}{\varepsilon_r}}-1}{\sqrt{\frac{\mu_r}{\varepsilon_r}}+1} \tag{2.16}$$

Additionally, S_{21} for the empty sample holder is

$$S_{21}^{0} = R_1 R_2 e^{-\gamma_0 L} \quad (2.17)$$

For non-magnetic materials, Eqs. (2.10), (2.11), and (2.12), and contain $\varepsilon_r^{'}, \varepsilon_r^{"}$, L, and the reference plane transformations R_1 and R_2 as unknown quantities. We have four complex Eqs. (2.10), (2.11), (2.12), and (2.17), plus the equation for the length of the air line, so we have equivalently nine real equations for the five unknowns. In many applications, we know the sample length. For magnetic materials, we have seven unknowns. Thus, the system of equations is overdetermined and it is possible to solve the equations in various combinations. Therefore, the complex relative permittivity (ε_r) and complex relative permeability (μ_r) of the sample can be determined using different ways. In the following, we will discuss the conversion methods often used for the calculation of ε_r and μ_r.

2.3 MEASUREMENT CALIBRATION METHODS

The measurement calibration denotes the mathematical modeling of the systematic error that comes from the impedance mismatch, system frequency response and leakage signals in the test setup [5].. In another word, the calibration process aims to remove the unwanted parts from the measurements (e.g., cables or the transmission line adaptors). This step is important to move the reference plane of the measurement to the interface of the MUT. In the literature, different calibration methods are investigated [6]. The efficient calibration method used in RF and microwave measurement is the short, open, load and thru (SOLT) [7]. This calibration is popular in most commercial VNA, there is a specific calibration kit that can contain all these standard loads to end the cables with them.

Usually, there is no problem with the calibration of the coaxial cables that connected to the VNA. The critical problem starts when the error comes from the fixture itself, and then there is a need for a de-embedding method to remove this undesirable section (i.e.., the MUT is usually centrally placed, and the connector areas should be removed). The SOLT method is not applicable here because there is no load available with these areas over the whole bandwidth. In the following sections: the thru, reflect and line (TRL) and the short, open (SO) calibration methods are presented in detail, which can be used when the SOLT method is not possible to apply.

2.3.1 Thru, reflect and line (TRL) calibration

In this section, a detailed derivation (based on [8][9]) of the TRL calibration is presented in order to offer the readers the whole steps for implementing their own code. In this calibration method, four measurements are required: thru, reflect, line and line with MUT. The measurement configuration of the TRL calibration is shown in Figure 2.4. Where $\Delta\ell$ represents the length difference between the thru and line transmission line.

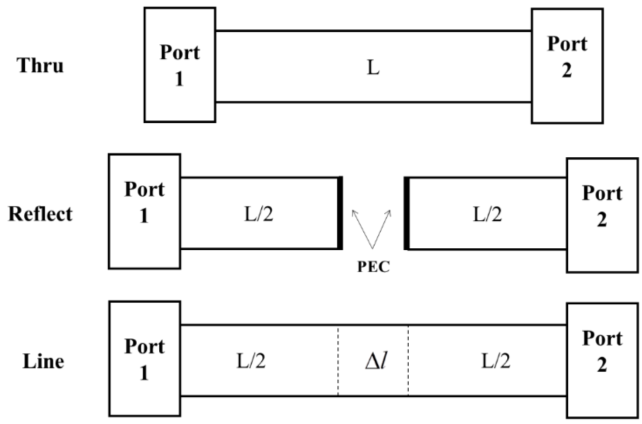

Figure 2.4 configuration of the TRL calibration measurement

For best accuracy, the optimal length of $\Delta\ell$ is the length which provides a quarter wavelength (90 degrees) of a phase difference between the thru and line at the center frequency [10].. From a mathematical point of view, it is more useful to analyze the system in a cascading form. The relation between Scattering parameters [S] matrix and wave cascading matrix (WCM) [T] is as follow [11]:

$$T = \begin{pmatrix} T_{11} & T_{12} \\ T_{21} & T_{22} \end{pmatrix} = \frac{1}{S_{21}} \begin{pmatrix} -\Delta & S_{11} \\ -S_{22} & 1 \end{pmatrix}, \qquad \Delta = S_{11}S_{22} - S_{12}S_{21} \tag{2.18}$$

$$S = \begin{pmatrix} S_{11} & S_{12} \\ S_{21} & S_{22} \end{pmatrix} = \begin{pmatrix} \dfrac{T_{12}}{T_{22}} & \dfrac{T_{11}T_{22} - T_{12}T_{21}}{T_{22}} \\ \dfrac{1}{T_{22}} & -\dfrac{T_{21}}{T_{22}} \end{pmatrix} \tag{2.19}$$

In the following, R denotes the WCM of the MUT which has $\Delta\ell$ as sample length, while R_M represents the WCM of the line with MUT. R_A and R_B are the WCM of the discontinuities including the ports at each side of the transmission line. The measurement matrix R_M is just the product of the matrices of the error boxes and the unknown MUT

$$R_M = R_A R R_B \quad \Longrightarrow \quad R = R_A^{-1} R_M R_B^{-1} \tag{2.20}$$

Let R_A be written as

$$R_A = \begin{pmatrix} r_{11} & r_{12} \\ r_{21} & r_{22} \end{pmatrix} = r_{22} \begin{pmatrix} a & b \\ c & 1 \end{pmatrix} \tag{2.21}$$

The inverse of R_A is

$$R_A^{-1} = \frac{1}{r_{22}} \frac{1}{a - bc} \begin{pmatrix} 1 & -b \\ -c & a \end{pmatrix} \tag{2.22}$$

R_B is similarly written as

$$R_B = \begin{pmatrix} \rho_{11} & \rho_{12} \\ \rho_{21} & \rho_{22} \end{pmatrix} = \rho_{22} \begin{pmatrix} \alpha & \beta \\ \gamma & 1 \end{pmatrix} \tag{2.23}$$

And the inverse of R_B is

$$R_B^{-1} = \frac{1}{\rho_{22}} \frac{1}{\alpha - \beta\gamma} \begin{pmatrix} 1 & -\beta \\ -\gamma & \alpha \end{pmatrix} \tag{2.24}$$

The matrix of the MUT is then found from

$$R = \frac{1}{r_{22}\rho_{22}} \frac{1}{a\alpha} \frac{1}{1 - b\dfrac{c}{a}} \frac{1}{1 - \gamma\dfrac{\beta}{\alpha}} \begin{pmatrix} 1 & -b \\ -c & a \end{pmatrix} R_M \begin{pmatrix} 1 & -\beta \\ -\gamma & \alpha \end{pmatrix} \tag{2.25}$$

Note that although there are eight terms in the error boxes, only seven quantities are needed to find R. They are *a, b, c, α, β, γ*, and r22ρ22. From the measurement of the through and of the line, seven quantities will be found. They are b, c/a, β/α, γ, $r_{22}\rho_{22}$, αa and $e^{2\gamma l}$. In addition to the seven quantities, if a were found, the solution would be complete. Let us first find the above seven quantities. The ideal through has an R matrix which is the 2x2 unit matrix. The measured R matrix with the through connected will be denoted by R_T and is given by

$$R_T = R_A R_B \tag{2.26}$$

With the line connected, the measured R matrix will be denoted by R_D and is equal to

$$R_D = R_A R_L R_B \tag{2.27}$$

Where R_L is the R matrix of the line, Now

$$R_B = R_A^{-1} R_T \tag{2.28}$$

So that

$$R_D = R_A R_L R_A^{-1} R_T \longrightarrow R_D R_T^{-1} R_A = R_A R_L \tag{2.29}$$

Define

$$T = R_D R_T^{-1} \tag{2.30}$$

Which when substituted into the above equations results in

$$T R_A = R_A R_L \tag{2.31}$$

The matrix T is known from measurements and will be written as

$$T = \begin{pmatrix} t_{11} & t_{12} \\ t_{21} & t_{22} \end{pmatrix} \tag{2.32}$$

Since the line is non-reflecting

$$R_L = \begin{pmatrix} e^{-\gamma l} & 0 \\ 0 & e^{-\gamma l} \end{pmatrix} \tag{2.33}$$

Recalling eq. (2.31) and writing the matrices results in

$$\begin{pmatrix} t_{11} & t_{12} \\ t_{21} & t_{22} \end{pmatrix} \begin{pmatrix} a & b \\ c & 1 \end{pmatrix} = \begin{pmatrix} a & b \\ c & 1 \end{pmatrix} \begin{pmatrix} e^{-\gamma l} & 0 \\ 0 & e^{-\gamma l} \end{pmatrix} \tag{2.34}$$

Next, writing out the four equations gives:

$$
\begin{aligned}
&t_{11}a + t_{12}c = ae^{-\gamma l} \\
&t_{21}a + t_{22}c = ce^{-\gamma l} \\
&t_{11}b + t_{12} = be^{+\gamma l} \\
&t_{21}b + t_{22} = e^{+\gamma l}
\end{aligned}
\tag{2.35}
$$

Dividing the first of the above equations by the second results in

$$
\frac{t_{11}a + t_{12}c}{t_{21}a + t_{22}c} = \frac{a}{c} = \frac{t_{11}\dfrac{a}{c} + t_{12}}{t_{21}\dfrac{a}{c} + t_{22}} \tag{2.36}
$$

Which gives a quadratic equation for *a/c*

$$
t_{21}\left(\frac{a}{c}\right)^2 + \left(t_{22} - t_{11}\right)\frac{a}{c} - t_{12} = 0 \tag{2.37}
$$

Dividing the third equation in the group by the fourth results in

$$
\frac{t_{11}b + t_{12}}{t_{21}b + t_{22}} = b \tag{2.38}
$$

Which gives the analogous quadratic equation for *b* as

$$
t_{21}b^2 + \left(t_{22} - t_{11}\right)b - t_{12} = 0 \tag{2.39}
$$

Dividing the fourth equation in the group by the second results in

$$
e^{2\gamma l} = c\,\frac{t_{21}b + t_{22}}{t_{21}a + t_{22}c} = \frac{t_{21}b + t_{22}}{t_{21}\dfrac{a}{c} + t_{22}} \tag{2.40}
$$

Since $e^{2\gamma l}$ is not equal to 1, *b* and *a/c* are distinct roots of the quadratic equation. The following discussion will enable the choice of the root.

Now

$$
b = \frac{r_{12}}{r_{22}} = S_{11} \tag{2.41}
$$

And

$$\frac{a}{c} = \frac{r_{11}}{r_{21}} = S_{11} - \frac{S_{12}S_{21}}{S_{22}} \tag{2.42}$$

For a well designed transition between coax and the non-coax $|S_{22}|$, $|S_{11}|$ <<1 which yields $|b|$<< 1 and $|a/c|$>>1. Therefore, $|b| \ll \left|\frac{a}{c}\right|$ which determines the choice of the root. Recalling eq. (2.31)

$$\det(T)\det(R_A) = \det(R_A)\det(R_L) \tag{2.43}$$

Or

$$\det(T) = \det(R_L) = 1 \tag{2.44}$$

So that

$$t_{11}t_{22} - t_{12}t_{21} = 1 \tag{2.45}$$

Which implies that there are only three independent T_{ij}. Then there are only three independent results, *e.g.* b, a/c, and $e^{2\gamma L}$. Now let us find four more quantities

$$r_{22}\rho_{22}\begin{pmatrix} a & b \\ c & 1 \end{pmatrix}\begin{pmatrix} \alpha & \beta \\ \gamma & 1 \end{pmatrix} = R_A R_B = R_T = g\begin{pmatrix} d & e \\ f & 1 \end{pmatrix} \tag{2.46}$$

Now

$$\begin{pmatrix} a & b \\ c & 1 \end{pmatrix}^{-1} = \frac{1}{a-bc}\begin{pmatrix} 1 & -b \\ -c & a \end{pmatrix} \tag{2.47}$$

So that

$$r_{22}\rho_{22}\begin{pmatrix} \alpha & \beta \\ \gamma & 1 \end{pmatrix} = \frac{g}{a-bc}\begin{pmatrix} 1 & -b \\ -c & a \end{pmatrix}\begin{pmatrix} d & e \\ f & 1 \end{pmatrix} \tag{2.48}$$

Or

$$r_{22}\rho_{22}\begin{pmatrix} \alpha & \beta \\ \gamma & 1 \end{pmatrix} = \frac{g}{a-bc}\begin{pmatrix} d-bf & e-b \\ af-cd & a-ce \end{pmatrix} \tag{2.49}$$

From which we can extract

$$r_{22}\rho_{22} = g\frac{a-ce}{a-bc} = g\frac{1-e\frac{c}{a}}{1-b\frac{c}{a}} \tag{2.50}$$

We also have

$$\begin{pmatrix} \alpha & \beta \\ \gamma & 1 \end{pmatrix} = \frac{1}{a-ce}\begin{pmatrix} d-bf & e-b \\ af-cd & a-ce \end{pmatrix} \tag{2.51}$$

From which we obtain

$$\gamma = \frac{f-\frac{c}{a}d}{1-\frac{c}{a}e} \tag{2.52}$$

And

$$\frac{\beta}{\alpha} = \frac{e-b}{d-bf} \tag{2.53}$$

And

$$\alpha a = \frac{d-bf}{1-\frac{c}{a}e} \tag{2.54}$$

The additional four quantities found are β/α, γ, $r_{22}\rho_{22}$ and αa. To complete the solution, one needs to find a. Let the reflection measurement through error box A be w_1. Then

$$w_1 = \frac{a\Gamma_R + b}{c\Gamma_R + 1} \tag{2.55}$$

Which may be solved for a in terms of the known b and a/c as

$$a = \frac{w_1 - b}{\Gamma_R\left(1 - w_1\frac{c}{a}\right)} \tag{2.56}$$

We need a method to determine a. Use the measurement for the reflect from through the error box B. Let w_2 denotes the measurement

$$w_2 = S_{22} + \frac{S_{12}S_{21}\Gamma_R}{1 - S_{11}\Gamma_R} = \frac{S_{22} - \Delta\Gamma_R}{1 - S_{11}\Gamma_R} \tag{2.57}$$

$$w_2 = \frac{-\frac{\rho_{21}}{\rho_{22}} + \frac{\rho_{11}}{\rho_{22}}\Gamma_R}{1 - \frac{\rho_{12}}{\rho_{22}}\Gamma_R} \tag{2.58}$$

Or

$$w_2 = -\frac{\alpha\Gamma_R - \gamma}{\beta\Gamma_R - 1} \tag{2.59}$$

α may be found in terms of γ and β/α as

$$\alpha = \frac{w_2 + \gamma}{\Gamma_R\left(1 + w_2\frac{\beta}{\alpha}\right)} \tag{2.60}$$

Recall eq. (2.56) so that

$$\frac{a}{\alpha} = \frac{w_1 - b}{w_2 + \gamma}\,\frac{1 + w_2\frac{\beta}{\alpha}}{1 - w_1\frac{c}{a}} \tag{2.61}$$

From earlier eq. (2.54) so that

$$a^2 = \frac{w_1 - b}{w_2 + \gamma}\,\frac{1 + w_2\frac{\beta}{\alpha}}{1 - w_1\frac{c}{a}}\,\frac{d - bf}{1 - \frac{c}{a}e} \tag{2.62}$$

Or

$$a = \pm\left(\frac{w_1 - b}{w_2 + \gamma}\,\frac{1 + w_2\frac{\beta}{\alpha}}{1 - w_1\frac{c}{a}}\,\frac{d - bf}{1 - \frac{c}{a}e}\right)^{\frac{1}{2}} \tag{2.63}$$

Which determines *a* to within *a* ± sign.

$$\Gamma_R = \frac{w_1 - b}{a\left(1 - w_1 \dfrac{c}{a}\right)} \tag{2.64}$$

So if Γ_R is known to within ± then a may be determined as well. Calibration is complete and we can now proceed to the measurement of the MUT. From earlier, the matrix of the MUT is found from Eq. (2.25). In which all the terms have now been determined.

2.3.2 TRL simulation validation

Relying on the previous theoretical description of the TRL calibration, a *Matlab* code was implemented for calibration use with the measured data. In this section, the validation of the TRL calibration technique is investigated using data exported from computer simulation technology (CST) which is an EM simulation software. Due to its electromagnetic properties advantage, the coaxial transmission line is selected as a fixture test. The coaxial transmission line allows the propagation of the TEM mode and the cut-off frequencies of the higher-order modes are very high and out of our interest frequency range. The numerical validation is performed by comparing the S parameters of an ideal two-port network with the calibrated S parameters of a two-port network which has discontinuities.

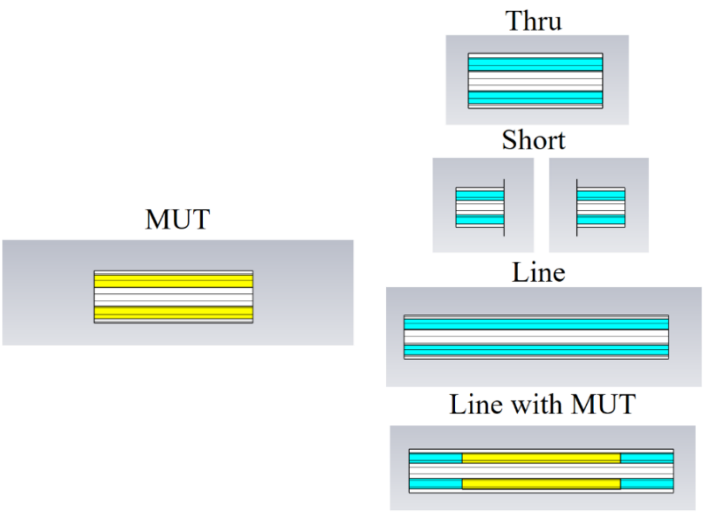

Figure 2.5 Cross-section view of the coaxial line fixtures employed for TRL calibration

Figure 2.5 shows the cross-section view of the different fixtures cases which are required for obtaining the sufficient S parameters results for the comparison. In

Figure 2.6, we can see real and imaginary parts comparison of the simulated and the calibrated S parameters of the MUT which has 1.5 cm as length. The presented results show a good similarity between the two cases and this proves the validity of the TRL calibration techniques over all the bandwidth from DC till 8 GHz.

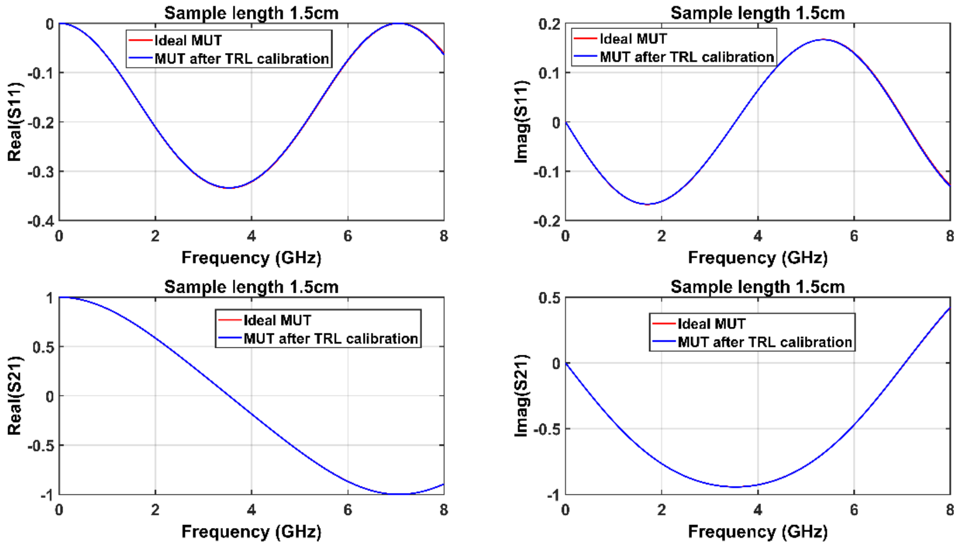

Figure 2.6 real and imaginary parts comparison of the S parameters for the ideal and the calibrated sample

Now, we are trying to make the problem more difficult and more practical by using unmatched coaxial transmission line fixture. The characteristic impedance of the transmission line is 75 ohms cascaded with connectors or transition section have 50 ohms as characteristic impedance. Like the previous validation procedure, we will simulate the MUT in two scenarios: first, inserted in an ideal transmission line and second, inserted in the proposed fixtures as shown in Figure 2.6.

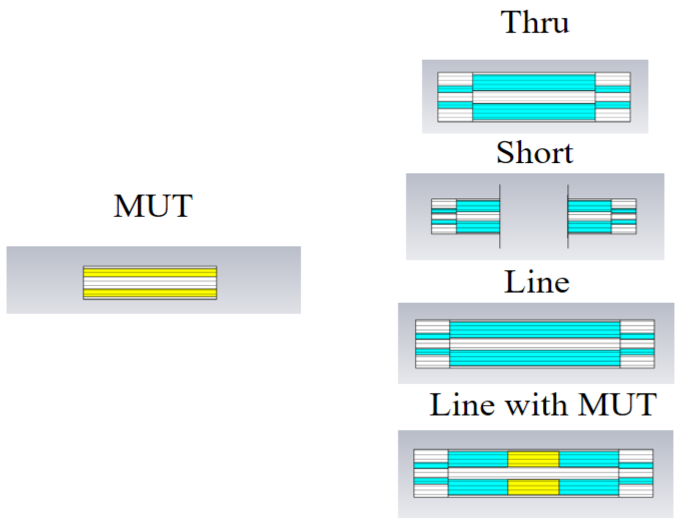

Figure 2.7 Cross-section view of the coaxial line fixtures with connectors employed for TRL calibration

The comparison of the S parameters responses for the calibrated and the ideal simulated cases are shown in Figure 2.8. Also, good convenience between the two results is noted in the whole bandwidth and this demonstrates the efficiency of the TRL calibration technique.

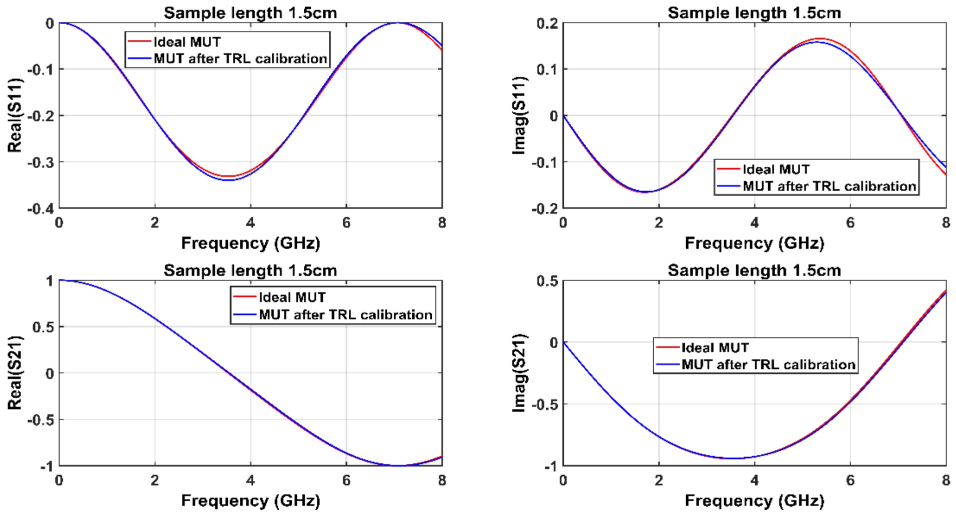

Figure 2.8 real and imaginary parts comparison of the S parameters for the ideal and the calibrated sample

2.3.3 Short and open (SO) calibration

The presented SO calibration technique is employed for taking off the responses of the test fixture’s discontinuities shown in Figure 2.9. The detailed steps of the SO calibration technique are reported in this section. This calibration is more simple than the TRL calibration. In addition, three measurements are needed to implement the calibration process. The required measurements are short, open loaded and total line with MUT.

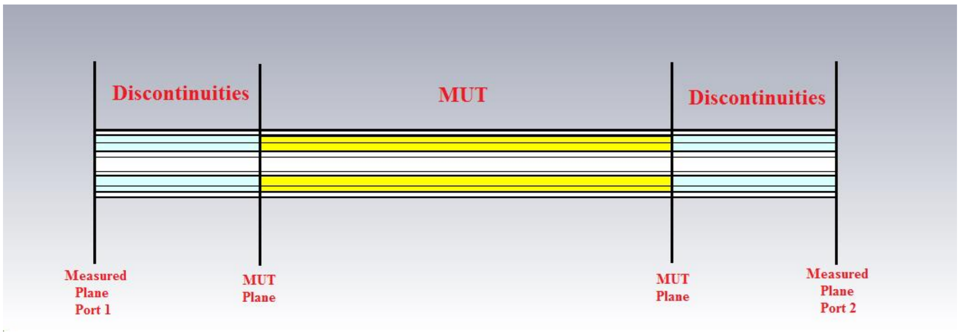

Figure 2.9 typical measurement plane configuration of two ports device

The total line with MUT measurement is the configuration presented in Figure 2.9. While the short and open measurements are the measurement of the discontinuities sections ending with the short or open circuit as exhibited in Figure 2.10.

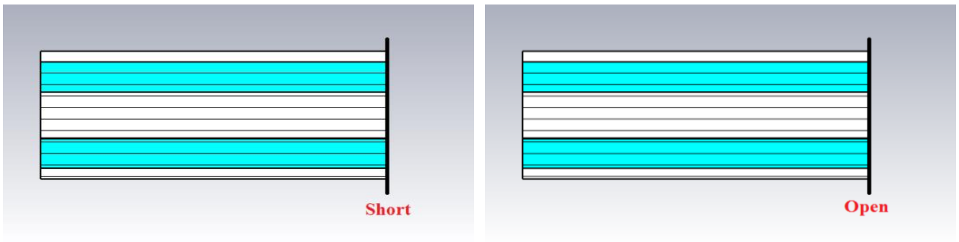

Figure 2.10 short and open measurements needed for de-embedding the discontinuities part

This calibration technique uses the ABCD matrix for representing the different sections. So with the ABCD matrix, we can analyze the system in cascading form by multiplying the different ABCD matrices as expressed in Eq. (2.66).

$$\begin{pmatrix} A & B \\ C & D \end{pmatrix}_{Total} = \begin{pmatrix} A & B \\ C & D \end{pmatrix}_{disc} \times \begin{pmatrix} A & B \\ C & D \end{pmatrix}_{MUT} \times \begin{pmatrix} A & B \\ C & D \end{pmatrix}_{disc} \qquad (2.65)$$

By multiplying the total $ABCD_{Total}$ matrix by the inverse of the $ABCD_{disc}$ at both sides, we can then obtain the $ABCD_{MUT}$ as follow:

$$\begin{pmatrix} A & B \\ C & D \end{pmatrix}_{MUT} = \begin{pmatrix} A & B \\ C & D \end{pmatrix}_{disc}^{-1} \times \begin{pmatrix} A & B \\ C & D \end{pmatrix}_{Total} \times \begin{pmatrix} A & B \\ C & D \end{pmatrix}_{disc}^{-1} \qquad (2.66)$$

Where,

$$\begin{pmatrix} S_{11} & S_{12} \\ S_{21} & S_{22} \end{pmatrix}_{Total} \rightarrow \begin{pmatrix} A & B \\ C & D \end{pmatrix}_{Total} \qquad (2.67)$$

Using the relation between the S matrix parameters and the *ABCD* matrix parameters [12] we can found the $ABCD_{Total}$ from the measured S_{Total}.

$$\begin{pmatrix} A & B \\ C & D \end{pmatrix} = \begin{pmatrix} \dfrac{(1+S_{11})(1-S_{22})+S_{12}S_{21}}{2S_{21}} & Z_0\dfrac{(1+S_{11})(1+S_{22})-S_{12}S_{21}}{2S_{21}} \\ \dfrac{1}{Z_0}\dfrac{(1-S_{11})(1-S_{22})-S_{12}S_{21}}{2S_{21}} & \dfrac{(1-S_{11})(1+S_{22})+S_{12}S_{21}}{2S_{21}} \end{pmatrix} \qquad (2.68)$$

We still have to find the $ABCD_{disc}$.

Writing the equation of reflection coefficient in one port network system in term of impedance for the two cases short and open:

$$S_{11short} = \frac{Z_{sc} - Z_0}{Z_{sc} + Z_0} \text{ and, } S_{11open} = \frac{Z_{oc} - Z_0}{Z_{oc} + Z_0} \qquad (2.69)$$

Where, Z_0, Z_{sc} and, Z_{oc} are respectively the characteristic impedance of the measuring device, the input impedance of the discontinuity section ended with short circuit and, the input impedance of the discontinuity section ended with an open circuit. Then Eq. (2.69) can be rewritten:

$$Z_{sc} = Z_0\frac{(1+S_{11short})}{(1-S_{11short})} \text{ and, } Z_{oc} = Z_0\frac{(1+S_{11open})}{(1-S_{11open})} \qquad (2.70)$$

After the determination of the impedances of short and open cases the characteristic impedance of the discontinuity part can be expressed as follow:

$$Z_c = \sqrt{Z_{sc} \times Z_{oc}} \tag{2.71}$$

Also, the propagation constant of the discontinuity section can be computed from the predetermined impedances:

$$\tan h(\gamma L) = \sqrt{\frac{Z_{sc}}{Z_{oc}}} \Rightarrow \gamma L = \operatorname{arctanh}\left(\sqrt{\frac{Z_{sc}}{Z_{oc}}}\right) \tag{2.72}$$

Since there is a relation between the *ABCD* matrix and the transmission line properties (the propagation constant and the characteristic impedance), the $ABCD_{disc}$ matrix is simply deduced.

$$\begin{pmatrix} A & B \\ C & D \end{pmatrix}_{disc} = \begin{pmatrix} \cosh(\gamma L) & Z_c \sinh(\gamma L) \\ \dfrac{\sinh(\gamma L)}{Z_c} & \cosh(\gamma L) \end{pmatrix} \tag{2.73}$$

Finally by substituting $ABCD_{Total}$ and $ABCD_{disc}$ matrices in Eq. (2.66)we can obtain the $ABCD_{MUT}$ matrix. Relying on the relation between the *ABCD* matrix and the S parameters matrix we can convert back the *ABCD* matrix to S matrix. Thus the calibrated S parameters of the MUT is calculated using (2.74) [12].

$$\begin{pmatrix} S_{11} & S_{12} \\ S_{21} & S_{22} \end{pmatrix} = \begin{pmatrix} \dfrac{A + \frac{B}{Z_0} - CZ_0 - D}{A + \frac{B}{Z_0} + CZ_0 + D} & \dfrac{2(AD - BC)}{A + \frac{B}{Z_0} + CZ_0 + D} \\ \dfrac{2}{A + \frac{B}{Z_0} + CZ_0 + D} & \dfrac{-A + \frac{B}{Z_0} - CZ_0 + D}{A + \frac{B}{Z_0} + CZ_0 + D} \end{pmatrix} \tag{2.74}$$

2.3.4 SO Simulation validation

The same procedure is followed here to validate numerically the SO calibration technique. The implemented *Matlab* code for the SO calibration requires three measurement cases as described in the theoretical section. The cross-section view of the coaxial line fixtures employed for simulates the ideal MUT and the MUT with discontinuities are shown in (2.11). The short-circuit load can be made by making a

PEC sheet at the end of the transmission line. The open-circuit load can be modeled by creating a PMC boundary condition at the end of the coaxial line which means that the magnetic field is zero there.

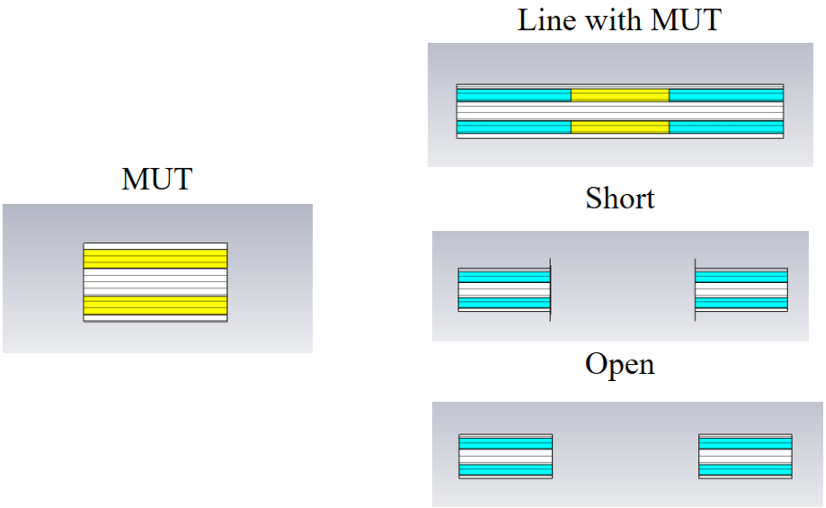

Figure 2.11 Cross-section view of the coaxial line fixtures employed for SO calibration

The simulated MUT has 1.5 cm as length. The real and imaginary parts of the S parameters for the ideal and calibrated MUT are compared in Figure 2.12. A good similarity is noted in the results for the two scenarios. Except for a pic, the response appeared at around 4.3 GHz, and this is due to numerical computation divergence that exist in Eq. (2.70) expression when we have zero in the denominator. This behavior could be solved easily by a smoothing filter for the resulted curves.

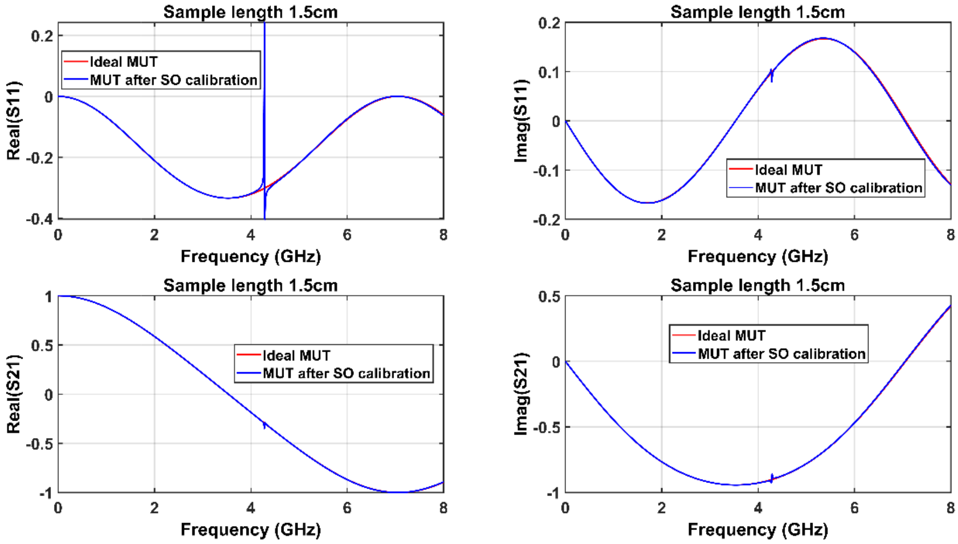

Figure 2.12 real and imaginary parts comparison of the S parameters for the ideal and the calibrated sample

2.4 CONVERSION METHODS

Following the material characterization steps, and after the sample preparation as well as measurement calibration, it is time now to find the relationship between the measured S parameters and the inherent material properties. Based on this relationship a conversion algorithm should be implemented in order to extract the electrical properties of the MUT. In the fact that there is no perfect conversion method for all MUT conditions and each technique has its advantages and limitations, the selection of the appropriate technique depending on the application and the MUT. There are several conversion techniques established in the literature, most of them based on the Nicolson-Ross-Weir (NRW). In this section, four conversion methods have been presented in details namely, NRW, Retrieval method, ABCD matrix method, and T matrix method. In addition, two other conversion techniques that work with uncalibrated S parameters (self-calibration included) are reported (i.e., SO characterization technique, and Two-transmission-line technique).

2.4.1 NRW method

The NRW method is first introduced by Nicolson, Ross, and Weir [4] [13]. In the following, a precise description of the conversion technique is exhibited relying on [14][15]. In our implementation, we suppose that the two-port network is symmetrical and reciprocal. Thus, $S_{11}=S_{22}$, and $S_{12}=S_{21}$. Furthermore, when the reference plane measurement is at the interface of the MUT Eqs. (2.10), (2.11), and (2.12) can be rewritten as:

$$S_{11} = \frac{\left(1-T^2\right)\Gamma}{1-T^2\Gamma^2},\ S_{21} = \frac{\left(1-\Gamma^2\right)T}{1-T^2\Gamma^2} \tag{2.75}$$

Here, T is the propagation factor expressed as:

$$T = e^{-jk_z d} \tag{2.76}$$

Where, k_z is the z-component of the propagation vector given by:

$$k_z^2 = k^2 - \kappa^2 \tag{2.77}$$

While, $k = \omega\sqrt{\mu\varepsilon}$ is the wavenumber in the material, and κ = 0 for TEM transmission line system. Moreover, Γ is the interfacial reflection coefficient then it is written in term of impedances:

$$\Gamma = \frac{Z - Z_0}{Z + Z_0} \tag{2.78}$$

For TEM transmission line systems, $Z = \eta$ and $Z_0 = \eta_0$, where $\eta = \sqrt{\frac{\mu}{\varepsilon}}$ and $\eta_0 = \sqrt{\frac{\mu_0}{\varepsilon_0}}$

Defining the intermediate quantities:

$$V_1 = S_{21} + S_{11} = \frac{T+\Gamma}{1+\Gamma T},\ V_2 = S_{21} - S_{11} = \frac{T-\Gamma}{1-\Gamma T} \tag{2.79}$$

Hence, we can rearrange the expressions to get into second-order polynomial equations.

$$\Gamma^2 - 2\Gamma X + 1 = 0 \tag{2.80}$$

Where

$$X = \frac{1-V_1V_2}{V_1 - V_2} = \frac{1-S_{21}^2 + S_{11}^2}{2S_{11}} \tag{2.81}$$

The solution of Eq. (2.80) is:

$$\Gamma = X + s_1\sqrt{X^2 - 1} \qquad (2.82)$$

Where, $s_1 = \pm 1$. In order to solve the sign ambiguity, an assumption should be made that the MUT is passive. Thus, one sign option satisfies the inequality $|\Gamma| \leq 1$. Then Γ is found, and T is simply determined as:

$$T = \frac{V_1 - \Gamma}{1 - V_1\Gamma} = |T|e^{j\phi} \qquad (2.83)$$

Where $-\pi < \phi \leq \pi$. Equating Eq. (2.83) to Eq. (2.76) and defining the dimensionless quantity $\overline{k_z} = \frac{k_z}{k_0}$, k_z is found by taking the natural logarithm:

$$\overline{k_z} = \frac{n - \frac{\phi}{2\pi}}{\frac{d}{\lambda_0}} + j\frac{\frac{\ln|T|}{2\pi}}{\frac{d}{\lambda_0}} \qquad (2.84)$$

Here $\lambda_0 = f/c$ is the free-space wavelength. This equation reveals one of the known difficulties with the NRW method. The integer n defines the branch of the log function. Its value is not known a priori but is related to the electrical thickness of the sample. With $\overline{k_z}$ known, μ and ε are determined as follows. First, define

$$F = \frac{1 - \Gamma}{1 + \Gamma} \qquad (2.85)$$

Then, for TEM waveguiding systems,

$$\varepsilon_r = \overline{k_z}F \qquad (2.86)$$

$$\mu_r = \frac{\overline{k_z}}{F} \qquad (2.87)$$

The main limitation of the NRW technique is the sharp drops responses appeared in the extracted ε and μ results. These drops occur at specific frequencies that have integers multiple of half guided wavelengths of the sample length. In a deep analysis, when the sample thickness is closer to $\lambda_g/2$ the value of S_{11} is closer to zero which will lead to inconsistency in Eq.(2.81), as well as peaks in the results. The easiest way to avoid this problem is to use a sample length smaller than $\lambda_g/2$ (n=0) at the lower frequency of interest. Several ways to overcome this branch's ambiguity are discussed in [16]

2.4.2 Retrieval method

This method is first introduced in [17] and [18] for metamaterial characterization purpose. Indeed, the retrieval method starts from the same equations of the NRW method but taking later different assumptions and analytical analysis to solve the problem. Here, the precise steps [19] are interpreted in order to link the S parameters to the electrical properties which will be found in terms of impedance and refractive index. Referring to the known relationship between the wavenumber and the refractive index ($k = k_0 n$ in case of the TEM wave-guiding system), in addition to Eqs. (2.75), (2.76), and (2.78) we can express the following:

$$S_{11} = \frac{\left(1-T^2\right)\Gamma}{1-T^2\Gamma^2}, S_{21} = \frac{\left(1-\Gamma^2\right)T}{1-T^2\Gamma^2}, \Gamma = \frac{Z-Z_0}{Z+Z_0}, \text{ and } T = e^{jk_0nd} \tag{2.88}$$

By rearranging Eq. (2.88) we can now calculate the impedance from the S parameters.

$$Z = \pm\sqrt{\frac{\left(1+S_{11}\right)^2 - S_{21}^2}{\left(1-S_{11}\right)^2 - S_{21}^2}} \tag{2.89}$$

Under the assumption that we are dealing with a passive material, we can consider that the MUT has no gain. This indicates that: $\mathrm{Re}[Z] \geq 0$; $\mathrm{Im}[n] \geq 0$; $\mathrm{Im}[\mu_r] \geq 0$; $\mathrm{Im}[\varepsilon_r] \geq 0$. Making use of the inequality ($\mathrm{Re}[Z] \geq 0$) we can solve the sign ambiguity in Eq. (2.89). Then, When Z obtained the transmission coefficient T is consequently obtained using the below equation:

$$T = \frac{S_{21}}{1 - S_{11}\Gamma} \tag{2.90}$$

Calling T from Eq. (2.88) and retrieving the refractive index by inverting the exponential in two steps. First, we have to write the refractive index in complex form.

$$T = e^{jk_0(n^{'} + jn^{''})d} = e^{jk_0 n^{'} d} e^{-k_0 n^{''} d} \tag{2.91}$$

Second, we compute the natural log of this equation.

$$\begin{aligned}
\ln T &= \ln\left(e^{jk_0 n^{'} d} e^{-k_0 n^{''} d}\right) \\
\ln T &= \ln\left(e^{jk_0 n^{'} d}\right) + \ln\left(e^{-k_0 n^{''} d}\right) \\
\ln T &= j\left(k_0 n^{'} d - 2\pi m\right) - k_0 n^{''} d
\end{aligned} \tag{2.92}$$

Since m is any integer, we can select the appropriate sign. From Eq. (2.92) we have:

$$\begin{aligned}
\operatorname{Re}\left[\ln T\right] &= -k_0 n^{''} d \\
\operatorname{Im}\left[\ln T\right] &= k_0 n^{'} d - 2\pi m
\end{aligned}
\quad \Longrightarrow \quad
\begin{aligned}
n^{'} &= \frac{1}{k_0 d}\left(Im\left[\ln T\right] + 2\pi m\right) \\
n^{''} &= -\frac{1}{k_0 d}\operatorname{Re}\left[\ln T\right]
\end{aligned} \tag{2.93}$$

Now, *n''* is known, but *n'* will be obtained after resolve the branching problem.

The branching problem can be solved by following the next analytical procedure: First, computes *m* at the first frequency point:

Since the material is passive, the $\operatorname{Im}\left[\mu_r\right] \geq 0$, $\operatorname{Im}\left[\varepsilon_r\right] \geq 0$ which gives:

$$\left|n^{'} Z^{''}\right| \leq n^{''} Z^{'} \tag{2.94}$$

We choose the branch index *m* that satisfies Eq. (2.94). Then, two scenarios can happen:

1. Only one solution for *m* exists. That is the correct answer.
2. Multiple solutions exist. For each branch *m*, we calculate the refractive index for all other frequencies. The correct choice for the initial branch *m* will produce a refractive index function that satisfies the above relation for all frequencies.

Second, the correct value of *m and n* are known at first frequency now. So, taking the advantage of a Taylor series we can compute the refractive index for the next frequency. Let's define $n(f_0)$, and $n(f_1)$ as the refractive indexes at the first and the second frequency respectively.

$$e^{jk_0(f_1)n(f_1)d}=e^{jk_0(f_0)n(f_0)d}\left[1+\Delta+\frac{\Delta^2}{2}+\ldots\right],$$
$$\Delta=jk_0\left(f_1\right)n\left(f_1\right)d-jk_0\left(f_0\right)n\left(f_0\right)d \tag{2.95}$$

The only unknown in this equation is the branch index *m* that occurs in the real part of $n(f_1)$ on the left-hand side. The equation is a binomial function of the unknown $n(f_1)$ and has two possible solutions.

$$n\left(f_1\right)\big|_{Root\#1} \text{ or } n\left(f_1\right)\big|_{Root\#2} \tag{2.96}$$

The imaginary part of $n(f_1)$ is obtainable without ambiguity. We then choose the root that has an imaginary part closer to the previous n'' computed using Eq. (2.93). Hence, from the real part of the selected root, we can extract *m* which will use to find the exact refractive index.

Finally, the complex permittivity and permeability can be deduced as follow:

$$\mu_r=nZ \tag{2.97}$$

$$\varepsilon_r=\frac{n}{Z} \tag{2.98}$$

As we mentioned before this method is investigated for metamaterial characterization application and its use in homogenous material characterization is still efficient, but there is a limitation in the sample length which should be less than $\lambda_g/2$ for the lowest frequency of interest to avoid divergence response.

2.5 CONVERSION METHOD BASED ON THE PROPAGATION CONSTANT

Figure 2.13 Ideal two-port network system configuration

The analytical way of complex permittivity extraction from the propagation constant is presented here. Relying on the derivation of Maxwell's equations we can write the propagation constant γ for any medium as follow:

$$\gamma = j\omega\sqrt{\mu\varepsilon} = j\omega\sqrt{\mu\left(\varepsilon^{'} - j\varepsilon^{"}\right)} \equiv \alpha + j\beta \tag{2.99}$$

Then, if we take the propagation constant to the power 2 we get:

$$\gamma^2 = -\omega^2\mu\left(\varepsilon^{'} - j\varepsilon^{"}\right) = \alpha^2 - \beta^2 + 2j\alpha\beta \tag{2.100}$$

By taking the equivalence of the real and imaginary part at each side of the previous equation, then the complex permittivity quantity is calculated using the below relations

$$\varepsilon_r^{'} = -\frac{Real\left(\gamma^2\right)}{\omega^2\mu_0\mu_r\varepsilon_0} = -\frac{c^2 Real\left(\gamma^2\right)}{\omega^2\mu_r} \tag{2.101}$$

$$\varepsilon_r^{"} = \frac{\mathrm{Im}\left(\gamma^2\right)}{\omega^2\mu_0\mu_r\varepsilon_0} = \frac{c^2\,\mathrm{Im}\left(\gamma^2\right)}{\omega^2\mu_r} \tag{2.102}$$

Where μ_r is 1 since we are working with a non-magnetic material, and $\omega = 2\pi f$ is the angular frequency. We should mention that the imaginary part of the propagation constant which is the phase constant β has a bounded value between ($-\pi$, and π) and this sweeping in its angles occurs due to the analytical expression that used to calculate the phase constant. So, the phase constant must be linearized to avoid instability or divergence in the extracted electrical properties.

There is a limitation in the linearization of $\left(\alpha^2-\beta^2\right)$ in Eq. (2.100) because β was raised to power 2 and added with other quantity. Thus, the linearization is not possible here and that will lead to a bandwidth limitation in the characterization method. To overcome this limitation a numerical solution is suggested in this work. Since the problem is due to the values of β, the linearization must be done for β. Second, the propagation constant γ should be rewritten as follow:

$$\begin{aligned} &real(\gamma)=\alpha \\ &\mathrm{Im}(\gamma)=unwrap(\beta) \\ &\gamma=real(\gamma)+j\,\mathrm{Im}(\gamma)\equiv\alpha+j\beta_{linearized} \end{aligned} \tag{2.103}$$

Unwrap is a *Matlab* function that can be used to linearize the phase constant β or you can build your own function that does the same linearization objective. Hence, you can use the same Eqs. (2.100), (2.101), and (2.102) to compute the complex permittivity.

Indeed, the conductor loss is included in the previous set of equations and its effect on the results relying on the application and the test fixture used for material characterization measurement. Usually, the dielectric constant is less sensitive to the conductor loss than the dielectric loss tangent. For those interested in removing the conductor loss effects from his results, we propose a simple idea to achieve that goal.

All you need to solve this issue is just an extra measurement of the two-port network with the absence of the MUT and usually is called vacuum or air case.

$$\gamma_{vac}=\alpha_c+\alpha_{vac}+j\beta \tag{2.104}$$

Where α_c, and α_{vac} represent the attenuation constant for conductor and vacuum respectively. Since the attenuation constant of the vacuum is $\alpha_{vac}=0$, the attenuation constant of the conductor α_c is now the real part of γ_{vac}. So, by recording α_c and subtract it from Eq. (2.99) we can cancel the conductor loss effect and continue with the same equations to extracted the electrical properties.

In the following, two methods for propagation constant determination are presented in order to use the previous equations to extract the electrical properties of the MUT. In both methods, we assume that we are measuring the responses of the MUT alone, but this is not a practical scenario since usually errors included in the measurements which are coming from the discontinuities sections. So, a calibration technique should be used first to take off the error boxes effects.

2.5.1 ABCD matrix method

This technique uses the propagation constant to extract the electromagnetic material properties. The idea is to measure the MUT's S parameters using a two-port network system. We suppose that the measured S parameters represent the MUT responses. Then the *ABCD* matrix of the MUT can be computed using the relationship between *S* and *ABCD* matrices see Eqs. (2.68), and (2.74).

$$[S]_{MUT} \Rightarrow [ABCD]_{MUT} \tag{2.105}$$

Now, we have the $ABCD_{MUT}$ matrix and benefiting from its correlation with the electromagnetic parameters of the medium of propagation as shown in Eq. (2.106), we can find by simple analytical inversion the propagation constant of the MUT.

$$\begin{pmatrix} A & B \\ C & D \end{pmatrix}_{MUT} = \begin{pmatrix} \cosh(\gamma L) & Z_c \sinh(\gamma L) \\ \dfrac{\sinh(\gamma L)}{Z_c} & \cosh(\gamma L) \end{pmatrix} \tag{2.106}$$

$$\gamma = \frac{\cosh^{-1}(A)}{L} \tag{2.107}$$

When the propagation constant is computed the electrical properties of the MUT can be extracted using Eqs. (2.99), (2.100), (2.101), and (2.102).

2.5.2 T matrix method

The T matrix method is based also on extracting the complex relative permittivity from the propagation constant. The propagation method is computed after several mathematical derivations as demonstrated in the following:

The relationship between *S* and *T* parameters matrices are known, we can then compute *T* matrix of the MUT

$$[S]_{MUT} \Rightarrow [T]_{MUT}$$

$$[T]_{MUT} = \begin{pmatrix} T_{11} & T_{12} \\ T_{21} & T_{22} \end{pmatrix} \quad (2.108)$$

Later the eigenvalues of the matrix should be extracted

$$(\lambda) = eig\left([T]_{MUT}\right) \quad (2.109)$$

Whereas λ as the Eigen-value vector of T_{MUT} which is calculated as:

$$\begin{pmatrix} \lambda_1 \\ \lambda_2 \end{pmatrix} = \frac{\left(T_{11} + T_{22}\right) \pm \sqrt{\left(T_{11} - T_{22}\right)^2 + 4T_{12}T_{21}}}{2} \quad (2.110)$$

Two eigenvalues are existed, by taking the average of the eigenvalues we can determinate the propagation constant using the below expressions:

$$\lambda = \frac{\lambda_1 + \lambda_2}{2} \quad (2.111)$$

$$\gamma = \frac{\ln(\lambda)}{\Delta\ell} \quad (2.112)$$

Where $\Delta\ell$ is the sample length

After that, we can extract the complex permittivity as shown in Eqs. (2.99), (2.100), (2.101), and (2.102)

2.6 CONVERSION METHODS BASED ON UNCALIBRATED S PARAMETERS

In several situations, the calibration of the two-port network can not be performed due to a physical limitation with the test fixture. Hence, the self-calibration techniques could be useful in these cases. In the subsequent two techniques that use uncalibrated S parameters to extract the electromagnetic material properties are proposed.

2.6.1 Short and open method

This method is useful when the measured two-port network has error boxes at two sides as exhibited in Figure 2.14 [20].

Figure 2.14 two-port network with error box configuration

We suppose that the system is symmetric, then the two error boxes that represent the transition parts or the discontinuities as named in Figure 2.9 are electrically and mechanically identical. This technique needs three measurements one for the whole system and two for short and open loaded of the error box. The short and open measurement configuration is already presented in Figure 2.10. We should mention that in section 2.3.3 we reported the SO method for calibration purpose while here our interest is related to material characterization purpose. Thus, in SO calibration method we were interested in computing the calibrated S parameters, while in SO material characterization method we have to compute the propagation constant which is sufficient to extract the complex permittivity. After getting the measurement of the S parameters for the whole system, we can convert S_{total} matrix to $ABCD_{total}$ matrix. Later relying on the below expression w can export the propagation constant of the MUT.

$$\cosh(\gamma L) = \frac{(Z_{oc}+Z_{sc})(A_{total}+D_{total})-(2Z_{oc}\times Z_{sc}\times C_{total})-(2B_{total})}{2(Z_{oc}-Z_{sc})} \tag{2.113}$$

Where Z_{oc}, and Z_{sc} are the impedances of the error box when is loaded with an open and short circuit at the end. These impedances can be calculated using Eq. (2.70).

$$\gamma = \frac{\cosh^{-1}\left(\frac{(Z_{oc}+Z_{sc})(A_{total}+D_{total})-(2Z_{oc}\times Z_{sc}\times C_{total})-(2B_{total})}{2(Z_{oc}-Z_{sc})}\right)}{L} \tag{2.114}$$

From Eqs. (2.99), (2.100), (2.101), and (2.102), and we can extract the complex permittivity

2.6.2 Two transmission line method

The implementation of this method requires two transmission lines with the same physical and electrical properties but with different lengths. If L_1 and L_2, respectively, represent the lengths of the first and the second lines, whereas $\Delta\ell = L_2 - L_1$ is the length difference between both lines, then the uncalibrated measured S parameters of the MUT for the two lines are sufficient to accurately extract the propagation constant.

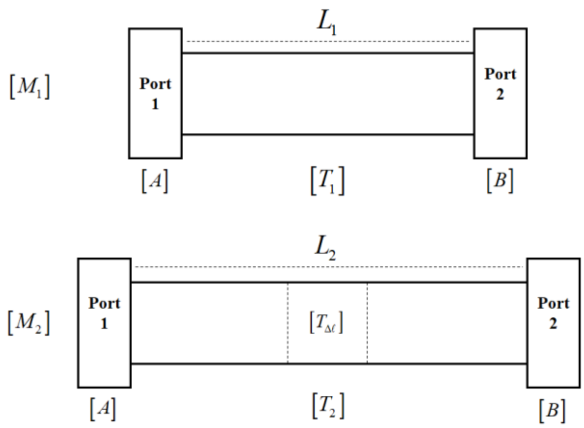

Figure 2.15 two-transmission line measurement configuration

Figure 2.15 exhibits the measurement configurations. S_1 and S_2 represent the uncalibrated scattering parameters of the first and second test fixtures. These scattering parameters can be measured directly using a vector network analyzer VNA.

$$[S_1] \Rightarrow [M_1], [S_2] \Rightarrow [M_2] \tag{2.115}$$

We use the matrices M_1 and M_2 for modeling respectively the WCM of the first and the second fixtures. Whereas the WCM *A* and *B* represent the connector-port section at two sides, respectively. In this case, *A* and *B* are similar since we suppose that the two connector ports are mechanically and electrically identical [21]. In the cascading configuration, we can express the fixture as follows:

$$
\begin{aligned}
[M_1] &= [A][T_1][B] \\
[M_2] &= [A][T_2][B]
\end{aligned}
\tag{2.116}
$$

T_1 and T_2 are the WCM of the first and the second transmission lines. So, the multiplication of the long fixture by the inverse of the short fixture will result in the following:

$$
\begin{aligned}
[M_{12}] &= [M_2][M_1]^{-1} \\
[T_{12}] \equiv [T_{\Delta\ell}] &= [T_2][T_1]^{-1} \\
[M_{12}] &= [A][T_2][A][A]^{-1}[T_1]^{-1}[A]^{-1} \\
[M_{12}][A] &= [A][T_{12}]
\end{aligned}
\tag{2.117}
$$

$T_{\Delta\ell}$ is the WCM for the $\Delta\ell$ section. $\Delta\ell$ has the same characteristic impedance as the long and short transmission lines, but represents the ideal transmission line with no reflections. So, it is simply given by

$$
[T_{\Delta\ell}] = \begin{pmatrix} e^{-\gamma\Delta\ell} & 0 \\ 0 & e^{\gamma\Delta\ell} \end{pmatrix}
\tag{2.118}
$$

Where γ is the propagation constant of the transmission line. The two WCM matrices M_{12} and T_{12} have the same eigenvalues and its eigenvectors are related [22]. As $T_{\Delta l}$ is a diagonal matrix, its eigenvalues are the diagonal elements.

$$
[M_{12}] = \begin{pmatrix} m_{11} & m_{12} \\ m_{21} & m_{22} \end{pmatrix}
\tag{2.119}
$$

If we take into consideration that $M_{12} \equiv T_{MUT}$ in section 2.5.2. Thus, we can follow the same procedure in *T* matrix method in order to extract the complex permittivity using Eqs. (2.9), (2.10), (2.11), and (2.12)and then Eqs. (2.99), (2.100), (2.101), and (2.102).

2.7 SIMULATION VALIDATION

In the previous sections 2.42.5, and 2.6 we described four methods that need calibration measurement in the practical case (i.e., NRW, Retrieval, ABCD matrix, and T matrix) and two methods that do not need calibration measurement (i.e., SO, and tow-line). In order to validate these methods, different situations are simulated and its S parameters used as input in the implemented conversion codes to characterize the MUT.

2.7.1 Comparison of different conversion methods in the ideal case

In the beginning, we start the simulation study with the simplest case where the tow measurement ports are placed at the interface of the MUT to avoid any discontinuities and just getting the MUT's response. In that case, MUT with a length of 15 mm is placed in a coaxial line as shown in Figure 2.16.

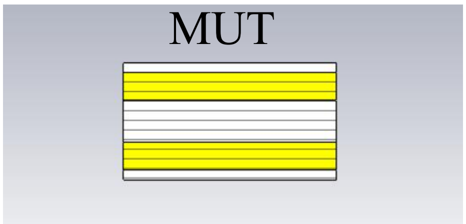

Figure 2.16 Cross-section view of the simulated coaxial line

Now, the FR-4 material is inserted in the coaxial line as MUT. By exporting the S parameters of the simulation and treated it using the implemented conversion algorithms the results of the four conversion methods in extracting the electrical properties of the MUT (i.e., loss-free FR-4, and lossy FR-4) are compared in Figure 2.17, and Figure 2.18.

It is noted in Figure 2.17 the permittivity extraction similarity between the numerical reference and the *ABCD* matrix and *T* matrix methods. For the case of using the NRW conversion method, the simulated result shows correspondence between the extracted and the reference permittivity except two resonances occur at (4.81 GHz, and 9.61 GHz). The resonance phenomenon is already explained in section 2.4.1 by relating the resonance frequencies to the multiple of half guided wavelength of the sample length. In this case, $\lambda_g / 2 = 7.5mm$ the resonance frequencies correspond respectively to ($2\lambda_g / 2$, and $\lambda_g / 2$) and that confirms the theoretical analysis.

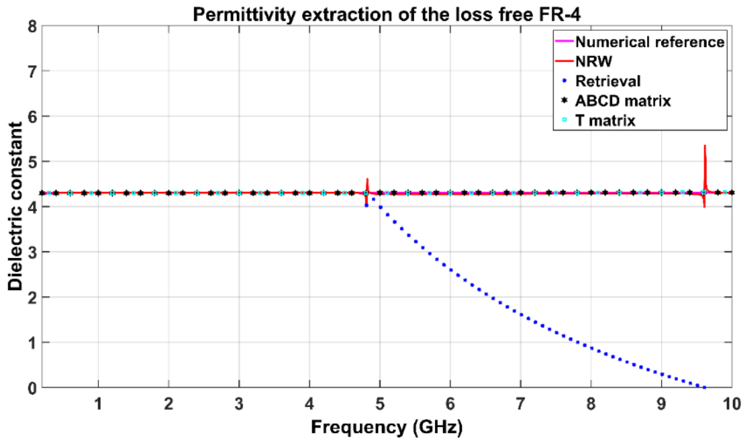

Figure 2.17 Permittivity extraction comparison of the FR-4 loss-free material using different conversion methods

Concerning the Retrieval conversion method, the result is still good till the first resonance frequency. After that, a divergence will happen to destroy the extracted permittivity. This behavior is also related to sample length as reported in section 2.4.2 which make a bandwidth limitation in the technique.

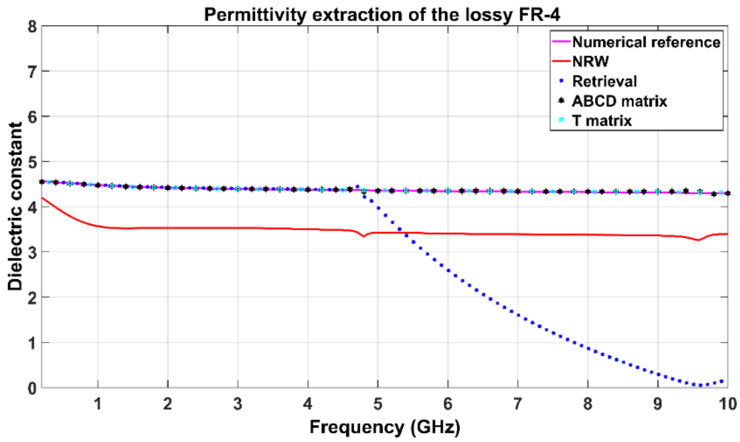

Figure 2.18 Permittivity extraction comparison of the lossy FR-4 material using different conversion methods

Figure 2.18 presents a comparison of the extracted permittivity using different conversion methods for lossy FR-4 material which has permittivity of 4.3 and dielectric loss tangent of 0.025. Here the *ABCD* matrix, *T* matrix, and retrieval conversion methods have the same performance as in loss-free FR-4 material case. The featured response is for the NRW method. The extracted permittivity goes down and the resonances disappear as shown in Figure 2.18. Thus, the simulated result of the NRW technique proves its limitation in characterizing the lossy material as reported in the literature.

2.7.2 Comparison of different Conversion methods after TRL calibration

Usually, in the practical situation, the measurement plane is not situated at the interface of the MUT due to physical or mechanical reasons. So, that means a calibration technique should be applied first to get the responses coming from the MUT alone. In order to simulate the realistic scenario, a coaxial transmission line is designed with discontinuities ports that has a different characteristic impedance comparing to the line as exhibited in Figure 2.19.

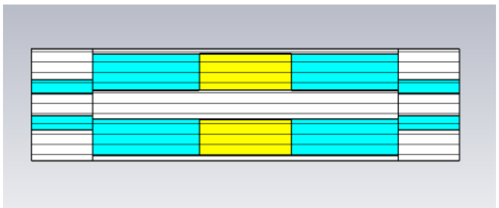

Figure 2.19 Cross-section view of the simulated coaxial line with discontinuities

The simulated MUT has 15 mm as length. Again we simulate the FR-4 loss-free and lossy. The extracted permittivity comparison of the loss-free FR-4 after a TRL calibration is shown in Figure 2.20. From the results, we can conclude the same as the ideal case simulation. The *ABCD* matrix and *T* matrix methods stay with the same efficiency while resonance effect looks higher in the Retrieval and the NRW conversion methods.

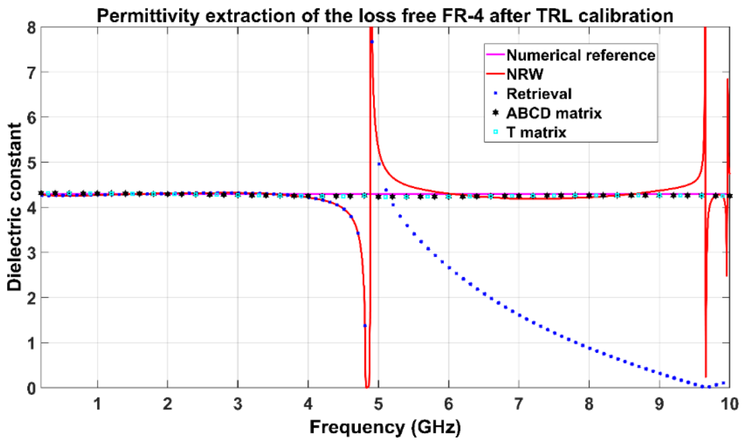

Figure 2.20 Permittivity extraction comparison of the loss-free FR-4 material after TRL calibration using different conversion methods

Furthermore, in Figure 2.21 the extracted permittivity for the case of simulated lossy FR-4 are presented. In this case, we can see the weakness of the NRW conversion method with the characterization of lossy material.

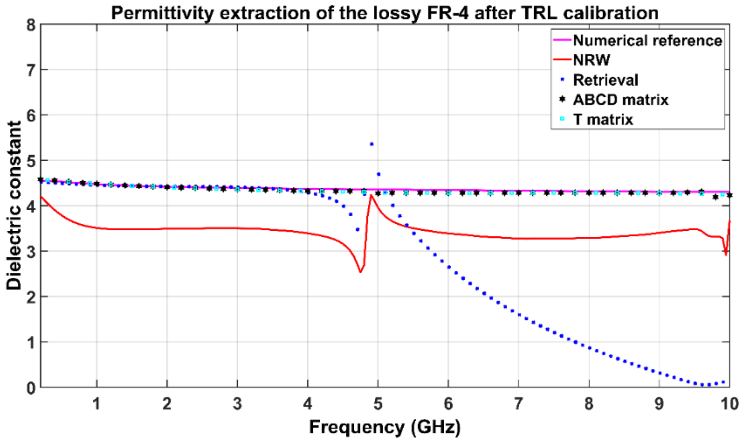

Figure 2.21 Permittivity extraction comparison of the lossy FR-4 material after TRL calibration using different conversion methods

2.7.3 Comparison of self-calibration conversion methods

In the precedent simulation study, we assessed the different conversion methods that require calibrated S parameters. Now, the two conversion methods that use the uncalibrated S parameters to compute the electrical properties will be validated by simulation. As earlier, the two material types of FR-4 are used in the simulation.

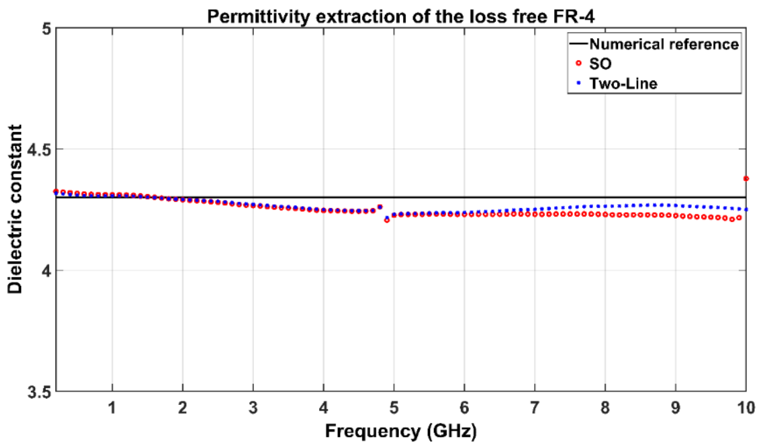

Figure 2.22 Permittivity extraction comparison of the loss-free FR-4 material using SO and Two-Line characterization methods

The result of the extracted permittivity using the SO and the Two-Line methods are displayed in Figure 2.22. Taking into consideration the scale of the plot, a good correspondence between the numerical reference and the extracted permittivity are achieved. Moreover, in Figure 2.23 the same comparison is made with the presence of the lossy FR-4 material. The extraction is still efficient for both conversion methods in spite of characterizing a lossy material.

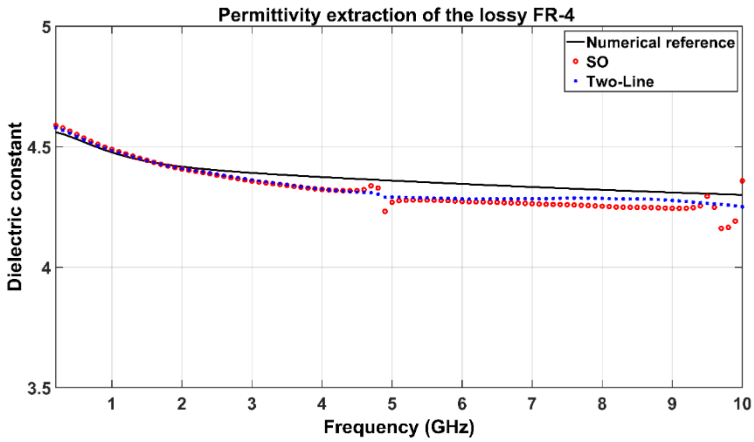

Figure 2.23 Permittivity extraction comparison of the lossy FR-4 material using SO and Two-Line characterization methods

2.7.4 Comparison of the efficient material characterization techniques

In this subsection, we selected the most efficient conversion methods that prove a good performance in the permittivity extraction over a wideband. The four methods are compared in Figure 2.24 when the MUT is the lossy FR-4.

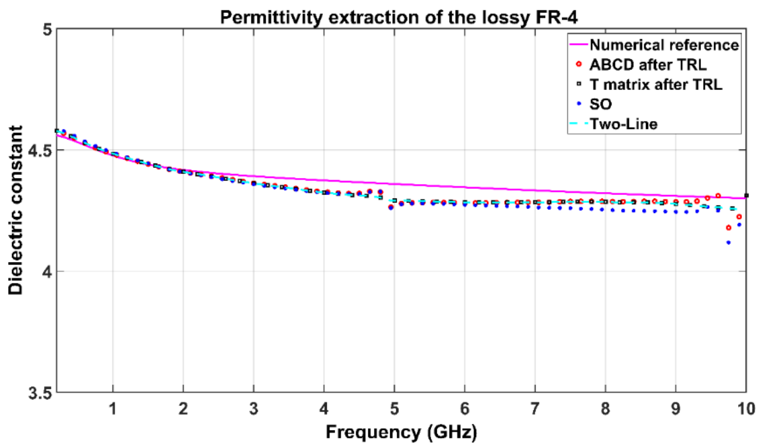

Figure 2.24 Permittivity extraction comparison of the lossy FR-4 material using different conversion techniques

The four methods show good correspondence in the permittivity extraction

2.7.5 Comparison of the extracted dielectric loss tangent using different conversion methods

In the precedent, the real and the imaginary part of the permittivity are given in different techniques. Now, the dielectric loss tangent is just this ratio $\tan(\delta) = \varepsilon_r^{"} / \varepsilon_r^{'}$. The simulated results of the dielectric loss tangent for the lossy FR-4 material are displayed in the figure below. The $\tan(\delta)$ is extracted using the different conversion methods. From the observation comparison presented in Figure 2.25, we can notice the weakness of the NRW method in addition to the Retrieval method. as expected the remaining conversion methods show good performance in the simulated dielectric loss tangent.

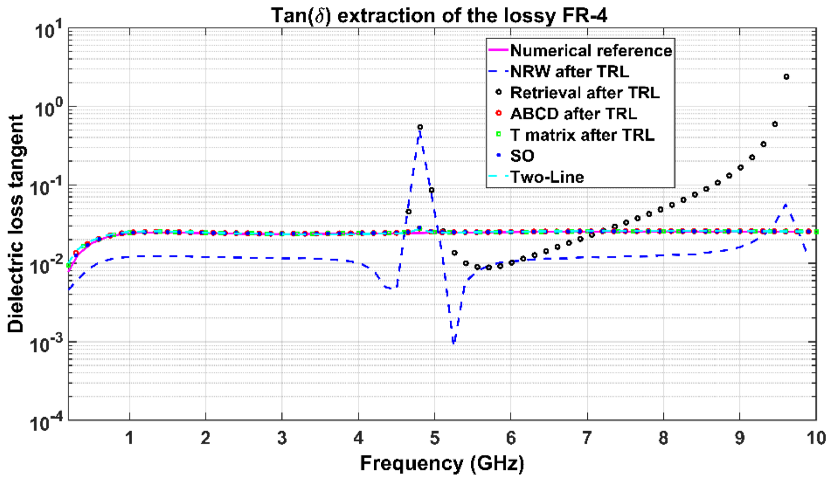

Figure 2.25 Loss tangent extraction comparison of the lossy FR-4 material using different conversion techniques

2.7.6 Error evaluation in the simulation

The error percentage of the simulated results are evaluated based on the numerical reference. The error results for both permittivity and dielectric loss tangent are shown in Figure 2.26, and Figure 2.27 respectively. As expected the ABCD, T matrix, SO, and Two-Line methods have low error percentage in permittivity and dielectric loss tangent extraction. While the NRW has bad results of error percentage with about 20% for permittivity and more than 50% for the dielectric loss. The retrieval method shows bad accuracy in case of dielectric loss tangent determination.

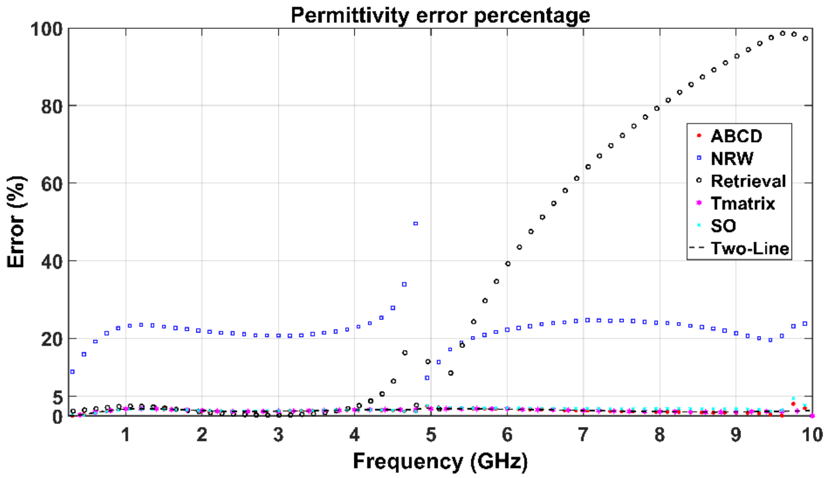

Figure 2.26 Simulated permittivity error percentage of the FR-4 lossy material

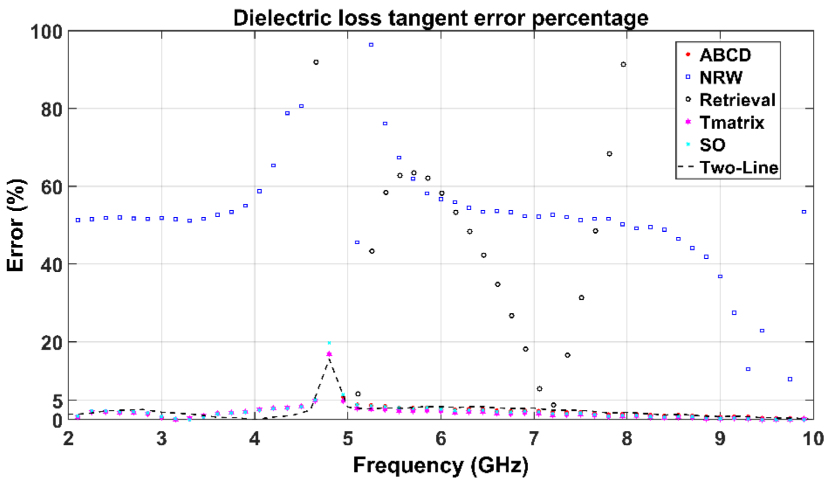

Figure 2.27 simulated dielectric loss tangent error percentage of the FR-4 lossy material

2.8 MEASUREMENT AND APPLICATIONS

2.8.1 3D printing filament characterization

Nowadays, 3D-printing technology is frequently used in diverse applications (e.g., medical, manufacturing, telecommunication and electronics). The availability and low cost of this technology make it popular worldwide; furthermore, it is of great value when traditional fabrication tools fail in terms of complexity and/or cost. 3D printing is used in electromagnetic applications in different Radio Frequency (RF) and Microwave (MW) bands. For example, in electromagnetic compatibility (EMC), low cost and lightweight TEM cells [23][24]Antennas, sensors, and metamaterial designs are some other applications of 3D printing. This wide use of 3D printing in the electromagnetic field necessitates knowledge of the electrical properties of the materials used in printing, such as ABS, PLA, and Semi-Flex.

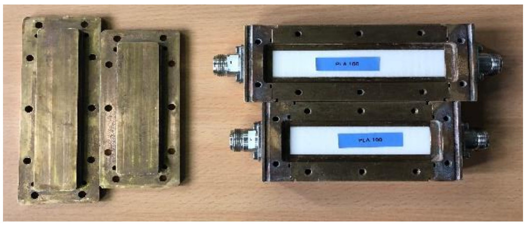

Figure 2.28 Rectangular coaxial text fixtures filled with printed samples

Rectangular coaxial transmission lines are used as a test fixture, as shown in Figure 2.28, with two test space lengths 8 cm and 10 cm. The fixture is made with copper as a conductor and can be filled easily. The samples must fit completely the test space of the fixtures in order to avoid gaps, which affect the accuracy of the MUT’s extracted property results.

Figure 2.29 3D-printed samples different materials and different infill density percentages

In addition to the electrical properties study, we studied the effects of the infill density percentage of the electrical properties because the printing usually does not have 100% of infill density. This will help researchers in the RF and Microwave applications to optimize their designs by using more accurate 3D-printing properties. The prepared samples are shown in Figure 2.29 for three types of plastic materials with three different infill densities: 100%, 50%, and 20%.

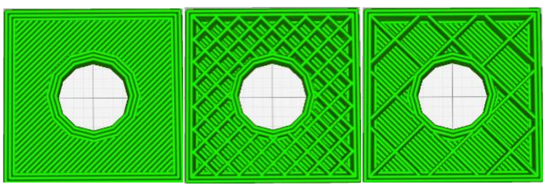

Figure 2.30 Cross-section view of the rectangular sample with 100%, 50% and 20% of infill density

percentages respectively

The cross-section of the rectangle coaxial sample with the infill density percentage is shown in Figure 2.30. In the extant literature, the electrical properties of the 3D printed samples in the presence of the TEM mode is not investigated. The dielectric constant versus frequency (2 MHz - 10 GHz) of the three kinds of plastic samples with 100% infill density is shown in Figure 2.31. All of them are different from each other. PLA relative permittivity is the lowest compared to the ABS and the Semi-Flex ones.

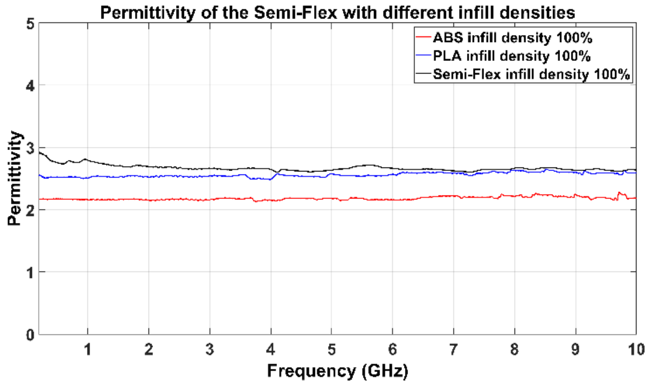

Figure 2.31 Permittivity of the ABS, PLA and Semi-Flex materials

Figure 2.32 shows the dielectric constant when the infill density percentage changed in three cases (100%, 50%, and 20%) with the three MUT (ABS, PLA, and Semi-Flex). The presented results for the dielectric constant while changing the infill density prove a proportional relationship between the infill density percentage and the retrieved relative permittivity. This opens the possibility for dielectric constant tuning by modifying the infill percentage, and this will be very helpful in several RF and microwave applications.

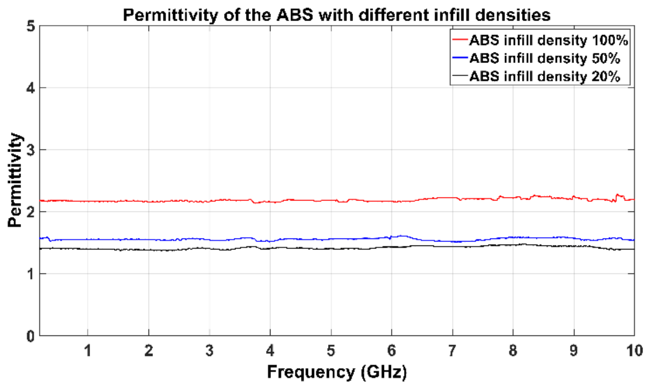

(a)

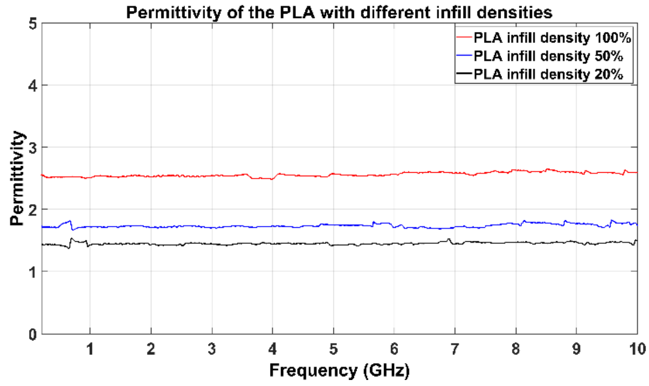

(b)

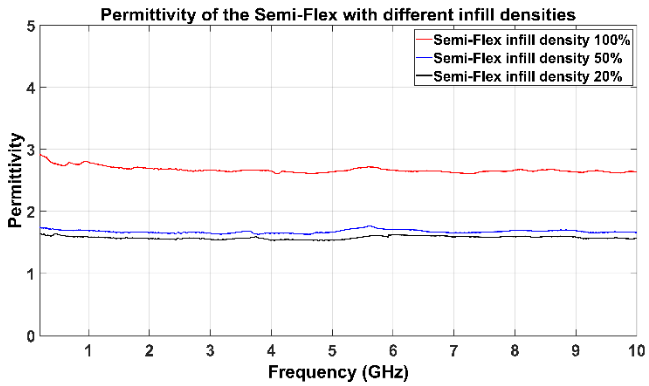

(c)

Figure 2.32 ABS, PLA and Semi-Flex permittivity extraction with infill density variations

On the other hand, Figure 2.33 shows the loss tangent comparison for the plastic material (ABS, Semi-Flex, and PLA) with 100% of infill density. Figure 2.34 exhibits the loss tangent comparison of the three plastic MUT with three different values of infill density percentage.

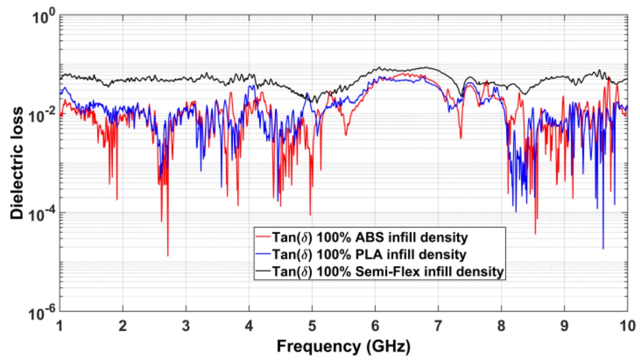

Figure 2.33 Tangent dielectric loss comparison among ABS, PLA and Semi-Flex materials with 100% of infill density

In Figure 2.34, some strange behavior in the variation of the loss tangent appears via higher loss tangent at some frequencies with lower infill density. This response is also found in [25][26] but is not explained. In our view, this phenomenon is due to the limitation of the extraction technique itself. It is known that in the transmission reflection material characterization technique, the permittivity extraction error percentage can be up to 5% while for the dielectric loss tangent, it is up to 10% [27], [10]. Also, Ref. [28] reports that the resolution of the extracted dielectric loss tangent is $\tan(\delta) \approx 0.01$. Thus, the dielectric loss tangent cannot be extracted when the MUT has a low dielectric loss $\tan(\delta) \ll 0.01$. For $\tan(\delta) > 0.01$, the 10% [27][10] error is still there, and it might lead to MUTs with smaller infill densities having a higher dielectric loss compared to MUTs with higher infill densities. By looking at the extracted dielectric loss tangent responses, we note that for dielectric loss values less than 0.01, sharp drops in the dielectric loss value occur. This means the extraction method is inaccurate for dielectric loss values less than 0.01. As mentioned before, the non-resonant material characterization technique has acceptable accuracy over a wide bandwidth while the resonant technique has more accuracy at single frequencies. Therefore, for obtaining more accurate results of the dielectric loss tangent, the resonant material characterization technique should be employed for the dielectric loss behavior investigation at several frequencies.

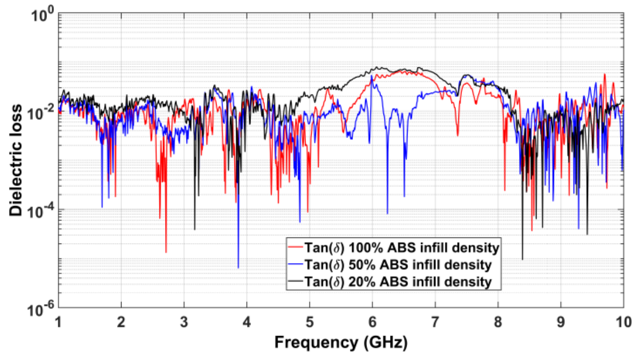

(a)

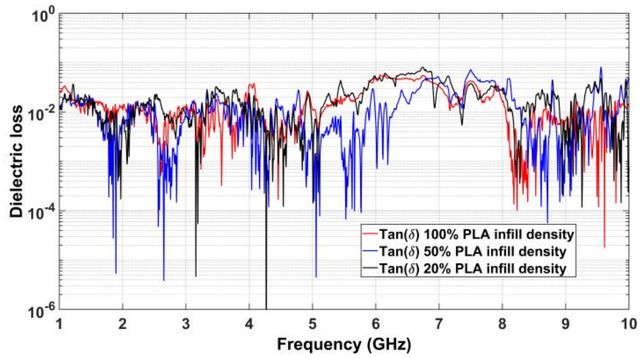

(b)

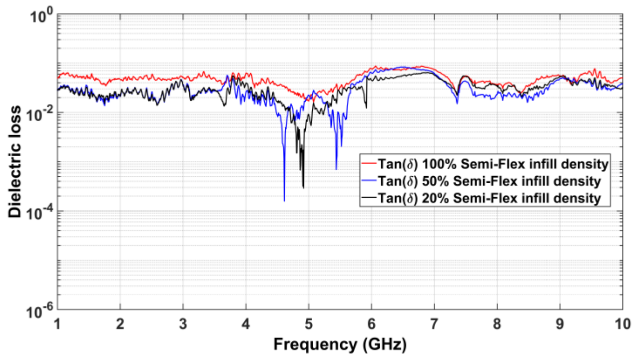

(c)

Figure 2.34 Dielectric loss tangent for ABS, PLA, and Semi-Flex plastic with three infill densities 100%, 50%, and 20%

2.8.2 Sand and soil characterization

In this section the inherent properties of the ground (i.e., sand and soil) are extracted due to is important in different applications and especially in the GPR. The electrical properties are studied in the same frequency range that the GPR usually uses from 1 GHz till 4 GHz.

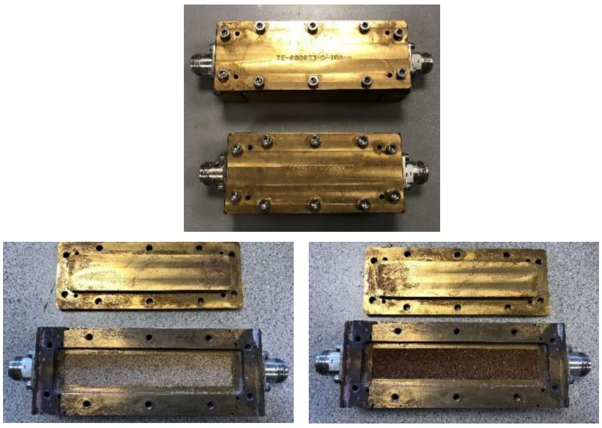

Figure 2.35 Rectangular coaxial fixture filled with soil and sand

The Two-Line technique is used to extract the electromagnetic properties from the measured S parameters. The rectangular coaxial transmission line is also used as a test fixture as shown in Figure 2.35. The permittivity of both sand and soil are exhibited in Figure 2.36. It is noticed that the soil has higher permittivity than the soil.

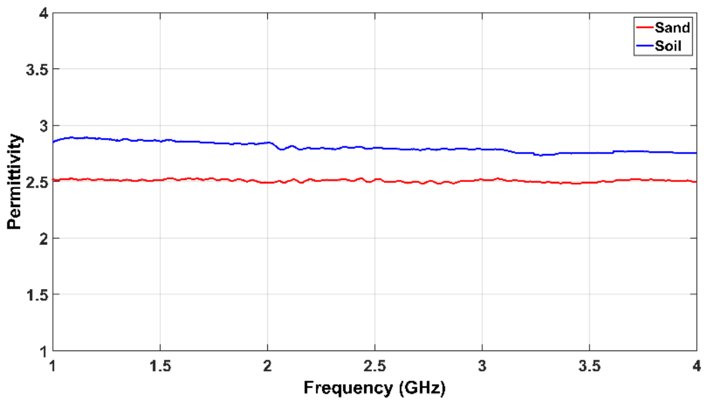

Figure 2.36 Permittivity extraction comparison of the sand and the soil

The dielectric loss tangent of the sand and the soil are displayed in Figure 2.37. It is remarked from the result that the soil has a higher loss tangent than the sand. In addition, it is observed the difference in the extracted curves of both materials, and that due to the limitation of the used technique in the determination of the loss tangent. As explained earlier, the accuracy of the extraction decreases when the loss tangent of the MUT decreases. Since the soil has a higher dielectric loss, its extracted dielectric loss will be more accurate.

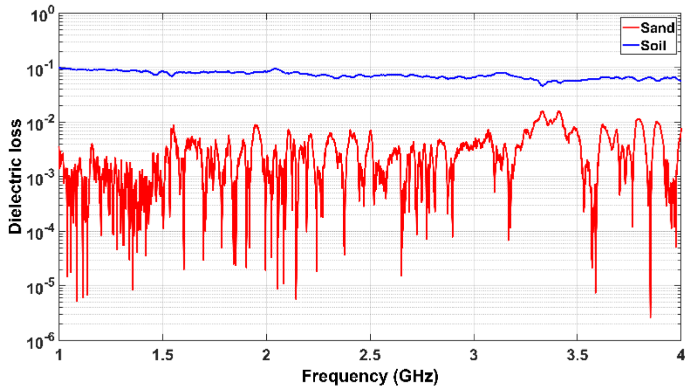

Figure 2.37 Tangent loss comparison between the sand and the soil

We should mention here that the permittivity of the medium might not be the same everywhere. It varies depending on the chemical composition, humidity, and heterogeneity of the medium. That means, taking two soil samples from two different places is not necessarily getting the same electrical properties. So the electromagnetic properties should be studied first for each working field.

2.8.3 Permittivity Extraction of Moist Sand & soil

A study of the dielectric constant of soil and sand in term of humidity variation is performed over a wide frequency range. The moisture content of the soil/sand can be calculated as a percentage, with respect to completely dry soil/sand, using Eq. (2.120) [29]:

$$MC\% = \frac{W_2 - W_3}{W_3 - W_1} \times 100 \tag{2.120}$$

In Eq. (2.120), W_1 is the weight of the fixture, W_2 the weight of moist soil/sand plus the fixture, and W_3 is the weight of dry soil/sand plus the fixture. Eq. (2.120) helps compute the humidity of the soil/sand from the different weights for the empty fixture, the fixture with the dry soil/sand and the fixture with the moist soil/sand.

In order to measure the different weights, a scale with 0.02 g of accuracy is used, as shown in Figure 2.38 The weights of the empty fixtures are measured first, followed by the weights of the fixtures when filled with dry soil/sand. Later, other weight measurements are taken when a specific quantity of water is added to the soil/sand already in the fixture using a pipette.

Figure 2.38 High-precision scale

To change (decrease) the humidity percentage of the MUT, the fixture containing the moist soil/sand is placed over a heat bed to let a portion of the water vaporize before re-measuring the weight, and from it re-calculate the new humidity percentage Figure 2.39. For each new percentage, the permittivity estimation is then done.

Figure 2.39 Heat bed to control the humidity of the MUT

The soil sample is taken from the Northeast of Lebanon, whereas the sand sample is taken from Beirut sea beach. The extracted permittivity of the two samples for different humidity percentages are given in Figure 2.40, and Figure 2.41, respectively. The two figures show that the permittivity of dry sand is about 2.5, and that of soil is about 4.

For both sand and soil, the permittivity increases with increasing humidity percentage. This is expected since the relative permittivity of water is around 80. The relative permittivity of sand reaches 20 when its humidity is 27%. The relative permittivity of soil increases to 30 when its humidity is 50%.

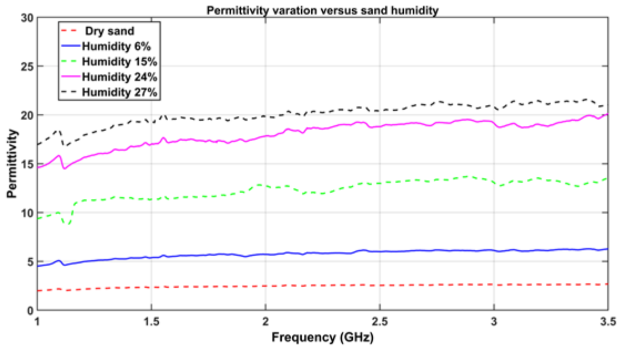

Figure 2.40 Permittivity variation in term of sand humidity

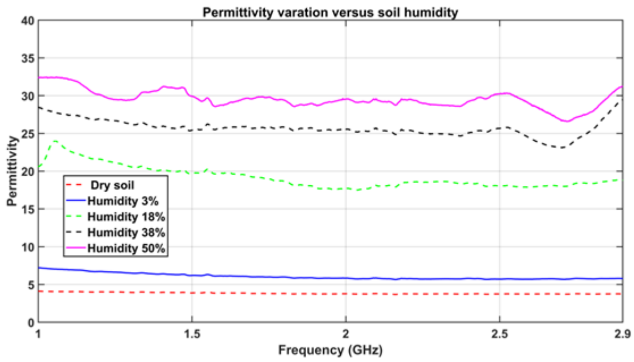

Figure 2.41 Permittivity variation in term of soil humidity

In brief, it is clearly noted that the water content of soil and sand greatly affects the permittivity

2.8.4 Error evaluation in the measurement

In order to evaluate the error percentage of the extracted permittivity, we used the measured S parameters of the rectangular coaxial lines in case of MUT absence. The absence of the MUT means measuring the electrical properties of the air.

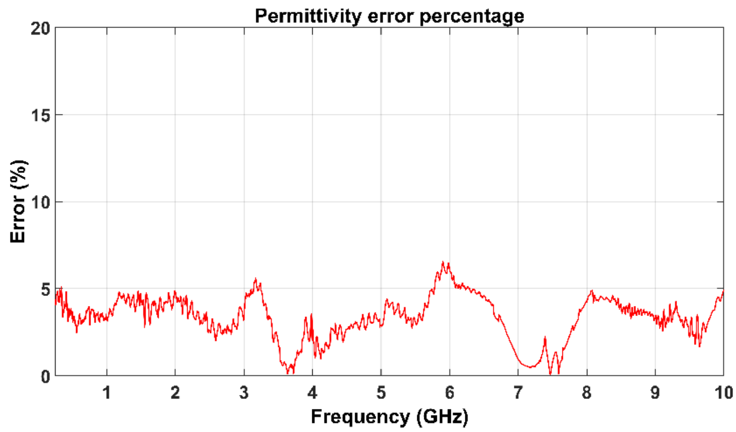

Figure 2.42 Error evaluation percentage of the extracted measured permittivity

So, if we suppose the permittivity of the air is 1 we can then evaluate the permittivity error by theoretical and measurement comparison. The error percentage is shown in Figure 2.42. the plots prove an acceptable error percentage over all the frequency band. The error percentage of the dielectric loss is not evaluated Since we do not have a refrence material.

2.9 CONCLUSION

In this chapter, the electromagnetic material characterization techniques are interpreted in general. Under the non-resonant techniques category, the transmission/reflection method is reported in details. Indeed, the extraction of the electrical properties procedure requires two main steps: calibration, and conversion methods. Two calibration methods (i.e., TRL and SO) are reported in details. Moreover, six conversion methods (i.e., NRW, Retrieval, ABCD matrix, T matrix, SO, and Two-Line) are presented to extract the electrical properties from the measured S parameters. Two of these techniques have a self-calibration property. Also, the validation of the different methods is investigated using simulated and measurement studies. In addition, the evaluation of the error percentage is done in simulation and measurement. Since we are interested in the characterization of underground targets, we selected several materials to characterize including plastic and ground in order to use its properties to enhance the detection of the buried objects.

2.10 REFERENCES

[1] Chen, Lin-Feng, C. K. Ong, C. P. Neo, V. V. Varadan, and Vijay K. Varadan. *Microwave electronics: measurement and materials characterization*. John Wiley & Sons, 2004.

[2] Baker-Jarvis, James, R. Geyer, and Paul Domich. "Improvements in transmission line permittivity and permeability measurements." In *Conference on Precision Electromagnetic Measurements*, pp. 232-233. IEEE, 1990

[3] Baker-Jarvis, James, Eric J. Vanzura, and William A. Kissick. "Improved technique for determining complex permittivity with the transmission/reflection method." *IEEE Transactions on microwave theory and techniques* 38, no. 8 (1990): 1096-1103.

[4] Nicolson, A. M., and G. F. Ross. "Measurement of the intrinsic properties of materials by time-domain techniques." *IEEE Transactions on instrumentation and measurement* 19, no. 4 (1970): 377-382.

[5] Keysight Technologies, "Specifying Calibration Standards and Kits for Keysight Vector Network Analyzers Application Note," 2016.

[6] Rumiantsev, Andrej, and Nick Ridler. "VNA calibration." *IEEE Microwave Magazine* 9, no. 3 (2008): 86-99.

[7] Padmanabhan, Sathya, Peter Kirby, John Daniel, and Lawrence Dunleavy. "Accurate broadband on-wafer SOLT calibrations with complex load and thru models." In *61st ARFTG Conference Digest, Spring 2003.*, pp. 5-10. IEEE, 2003.

[8] Engen, Glenn F., and Cletus A. Hoer. "Thru-reflect-line: An improved technique for calibrating the dual six-port automatic network analyzer." *IEEE transactions on microwave theory and techniques* 27, no. 12 (1979): 987-993.

[9] J. E. Schutt-aine, "Automated Microwave Measurements TRL Calibration," pp. 1–4.

[10] Chung, Jae-Young. "Broadband characterization techniques for RF materials and engineered composites." PhD diss., The Ohio State University, 2010.

[11] C. B. S, "Parameters Conversion Table.pdf," vol. 42, no. 2, pp. 205–211, 1994.

[12] Pozar, David M. Microwave engineering. John Wiley & Sons, 2009.

[13] Weir, William B. "Automatic measurement of complex dielectric constant and permeability at microwave frequencies." *Proceedings of the IEEE* 62, no. 1 (1974): 33-36.

[14] Rothwell, Edward J., Jonathan L. Frasch, Sean M. Ellison, Premjeet Chahal, and Raoul O. Ouedraogo. "Analysis of the Nicolson-Ross-Weir method for characterizing the electromagnetic properties of engineered materials." *Progress In Electromagnetics Research* 157 (2016): 31-47.

[15] Vicente, Alexandre Natã, Gustavo Maciulis Dip, and Cynthia Junqueira. "The step by step development of NRW method." In *2011 SBMO/IEEE MTT-S International Microwave and Optoelectronics Conference (IMOC 2011)*, pp. 738-742. IEEE, 2011.

[16] Arslanagić, S., Troels Vejle Hansen, N. Asger Mortensen, Anders Heidemann Gregersen, Ole Sigmund, Richard W. Ziolkowski, and Olav Breinbjerg. "A review of the scattering-parameter extraction method with clarification of ambiguity issues in relation to metamaterial homogenization." *IEEE Antennas and Propagation Magazine* 55, no. 2 (2013): 91-106.

[17] Chen, Xudong, Tomasz M. Grzegorczyk, Bae-Ian Wu, Joe Pacheco Jr, and Jin Au Kong. "Robust method to retrieve the constitutive effective parameters of metamaterials." *Physical review E* 70, no. 1 (2004): 016608.

[18] Smith, D. R., D. C. Vier, Th Koschny, and C. M. Soukoulis. "Electromagnetic parameter retrieval from inhomogeneous metamaterials." Physical review E 71, no. 3 (2005): 036617.

[19] R. C. Rumpf, "Homogenization and Parameter Retrieval," pp. 124–140, 2018.

[20] Li, Yin, and Lei Zhu. "A short–open calibration method for accurate de-embedding of 3-D nonplanar microstrip line structures in finite-element method." *IEEE Transactions on Microwave Theory and Techniques* 66, no. 3 (2017): 1172-1180.

[21] Huynen, Isabelle, Catherine Steukers, and Fabienne Duhamel. "A wideband line-line dielectrometric method for liquids, soils, and planar substrates." *IEEE Transactions on Instrumentation and Measurement* 50, no. 5 (2001): 1343-1348.

[22] Hasar, U. C., G. Buldu, M. Bute, J. J. Barroso, T. Karacali, and M. Ertugrul. "Determination of constitutive parameters of homogeneous metamaterial slabs by a novel calibration-independent method." *AIP Advances* 4, no. 10 (2014): 107116.

[23] A. Al Takach, F. Ndagijimana, J. Jomaah, and M. Al-Husseini, "3D-printed low-cost and lightweight TEM Cell," *Proc. - 2018 Int. Conf. High Perform. Comput. Simulation, HPCS 2018*, no. 1, pp. 47–50, 2018.

[24] Al Takach, Ali, Fabien Ndagijimana, Jalal Jomaah, and Mohammed Al-Husseini. "Position optimization for Probe Calibration Enhancement Inside the TEM Cell." *In 2018 IEEE International Multidisciplinary Conference on Engineering Technology (IMCET)*, pp. 1-5. IEEE, 2018.

[25] Le, Taoran, Bo Song, Qi Liu, Ryan A. Bahr, Stefano Moscato, Ching-Ping Wong, and Manos M. Tentzeris. "A novel strain sensor based on 3D printing technology and 3D antenna design." *In 2015 IEEE 65th Electronic Components and Technology Conference (ECTC)*, pp. 981-986. IEEE, 2015.

[26] Mirzaee, M., and S. Noghanian. "High frequency characterisation of wood-fill PLA for antenna additive manufacturing application." *Electronics Letters* 52, no. 20 (2016): 1656-1658.

[27] Moukanda Mbango, Franck. "Contribution à la caractérisation des matériaux utilisés en microélectronique radiofréquence." PhD diss., Grenoble 1, 2008.

[28] Krupka, Jerzy. "Frequency domain complex permittivity measurements at microwave frequencies." *Measurement Science and Technology* 17, no. 6 (2006): R55.

[29] B. Craze, “Soil Survey Standard Test Method Soil Moisture Content,” *Soil Survey Standard Test Method Soil Moisture Content*, 1990. [Online]. Available:https://www.environment.nsw.gov.au/resources/soils/testmethods/mc.pdf.

Chapter 3: Permittivity Extraction Using TEM Cell Technique

Contents

3.1 INTRODUCTION

The closed TEM cell is commonly used in the electromagnetic compatibility tests. In this chapter, the design and investigation of the use of TEM cells in electromagnetic material characterization are developed. The purpose of this study is to prepare a suitable test fixture for electrical properties extraction of medium or targets that are not able to characterized using the regular transmission line fixture. This chapter presents the TEM cell theory and its different types. The design and fabrication of different cells are discussed. In addition, two models of closed TEM cells are proposed for material characterization application. Furthermore, simulation and measurement validations of the use of the closed TEM cell in the material characterization are performed. Two types of landmines are electrically characterized by extracting their effective permittivity that represents the landmine and its surrounding environment.

3.2 TEM CELL THEORY

3.2.1 Introduction

The TEM cell was first introduced by Myron L. Crawford at the National Bureau of Standards in 1974 [1]. Crawford realized that the electronic or electromechanical systems in the open systems would affect the level and number of potentially interfering signals. For this reason, he presented the TEM cell for establishing uniform electromagnetic fields in a shielded environment. The TEM cell can be used for E-field probes calibration, E-field immunity radiation test and emission radiation measurement from a product. TEM cells are used in final compliance certification tests. There are many EMC standards which require a TEM cell as (IEC 61000-4-3) for radiated susceptibility and radiated emission tests and (SAE J1752-3) for Integrated Circuits (IC), Micro Electro-Mechanical Systems (MEMS) devices and PCBs [2].

TEM cell is shielded enclosure, thus the inside electromagnetic field is isolated from the outer electromagnetic noise and at the same time does not produce electromagnetic radiation in the environment. The electromagnetic test, in general, required an anechoic chamber for better accuracy in the results but this expensive chamber does not available easily. The TEM cell can obviate the requirement of the anechoic chamber in many electromagnetic tests but, it has several limitations which depend on the application and the size of equipment under test (EUT). Furthermore, TEM cell does not need an antenna to create the EM field in contrast to the anechoic chamber. In pursuance of reaching the desired field strength at the EUT, the necessary input power in TEM cell much lower compared with the antenna in the anechoic chamber [3].

TEM cell is a kind of mixing between a coaxial rectangular transmission line and stripline. Some references called the main part of the cell rectangular coaxial strip line (RCTL) [4]. The TEM cell supports the propagation of the TEM mode within its operating bandwidth. The main drawbacks for the TEM cell are the limitation of the test space, and the operating frequency band [5]. The TEM cell's size has an inverse proportional relationship with the frequency of interest and, at higher frequencies, the resonance of higher-order modes limits the usable bandwidth.

Indeed, four conditions should be taken in consideration when the design process of a TEM cell is being, maximum usable test cross-sectional area, maximum upper useful frequency limit, minimum cell impedance mismatch or voltage standing wave, and maximum uniformity of EM field pattern characteristic of the cell [6].

3.2.2 Physical description

The TEM cell in the physical shape is a combination between rectangular coaxial line and stripline. The cell consists of three main parts the connectors, the transition part, and the rectangular coaxial line. This cell serves a broadband linear phase and amplitude transducer [7]. The outer conductor is extended to a rectangular box, and the inner one is changed to a flat metal board. In addition, the inner conductor or the septum as is known acts as the positive conductor and the outer one acts as the ground.

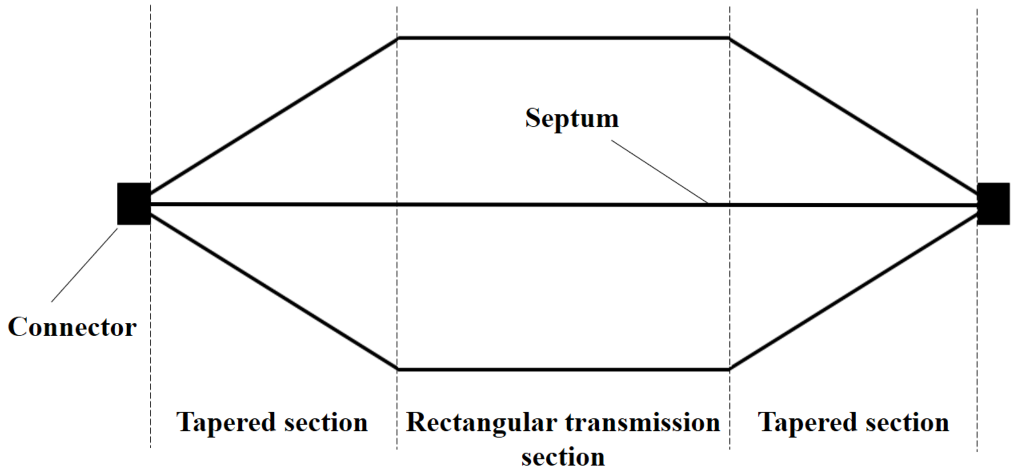

Figure 3-1 Side view of the physical shape of the TEM cell

By looking in the figure above we can see the different parts of the TEM cell, the tapered section must be designed to match the characteristic impedance between the connectors and the rectangular transmission area. This matching is very important to transfer the maximum power from the first port to the end. Usually in the test of the electronic equipment one port connected to the signal and the other one connected to the load. Furthermore, the size of the TEM cell related directly to the usable frequency range

The size of the EUT which can be placed inside the TEM cell should not exceed one-third of the distance between the septum and the outer conductor since the uniformity of the EM field is centered in this region [3].. Several modifications are possible for the cell that can be helpful upon the application, if the septum is vertically offset two zones of unequal size can be created, consequently an asymmetric TEM cell being constructed. This lead to enlarge the EUT's size that can be tested without increasing the total size of the cell and without decreasing its upper useful frequency [4]. The TEM cell is available in different forms open and closed. The open TEM cell is like the closed cell in its structure but without the sidewalls to avoid the complexity of the window and keeping the construction simple. The open cell is most popular and cheaper than the closed cell. On the other hand, the closed cell has the isolation advantage from external EM in comparison with the open cell.

The major design considerations of the typical TEM cell [1]:

- Maximize usable test cross-sectional area.
- Maximize upper useful frequency limit.
- Minimize cell impedance mismatch or voltage standing wave ratio.
- Maximize uniformity of EM field pattern characteristic of the cell.

3.2.3 Electrical description

In fact, the TEM cell converts the radially directed electric field from the coaxial line to the uniform electric fields in the tri-plate section [5]. To adapt this conversion between these tows parts a transition region is needed to link them which is the tapered section. Hence this device is utilized as a uniform EM field's standard creation in a shielded location. The cell is supported the TEM mode as the main propagation EM fields and this is a positive point for the cell in increasing the accuracy of the test [8]. The EM wave inside the TEM cell formed by orthogonal electric (E) and magnetic (H) fields which are perpendicular to the direction of propagation. The E field is perpendicular to the septum while the H field is parallel to the septum and both of them are uniform in the rectangular transmission section. Also, we should take into consideration the effects of the EM field due to any change in the size or the physical shape of the TEM cell. For instance, the E field above and below the septum in the symmetric TEM cell is different than the E field in the asymmetric cell, undoubtedly the characteristic impedance is also changed [4]. Any mismatch occurred in the structure appears in the standing waves. Therefore the distribution of the E field loses the uniformity and the amplitude of the EM filed will not be the same at different points inside the cell [5]. For this reason, lots of researches were done to study the field distribution in the TEM cell. Spiegel used a Quasi-static method to calculate the field distributing on the cross-section of TEM Cells. Hese calculated the distribution of the electrical field when the DUT is placed into TEM Cells using the FDTD method. Moreover, the operating frequency band of the TEM cell is restricted by its physical size and the test space too. So, to enhance these limitations several development methods are put forward as asymmetric TEM cell, TTEM cell, GTEM cell and so on [9].

The EM fields propagated in transverse mode inside the cell as plane waves with free space wave impedance of 377 ohms. The E field (v/m) at the middle working space of the TEM cell is given by [2]:

$$E = \frac{V}{d} = \frac{\sqrt{pZ_0}}{d} \tag{3.1}$$

Where V is the rms voltage on the septum in Vlot, d is the separation between the lower or upper wall and septum in meter, Z_0 is the characteristic impedance of the TEM cell which should be designed to reach 50 Ω, and p is the power flowing through the septum conductor of the cell in watt.

For a practical case the previous equation is modified as below:

$$\mathrm{E} = \frac{\sqrt{\mathrm{pZ_0}}}{\mathrm{d}} \mathrm{C_E} \tag{3.2}$$

Where C_E is the correction factor for the average field strength over the volume of the EUT derived from the analysis of the field distribution over the cross-section of the cell. Thus, by measuring the power flowing through the septum, the E-field can be calculated for known values of d and C_E. Also, Cai and Costache in [61] proposed an empirical expression for the electric field of the areas under test is given as:

$$E\left(l + l^{'}\right) = \frac{1}{b} = \sqrt{\frac{\left(S_{in}^2 k_1 + 2S_{in} k_2 + k_1\right) z_0 P_{in}}{S_{in}^2 k_2 + 2S_{in} k_1 + k_2 - 2(S_{in}^2 - 1) e^{2\alpha(l+l^{'})} \cos\left[\phi_L + \frac{4\pi f(l)}{c}\right]}} \tag{3.3}$$

Where

$$S_{in} = \frac{1 + \left|\Gamma_L\right| e^{-2\alpha l}}{1 - \left|\Gamma_L\right| e^{-2\alpha l}},$$

$$k_1 = 1 - e^{4\alpha(l+l^{'})},$$

$$k_2 = 1 + e^{4\alpha(l+l^{'})}, \tag{3.4}$$

$$\phi_L = \tan^{-1}\left(\frac{2X_L Z_0}{R_L^2 + X_L^2 - Z_0^2}\right)$$

Where $l^{'}$ is the length of the observed position, P_{in} is the net power, which flows in the TEM cell, and $Z_L = R_L + jX_L$ is the terminal load impedance

3.2.4 Characteristic impedance

Tippet investigated the natural impedance of the rectangle coaxial line using the conformal mapping method and the singular integral method. Tanaka got a result of TEM Cells' natural impedance and potential distributing in Cells making use of boundary element method. The line and the tapered transitions are designed to have a characteristic impedance of 50 ohms along the entire length, to ensure minimum VSWR.

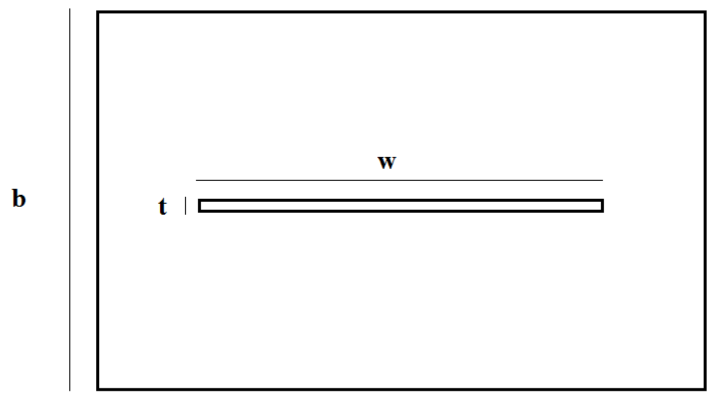

Figure 3-2 Cross-section view of the TEM cell

The cells can be designed using experimental modeling and the approximate equation for the characteristic impedance of the shielded strip line [52]:

$$Z_0 \simeq \frac{94.15}{\sqrt{\varepsilon_r}\left[\frac{w}{b\left(1-\frac{t}{b}\right)}+\frac{C^{f'}}{0.0885\varepsilon_r}\right]}(ohms) \tag{3.5}$$

Where ε_r is the relative dielectric constant of the medium between the conductors, $C^{f'}$ is the fringing capacitance in picofarads per centimeter, *w*, *b*, and *t* are shown in the figure Figure 3-2. Furthermore, Tippet and Chang [62] proposed an equation for the characteristic impedance of the TEM cell.

$$Z_0 = \frac{376.7}{4\left[\frac{a}{b}+\frac{2}{\pi}\ln\left(\sinh\frac{\pi g}{2b}\right)\right]-\frac{\Delta c}{\varepsilon_0}} \tag{3.6}$$

Where *a* is the TEM cell's width, *b* is the TEM cell's height, and *g* is the side gap between the septum and the outer conductor. These parameters are the length of the TEM cell dimension in meter, Δ_C is the fringe capacitance between the edges of the center plate and the sidewalls of the TEM cell. If the ratio of *a* and *b* is larger than 1, $a/b > 1$, we can then ignore the term of $\Delta C/\varepsilon_0$.

3.2.5 Cut off frequency

Since the TEM cell is an expanded rectangular coaxial transmission line, the useful frequency range should be defined. In general, The TEM cell propagates the TEM modes at all frequencies which has no low cut off frequency but, in the reality, there are limitations in the useful frequency band due to the higher-order modes and their resonances. The higher-order TE and TM modes appear after their cut off frequency. So, the TEM cell work from DC till cut off frequency which related directly to the TEM cell's dimensions. Obviously, we can understand the importance of the cut off frequency computing of the higher-order modes. In fact, the tapered section of the TEM cell consists of the septum and the outer conductor and because of having different folding angles the outer and the inner conductor have Δs as length difference. So along the outer conductor, the travel time for a wave is longer by $\Delta t = \Delta s/c_0$. These field distortions give rise to higher mode propagation and thus affect the uniformity of the field inside the cell increasingly at higher frequencies [3]. Weil and Gruner obtained numerical solutions for the normalized cut-off frequencies of the initial odd higher-order modes as a function of the inner conductor width. Wilson and Ma outlined some approximate analytical expressions for determining the cut-off frequencies of the first few higher-order modes using a small gap assumption. Zhang and Fu calculated the higher-order modes cut-off frequencies in various symmetric TEM cells with the transmission line method. The $TE_{m,2n,}$ and $TM_{m,2n}$ mode cutoff frequencies are unaffected by the presence of the inner conductor for the symmetric cell, therefore, can be conveniently obtained by the rectangular waveguide formula. When n is odd, the maximum *E* field in the *x*-direction along the center conductor occurs, and capacitive coupling exists between the center stripe and the vertical sidewalls, resulting in lowering of cut-off frequencies compared with the waveguide for TE cases [12].. The equation for determining the cutoff frequency for any higher-order mode, in general, is given by [1]:

$$f_{Cmn} = \frac{c\sqrt{b^2m^2 + W^2n^2}}{2bw} \quad (3.7)$$

Where c is the velocity of propagation of light 3×10^8 m/s, b and W are shown in Figure 3-2 and m and n are integers related to the half-sine variations of the field in the vertical and transverse directions.

3.2.6 Resonance frequency

As we mentioned before at low frequencies the TEM cell allows for the TEM mode to propagate, at high frequency several TE and TM modes start to propagate. In fact, each higher-order mode reflected at some points within the taper section where becomes too small to propagate the mode. The propagating energy in the higher-order mode undergoes multiple reflections, end to end, within the cell until it is dissipated. As well as the TEmn and TMmn modes in the cell have one cut off frequency fc_{mn} related to them and multiple sets of resonance frequencies. So, the computation of the cut off frequencies can be used to enhance the prediction of the resonance frequencies. Moreover, the presence of higher-order mode resonances in the cell disturbs the amplitude and the direction of the EM field inside the TEM cell. There is coherence between the TEM cell's body and its resonance frequencies since the TEM cell acts as a cavity for several frequencies. This phenomenon happens when the resonance condition satisfied. Thus every effective length of higher-order mode is equal p times the half guide wavelength the resonance will occur at this frequency. The higher-order mode resonances appear at sharply defined frequencies. Thus, could exist frequency windows between resonances where field variations become predictable and TEM cell usage is still quite valid. Hill analyzed TEM cell resonances based on experimental data from different cells. The resonance frequencies are expressed as [13]:

$$f_{rmnp}^2 = f_{cmn}^2 + \left(\frac{pc}{2L_{mn}}\right)^2 ; p > 0 : m, n \geq 0 \quad (3.8)$$

Lmn, is adjusted to get a good agreement between measured and calculated frequencies for between two and four resonances, depending on the mode. *Lmn* is related to the cell dimensions by the equation:

$$L_{mn} = L_c + X_{mn} L_E \tag{3.9}$$

Where Lc is the length of the uniform-cross-section center part of the cell, L_E is the length of the two tapered ends of the cell, and X_{mn} is the fraction of the two ends included in the value of Lmn. The problem with frequency resonances is restrained the operating frequency band of the TEM cell. To increase the upper frequency limit of the TEM cell with respect to the cavity effects, absorbing material can be placed on the walls in order to minimize resonances and reflections. Deng made a number of methods, including using a slotted outer wall, placing magnetic loops or ferrite elements and pasting absorbing materials inside the cell, to expand the testing bandwidth of a TEM cell [8]. Also Dai, Wang and Su proposed a structure of a binary TEM cell, which has been realized by the Laplace Instrument Ltd, to expand test space by using asymmetric structure.

3.3 OPEN TEM CELL

The open TEM cells can be symmetric (the septum is exactly in the middle of the structure) or asymmetric (the septum is shifted towards the upper or lower ground plane). In this work, two open TEM cells are designed and implemented, where one is symmetric and the second is asymmetric. More details presented in the following sections.

3.3.1 Characteristic impedance

In this work, the open TEM cell is studied as two small striplines connected to a large middle one via two transition parts . Referring to Figure 3-3, the small striplines are the ones directly connected to the N-type connectors at the two ends. The size of these small striplines is dictated by the size of the N-type connector. The middle large stripline has the septum as its metal trace.

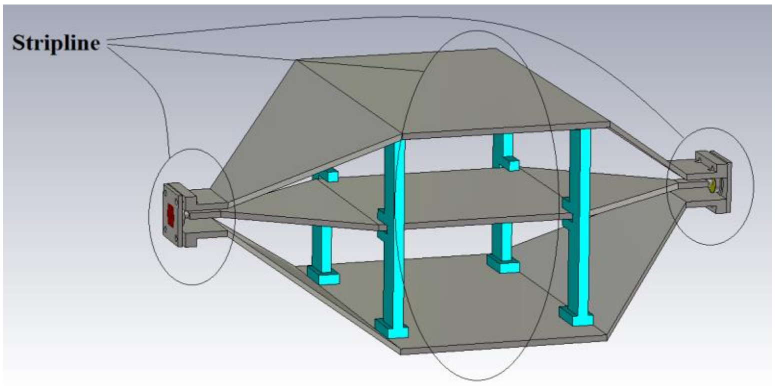

Figure 3-3: The three striplines of the TEM cell

So, by using the impedance formula of the stripline we can then design the two small and the large striplines to achieve 50-Ω impedance matching. Since the open TEM cells can be symmetric and asymmetric, the characteristic impedance of the symmetric and asymmetric striplines should be discussed.

Figure 3.4 shows the symmetric configuration of the stripline.

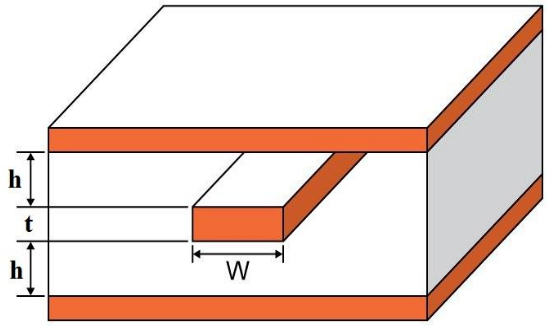

Figure 3-4 the symmetric stripline configuration

The impedance equation of the symmetric stripline is given as follow [14]:

$$Z_{0,ss1} = \frac{60}{\sqrt{\varepsilon_r}} \ln\left(\frac{4b}{\pi D}\right),$$

$$\text{where } b = 2h + t, \tag{3.10}$$

$$D = \frac{W}{2}\left\{1 + \frac{t}{\pi W}\left[1 + \ln\left(\frac{4\pi W}{t}\right)\right] + 0.551\left(\frac{t}{W}\right)^2\right\}$$

$Z_{0,SS1}$ is the impedance of the symmetric stripline, h is the distance between the septum and the top ground, t is the thickness of the covered plate and W is the width of the metal trace. We can use this equation when one of these conditions is satisfied

$\left(\frac{W}{b} < 0.35\right), \left(\frac{t}{b} \leq 0.25\right) and \left(\frac{t}{W} \leq 0.11\right)$.

For the asymmetric case, the stripline configuration is displayed in Figure 3-5.

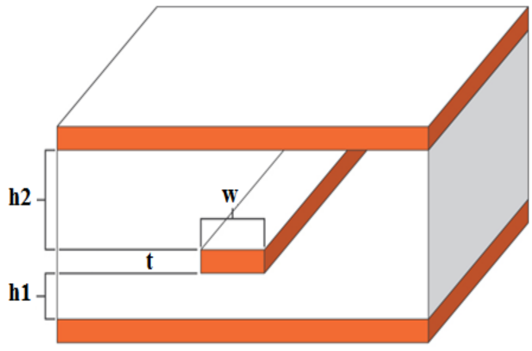

Figure 3-5 the asymmetric stripline configuration

The characteristic impedance of the asymmetric stripline is expressed as follow [14]:

$$Z_{0,AS} = \frac{1}{\varepsilon_r} \times \left[Z_{0,SS(\varepsilon_r=1,b=h_1+h_2+t)} - \Delta Z_{0,air} \right]$$

where,

$$\Delta Z_{0,air} = 0.0325\pi Z_{0,air}^2 \times \left(0.5 - \frac{1}{2}\frac{2h_1+t}{h_1+h_2+t} \right)^{2.2} \left(\frac{t+W}{h_1+h_2+t} \right)^{2.9},$$

$$Z_{0,air} = 2 \times \left[\frac{Z_{0,SS(\varepsilon_r=1,b=h_1)} Z_{0,SS(\varepsilon_r=1,b=h_2)}}{Z_{0,SS(\varepsilon_r=1,b=h_1)} + Z_{0,SS(\varepsilon_r=1,b=h_2)}} \right],$$

$$Z_{0,SS} = \frac{\eta_0}{2\pi\sqrt{\varepsilon_r}} \times \ln\left(1 + \frac{8b}{\pi W'}\left[\frac{16b}{\pi W'} + \sqrt{\left(\frac{16b}{\pi W'}\right)^2 + 6.27} \right] \right), \tag{3.11}$$

$$W' = W + \frac{t}{\pi}\ln\left[\frac{e}{\sqrt{\left(\frac{t}{4b+t}\right)^2 + \left(\frac{\pi t}{4(W+1.1t)}\right)^m}} \right], \text{ and}$$

$$m = \frac{6b}{3b+t}$$

ε_r is the relative permittivity of the stripline substrate, t is the metal trace thickness, h_1 is the distance between the septum and the lower ground plane, h_2 is the distance between the septum and the upper ground plane, W is the metal trace width and $Z_{0,SS}$ is one of the commonly used set of equations for a symmetric stripline. $Z_{0,SS(\varepsilon r = 1;\, b = h1)}$ is the impedance of the symmetric stripline with air as the dielectric and having a total thickness b equal to h_1, and $Z_{0,SS(\varepsilon r = 1;\, b = h2)}$ with air as the dielectric and having total thickness b equal to h_2

3.3.2 Design

Relying on the previous equations for computing the characteristic impedance of the stripline, two different open TEM cells are designed. The first one is a symmetrical cell as shown in Figure 3-6. It is 26 cm in length, 10.3 cm in height and

17 cm in ground width, denoted *Wg*. The thickness of the septum is 3 mm. The TEM cell is designed using the CST studio software.

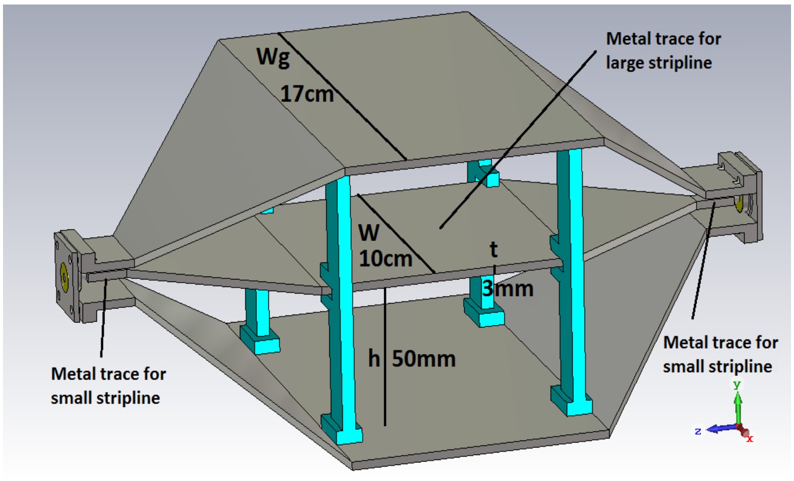

Figure 3-6 The model of the open TEM cell design

The seconde one is the asymmetric TEM cell which is obtained by having the septum closer to one of the two ground planes. The asymmetric TEM cell offers additional test space by increasing the distance between the septum and the ground plane on one side. It can also enhance the operational bandwidth in several cases. Figure 3-7 exhibits the design model and the dimensions of the asymmetric TEM cell.

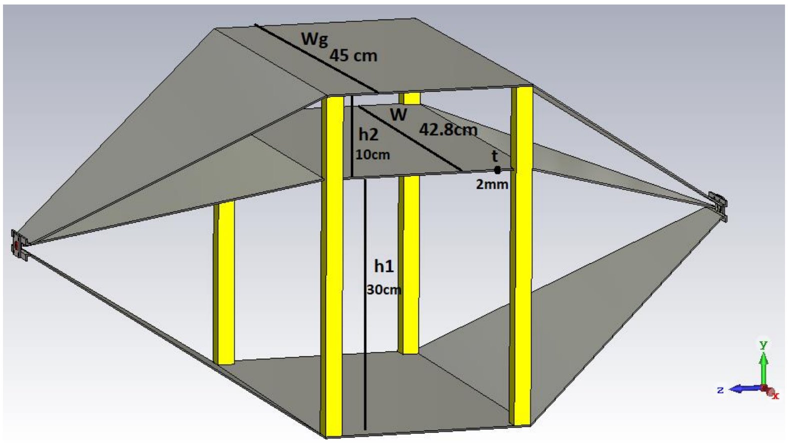

Figure 3-7 The model of the asymmetric open TEM cell design

3.3.3 Fabrication and results

Benefiting from the 3D-printing technology, the first design of the open TEM cell is fabricated. The fabrication process starts by printing the TEM cell parts using the inexpensive 3D printer Micromake D1. This 3D printer is based on the fused deposition modeling (FDM) technology, and the acrylonitrile butadiene styrene (ABS) filament is used. The permittivity of the used ABS material is 2.2 as reported in chapter 2. The plastic parts are then covered with aluminum tape, except for the four holders, to avoid shorting the septum to the ground plates. Pieces of paper clips are used to assemble the whole body of the open TEM cell. Figure 2.8 shows the different parts of the cell before the assembly.

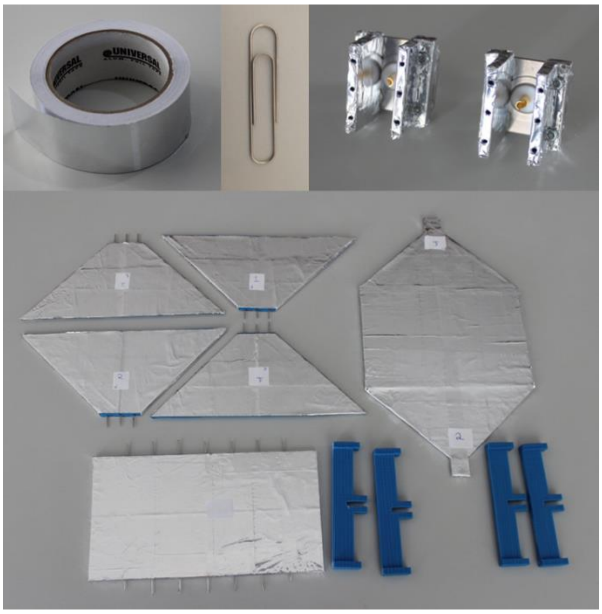

Figure 3-8 The TEM cell parts covered with aluminum tape

The 3D printed cell weighs 0.37 Kg in total, and its material costs less than 20 USD. This is twenty times less expensive than a similar conventional metal cell (with material and fabrication cost estimated at about 400 USD) not to count the very expensive CNC machines used. It is also worth mentioning that fabricating a metal cells requires a worker with special expertise in dealing with metals and CNC machines, whereas 3D printing is becoming more prevalent especially as the price of 3D printers has become as low as 150 USD. The final design after assembly is shown in Figure 3-9. The size of the TEM cell that can be 3D printed does not depend on the size of the 3D printer since the TEM cell can be fabricated in small parts and then assembled as was done with the presented cell.

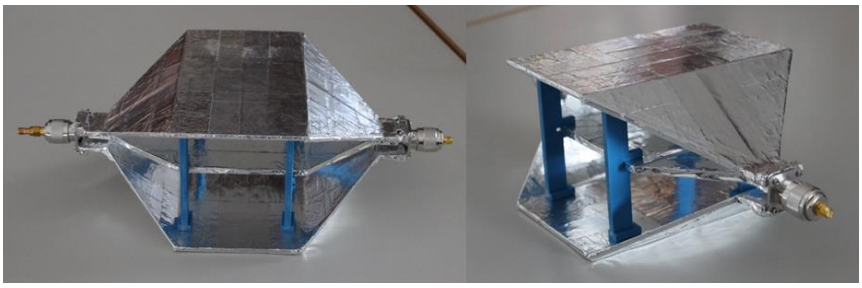

Figure 3-9 The assembled open TEM cell

The S-parameters of the symmetric open TEM cell are measured using a network analyzer and are compared to their simulated counterparts. Figure 3-10 compares the simulated and measured S parameters, where operation is proven in the frequency range from DC to 1.6 GHz. This is considered where S_{11} stays below -10 dB, and S_{21} stays better than -3 dB. The slight differences between the measured and simulated results are due to fabrication inaccuracies.

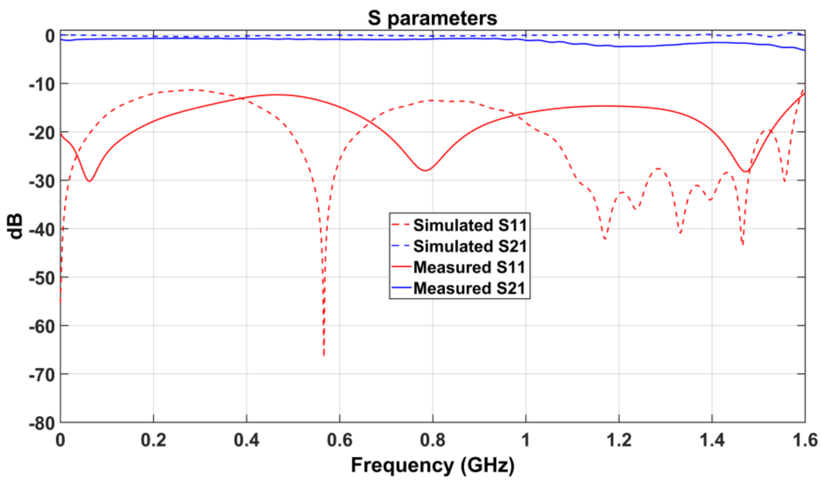

Figure 3-10 The S parameters results of the open symmetric TEM cell

The fabrication of the second design of the open asymmetric TEM cell is done using the traditional fabrication method of cutting and bending of aluminum plates. In order to assemble the three aluminum parts together, four wood sticks are incorporated at the corners. A photo of the fabricated asymmetric TEM cell is shown in Figure 3-11. This cell has the dimensions of 86*45*40 cm^3.

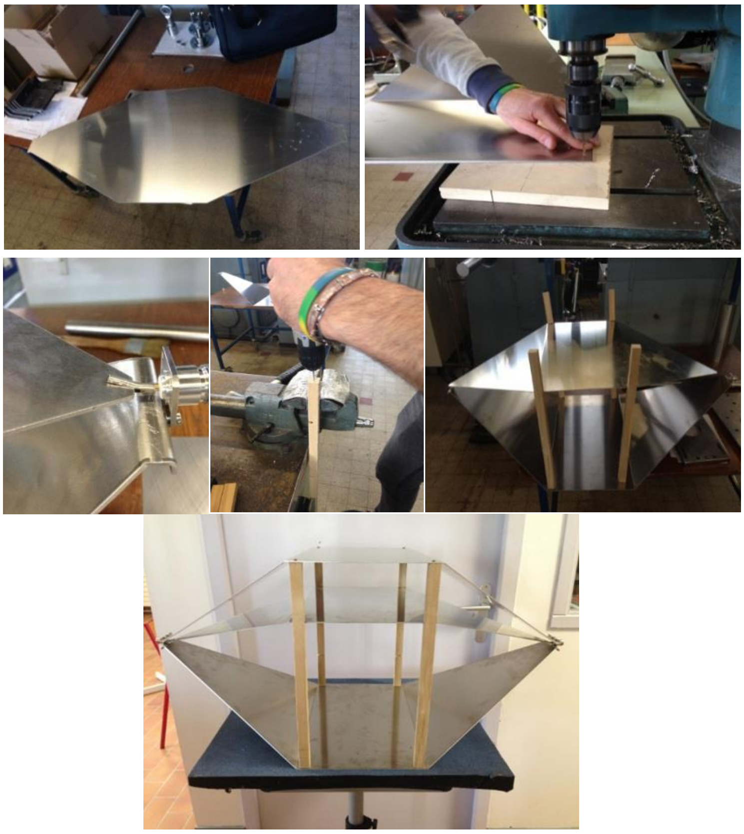

Figure 3-11 The fabricated model of the assymetric TEM cell using traditional method

The measured and the simulated S parameters plots of the asymmetric TEM cell are given in Figure 3-12. The plots demonstrate a good agreement between the measured and the simulated results, in addition to operation over the frequency range from DC to 650 MHz.

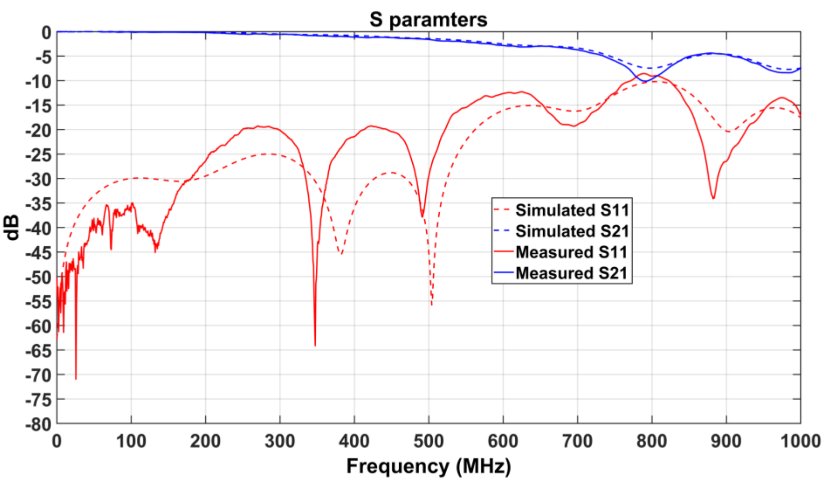

Figure 3-12 The S parameters result of the asymmetric TEM cell

3.4 CLOSED TEM CELL

We selected the closed TEM cell as a test device for material characterization application of underground targets, since it has the isolation advantage from outside EM noise in addition to the compatible test space with MUT's size. In order to prepare the measurement fixture of the MUT, two different models of the closed TEM cell were proposed in this section.

3.4.1 First model

Relying on the different material characterization techniques that discussed in chapter 2, we propose the first model of closed TEM cell that is compatible in use with the Two-line technique to extract the electrical properties of the MUT.

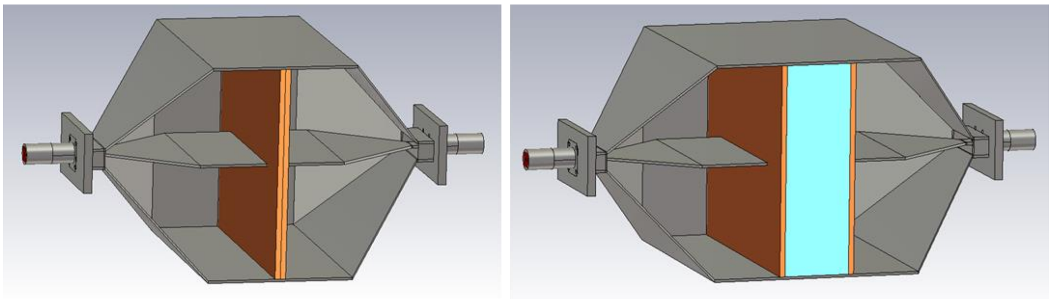

Figure 3-13 The side view of the designed TEM cells without the cover plate

The first model consists of two closed TEM cells having a length difference of 5 cm. In addition, this model uses simultaneously the septum holder as an MUT container. Figure 3-13 exhibits the side view of the designed TEM cells without the cover plate. The blue color in Figure 3-13 represents the MUT zone which has 5*19*16.2 cm^3 of volume test space. In order to implement the simulation study, the model was created using the *CST Studio* software.

Figure 3-14 The design of the closed TEM cell using *Fusion 360* software

In fact, the previous design cannot be fabricated directly due to fabrication machine limitation. Thus, another design was created using *Fusion 360* which is special mechanical software. This software can study the feasibility of the model by taking into consideration the material type, bending and cutting effects. The new design is displayed in Figure 3-14. The design consists of several parts to facilitate the fabrication process. Furthermore, the TEM cell's parts can be connected by screws that give an advantage point if we want to change easily any part.

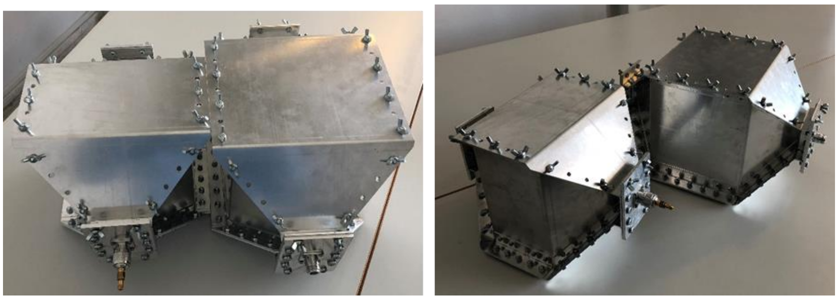

Figure 3-15 The fabricated closed TEM cells

The fabricated closed TEM cells are shown in Figure 3-15. Specific screws are put on top of the TEM cell for quick open to fill or change the MUT.

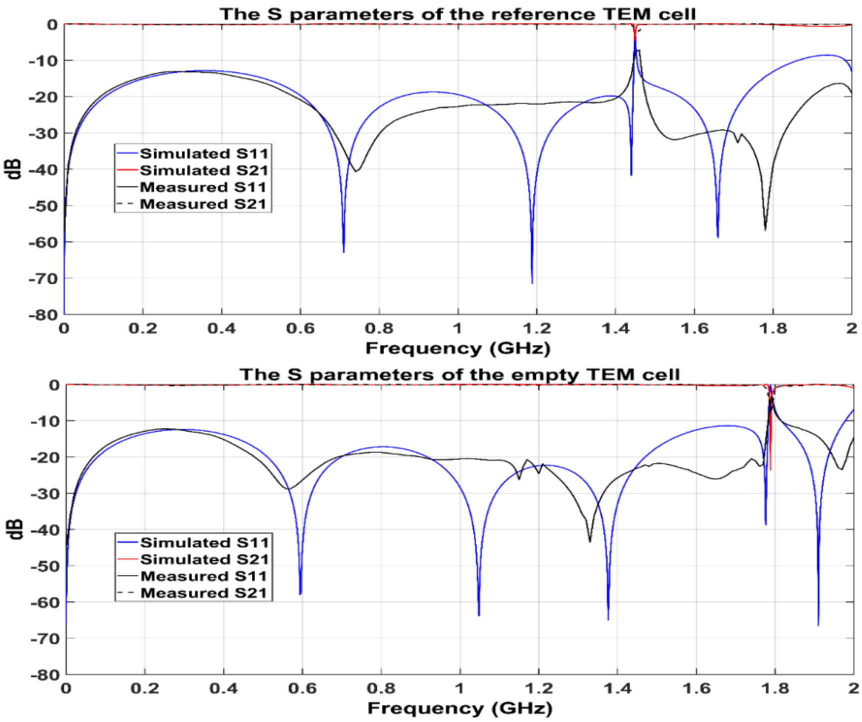

Figure 3-16 The comparison of the simulated and the measured S parameters for the two TEM cells

The S parameter measurement for the two fabricated TEM cells was taken using a VNA. The comparison between the simulated and the measured S parameters results are exposed in Figure 3-16. The results prove a good similarity between the simulation and the measurement in term of the operational bandwidth and the higher order mode resonance frequencies.

3.4.2 Second model

A new model was developed to overcome the MUT length limitation found in the first model. In addition, the new model has the implementation ability for different calibration and conversion methods due to its physical design. The new model is created also using the *Fusion 360* software and shown in Figure 3-17.

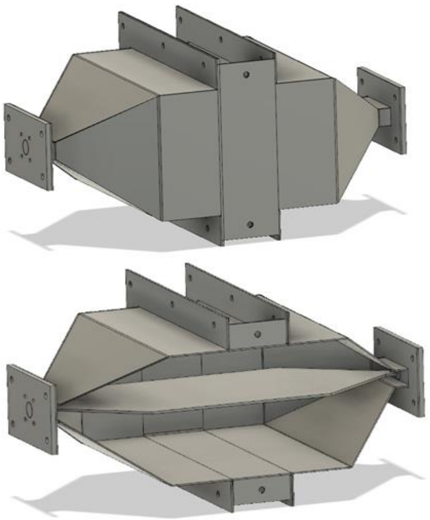

Figure 3-17 The second model of the closed TEM cell

This model consists of three main parts the two transition parts and the middle section. The middle section represents the MUT container which can be removed when measuring the thru configuration or connected with the desired MUT sample length when measuring the line configuration. The fabricated design is exhibited in Figure 3-18.

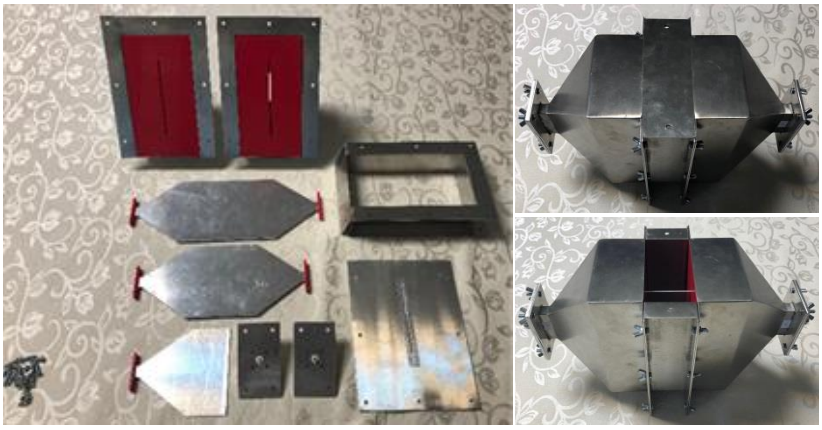

Figure 3-18 The fabricated new model of TEM cell

The S parameters of two cases were simulated and measured the first case is the thru configuration when connected the transition parts to each other directly and the second case is when connected the transition parts via the middle part. The results of the S parameters are plotted in Figure 3-19, the results shows good convenience between the simulation and the measurement.

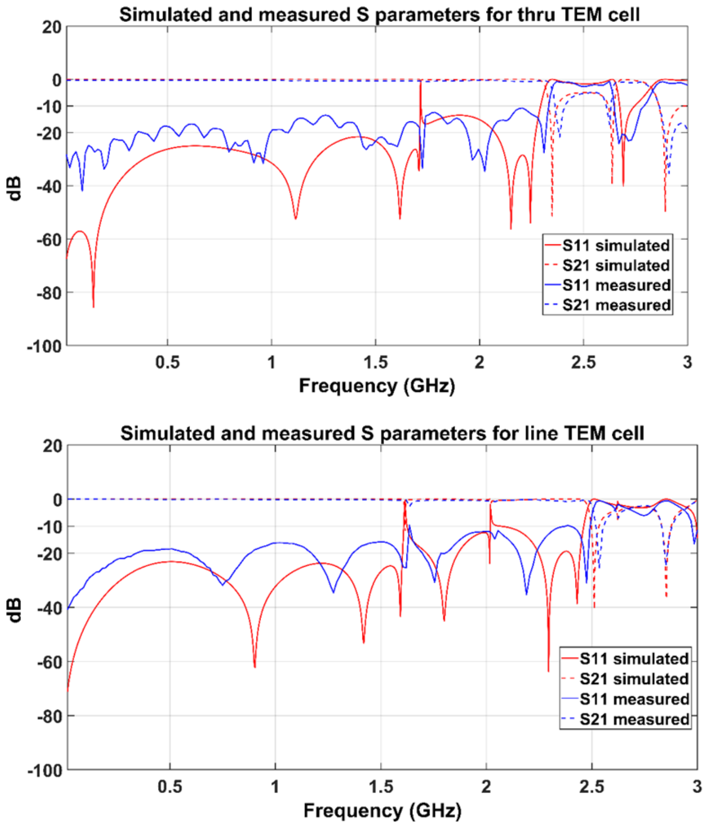

Figure 3-19 The S parameters comparison between the simulation and the measurement for thru and line configuration

3.5 HIGHER ORDER MODE SUPPRESSION TECHNIQUES

The operational bandwidth limitation of the TEM cells is due to the resonances of the higher order TE and TM modes. The TE modes are the first several higher order modes to appear in a TEM cell as the frequency increases above the useful measurement range of the cell. TE modes first appear at frequencies above their respective cut-off frequencies. Since the cell terminations are not matched for higher order mode propagation, the cell becomes a resonant cavity and the energy in a particular TE mode is highest at frequencies corresponding to the cavity resonances. At the resonant frequencies corresponding to TE modes, the magnetic field in the longitudinal direction is relatively high, and the TEM mode field distribution is significantly disturbed. TE mode resonant frequencies can be estimated using analytical methods.

3.5.1 Mode suppressing techniques

One method to suppress the TE modes is to reduce the current that flows in the transverse plane in order to suppress the longitudinal magnetic field. To achieve that several modifications on the physical shape of the TEM cell should be made, but the modification should not change the TEM cell test topology, the cell size, the normal propagation of the TEM mode and the shielding of the cell. With these requirements in mind, several methods for suppressing higher order modes are proposed, as described in Table 3-1 [15].

Table 3-1 Different methods for suppressing TE modes in TEM cells

1.Slotted walls 	PCBs with parallel traces in the longitudinal direction are used to line the outer walls in order to prevent current from flowing in the transverse direction. Currents flowing in longitudinal direction are not affected.
2.Slotted septum 	Slots are cut in the septum in order to form parallel traces in the longitudinal direction and suppress any currents flowing in the transverse direction.

3.Two layer septum with resistors 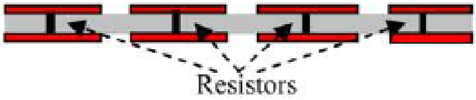	The septum is constructed using two-layer printed circuit boards with a dielectric layer in the middle. Resistor of total 2 ohms are placed between the layers of the septum for each strip in order to achieve a 45-degree phase angle between the capacitance formed by the two-layers and the connecting resistors at the resonances occurred at around 1 GHz. Thus, for each septum strip, two 1-ohm resistors are used. Currents flowing in the vertical direction are attenuated by these resistors.
4.Resistors between slotted traces 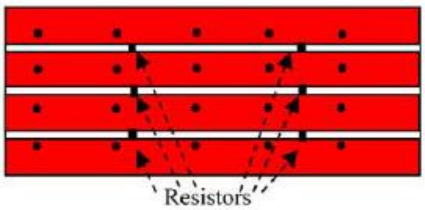	Tow 80-ohm resistors are placed in parallel between each slot connecting the adjacent traces for both the septum and the outer walls. The resistors are mounted evenly across the slots and the total resistance from edge to edge on each board is around 200 ohms. Currents flowing in the transverse plane are attenuated by these resistors.
5.Magnetic loops near the walls 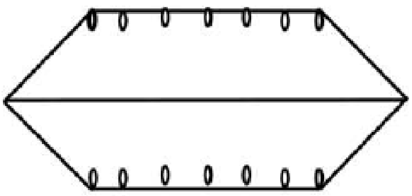	Resonant magnetic loops are placed in the corners near the floor of the cell with the magnetic dipole moment parallel to the longitudinal direction in order to cancel out some of the magnetic field in the longitudinal direction
6.Ferrite tiles in the corners 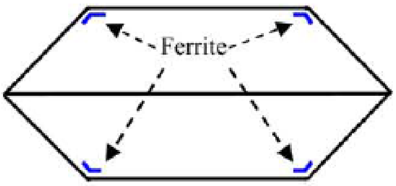	Ferrite tiles are positioned parallel to the side walls of the cell at the corners in order to absorb energy in the magnetic field associated with higher order modes
7.Long narrow ferrites 	Long narrow ferrite strips are positioned along the longitudinal direction on the walls, so that TEM mode is less affected than TE modes

8.Absorbing material loading 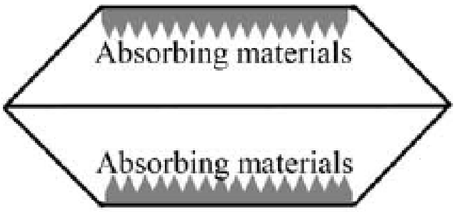 	RF-absorbing materials are placed inside the TEM cell to dampen the cell's high-frequency higher order mode resonances. The limitations of this method are a decrease in the usable testing volume as well as reduced TEM mode field.
9.Active mode cancelation	Consist of two semi-circular loops mounted transversally on vertical walls. A feedback system tailored for the targeted resonance is used to drive the probes in order to produce an electric field of equal magnitude to that of the excited resonance, but 180-degree phase difference.

3.5.2 Simulation for suppressing techniques

Referring to Table 3-1 different techniques were proposed to suppress the higher order modes. In this work, we implemented numerically two techniques of them using *CST Studio* software.

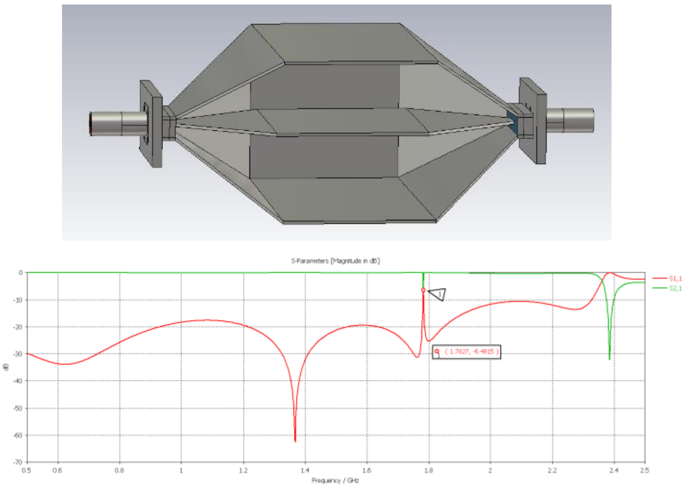

Figure 3-20 The closed TEM cell without modification and its S parameters response

In order to see the influence of the modification in the TEM cell, we designed a closed TEM cell as a reference for this study. Figure 3-21 displays the reference cell and its S parameter. It is noted the resonance at 1.78 GHz.

The first technique to dump the resonance of the higher modes is implemented by placing an absorber material on the top and bottom of the ground plane. The result of this case is shown in Figure 3-21 that prove a good efficiency in suppressing the resonance of the higher order mode.

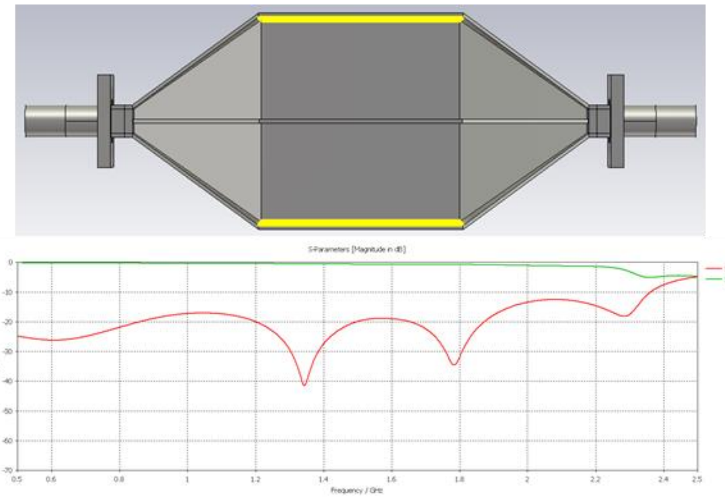

Figure 3-21 TEM cell with absorber material placed at the top and the bottom metal plane and its S parameter result

The second technique is to spilt the septum into two traces filled with an absorber material between them. The result is exhibited in Figure 3-22.

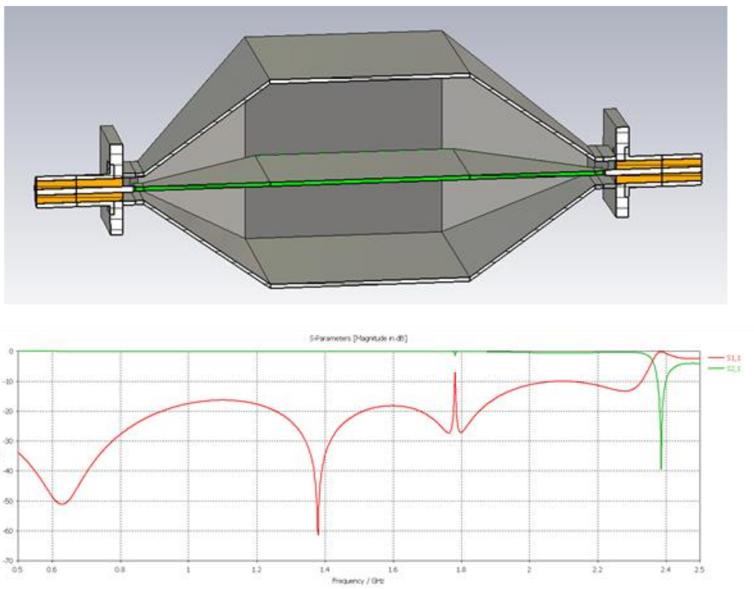

Figure 3-22 TEM cell with split septum filled with absorber material and its S parameters response

The results give lower efficiency compared to the first case. The suppression of the resonances for the higher order modes is a separate research topic that requires a deep study of the resonance phenomenon to develop a new technique that expands the bandwidth of the TEM cell.

3.6 MATERIAL CHARACTERIZATION USING CLOSED TEM CELL

In this work, the use of the closed TEM cell for material characterization is attempted for the first time. A novel design for closed TEM cell is proposed, this design allows the implementation of the different material characterization techniques. In addition to the MUT insertion easiness, this design provides a relative big test space comparing to the regular transmission lines. The bigger test space property could be an advantage in several characterization applications such as GPR. Knowing the electromagnetic properties of the scanned filed is a key factor in GPR detection efficiency. In some cases, the ground is not a homogeneous medium and it might contain a large or small clutters that should take their effective electromagnetic influence into consideration. Thus, with the proposed characterization test fixture it is possible to extract the effective electrical properties for buried objects. The landmine characterization is one of the interesting applications which will be discussed in this report.

3.6.1 Electromagnetic characterization simulation of homogeneous material

In chapter 2, the electromagnetic characterization techniques were reported in details. In addition a simulation and measurement validation was done with the use of a regular transmission line. Here we are presenting the use of a new test fixture for electromagnetic material characterization.

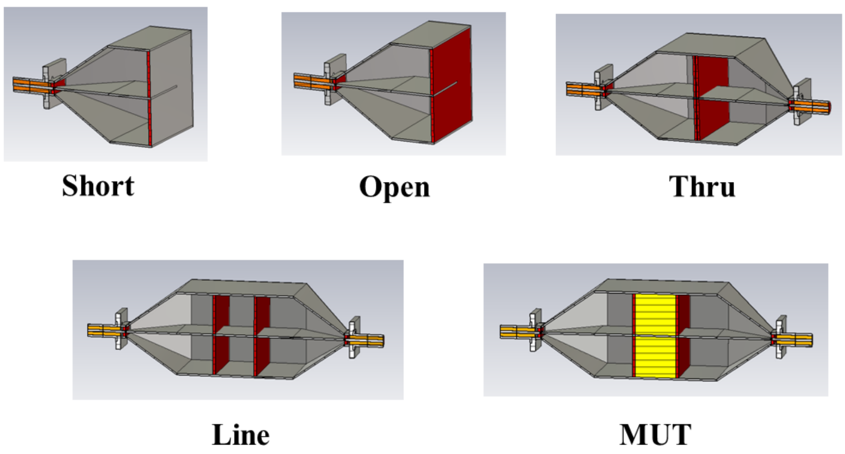

Figure 3-23 The cross-section side view of the closed TEM cell with different measurement configurations

Figure 3-23 exhibits the cross-section side view of the proposed closed TEM cell with different measurement configurations required for performing the different characterization techniques. The red color represents the PLA plastic holder where the yellow color denoted the MUT area. Six different characterization techniques were implemented numerically in order to characterize the lossy FR-4 material.

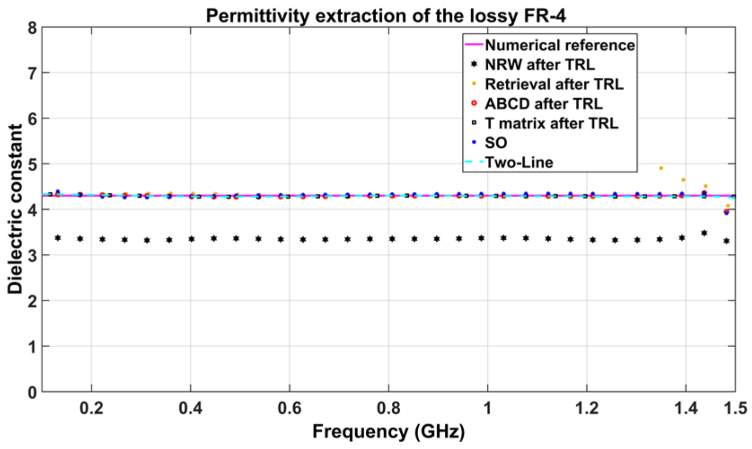

Figure 3-24 Comparison of the extracted simulated permittivity of lossy FR-4 material using different conversion methods

The extracted permittivity of the lossy FR-4 is plotted in Figure 3-24 while the extracted dielectric loss tangent of the lossy FR-4 is shown in Figure 3-25. We can notice from the results that the self-calibration methods in addition to the *T* matrix and *ABCD* matrix conversion methods prove a good correspondence between the extracted and the numerical reference curves. On the other hand, the *NRW* and the *Retrieval* conversion methods show fewer accuracy in the electromagnetic material properties extraction due to reasons explained in chapter 2.

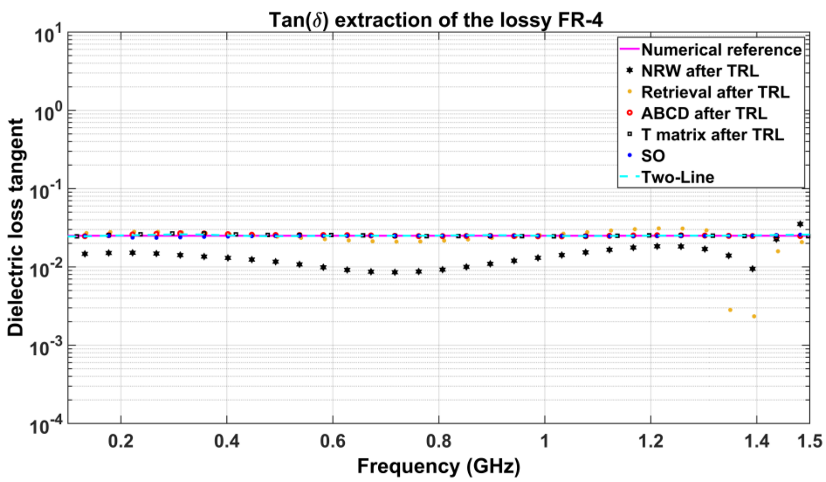

Figure 3-25 Comparison of the extracted simulated dielectric loss of lossy FR-4 material using different conversion methods

3.6.2 TEM cell dimension influence on simulation extraction of homogeneous material properties

In order to evaluate the TEM cell size impact on material properties extraction validity, a numerical parametric study was done. Figure 3-26 presents the parameterized cross-section view of the TEM cell middle part. Where ε is the permittivity of the homogeneous MUT.

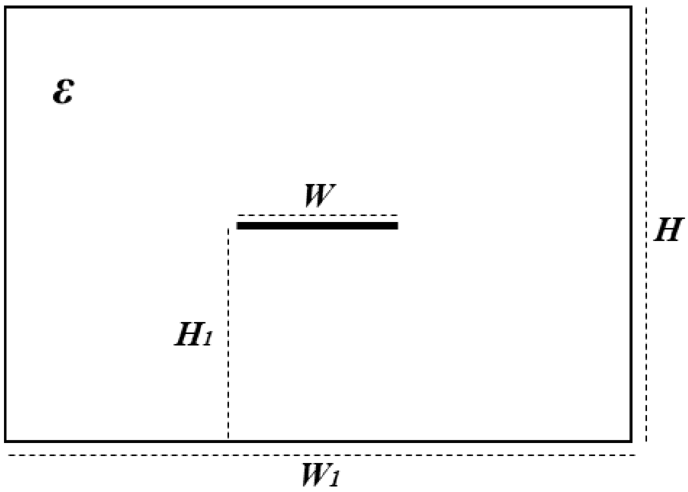

Figure 3-26 Parameterized cross-section view of the closed TEM cell

The parameters of the uniform section of the closed TEM cell is given in Table 3-2

Table 3-2 Parameters of the simulated TEM cell

Parameters	ε	W	W_1	H	H_1
Value	3	50 mm	[*60,...,190*] mm	162 mm	80mm

The numerical parametric study is started by placing a MUT in the closed TEM cell that has a permittivity of 3. Later, we simulate the closed TEM cell with the tuning of its width W_1. After that from the simulated S parameters, we extracted the permittivity using Two-line characterization method. The extracted permittivity versus W_1 at 600 MHz is displayed in Figure 3-27. The result proves that the extracted permittivity is impervious to the TEM cell size modification for the case of homogeneous material.

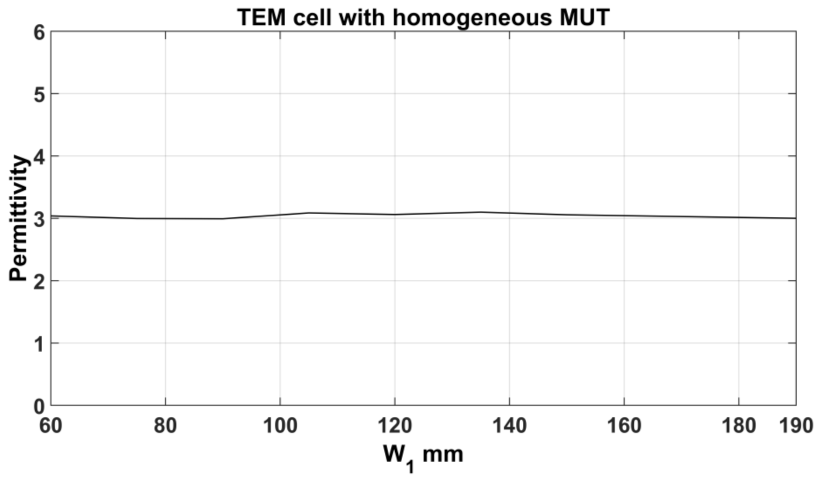

Figure 3-27 Permittivity extraction of homogeneous MUT placed in closed TEM cell with the changing of its global width W_1

3.6.3 Effective permittivity extraction simulation of composite material

In some applications, the MUT is not homogeneous and consists of composite materials, where each material has its own permittivity. Indeed, The electromagnetic characterization of composite material is not straightforward and related to several factors such as frequency, MUT size, material composition configuration, and measurement device. The extraction of the electrical properties of each component of the inhomogeneous material is complicated, time consuming, and is not practical. Instead of that, we can extract the effective electrical properties of this mixture that represented the global effective interaction between the EM field and this composition. Thus, studying the effective permittivity of a target placed in a specific medium could enhance the detection of this target using GPR or other sensor technology.

In this work, we propose also the use of the closed TEM cell for effective permittivity extraction of a target with their surrounding environment. The parametrized cross-section view of the closed TEM cell is exhibited in Figure 3-28. The yellow color represents the target that has a cylindrical shape with ε_1 as permittivity. While the remaining area in white color represents the environment with ε_2 as permittivity.

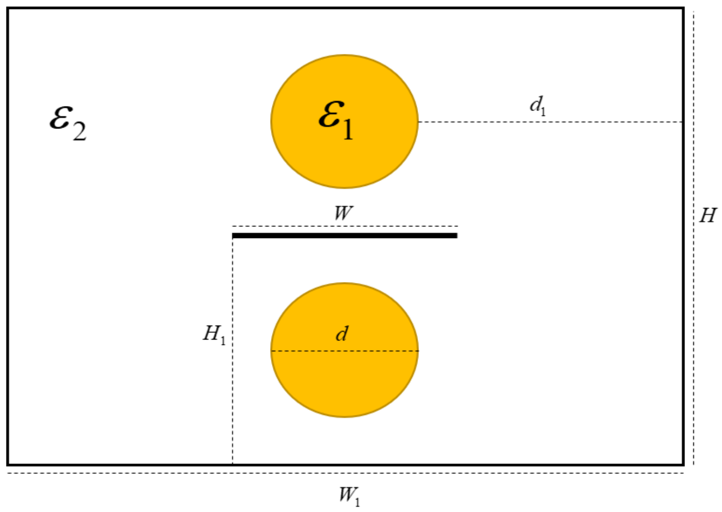

Figure 3-28 Parametrized dimensions of the cross-section view of the TEM cell

In order to evaluate the extracted effective permittivity variation with respect to the TEM cell dimension, a numerical study was implemented by considering the effects of three parameters ε_1, ε_2 and d_1.

Table 3-3 Parameters of the simulated closed TEM cell

Parameters	ε_1	ε_2	d (mm)	d_1 (mm)	H (mm)	H_1 (mm)	W (mm)	W_1 (mm)
Value	2.5	25	56	$[2,...,67]$	162	80	50	$(2d_1+d)$

We start the simulation study by using a closed TEM cell that has the parameters presented in Table 3-3. All the parameters are fixed except d_1. In this case, ε_1 is 2.5 and ε_2 is 25 and d_1 is tuned between 2 and 67 mm. From the simulated S parameters, we extracted the effective permittivity versus d_1 using Two-line conversion technique. The results are displayed in Figure 3-29. It is noted from the result that when d_1 increases the effective permittivity decreases. This behavior is due to the closer distance between the septum and the sidewall comparing to the distance between the septum and upper and the lower ground plane of the proposed TEM cell. The electric field is higher between two closer metal plates.

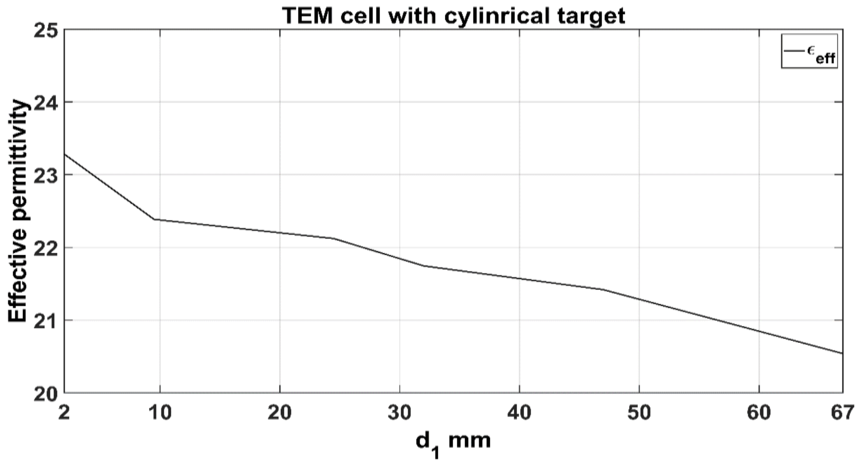

Figure 3-29 Extracted effective permittivity versus d1, where permittivity of cylinder is 2.5 and of MUT is 25

So, the extracted effective permittivity is more sensitive to the septum sidewall area. For this reason, when we have MUT with 25 of permittivity and target with 2.5 of permittivity the effective permittivity is going down while the distance d_1 increased.

Table 3-4 Parameters of the simulated closed TEM cell

Parameters	ε_1	ε_2	d (mm)	d_1 (mm)	H (mm)	H_1 (mm)	W (mm)	W_1 (mm)
Value	25	2.5	56	$[2,...,67]$	162	80	50	$(2d_1+d)$

Now we switch the permittivity values between ε_1, and ε_2. Then we did the same previous study. The extracted effective permittivity versus d_1 is shown in Figure 3-30. Here an increase in the effective permittivity is observed when d_1 increases. This response demonstrates that the extraction permittivity is more sensitive to the area that has a higher electric field. Furthermore, when d_1 increases the electric field in this area decreases, so the target permittivity effect becomes more relevant in the effective permittivity of the mixture. The same explanation used in the earlier case can work here and vice-versa.

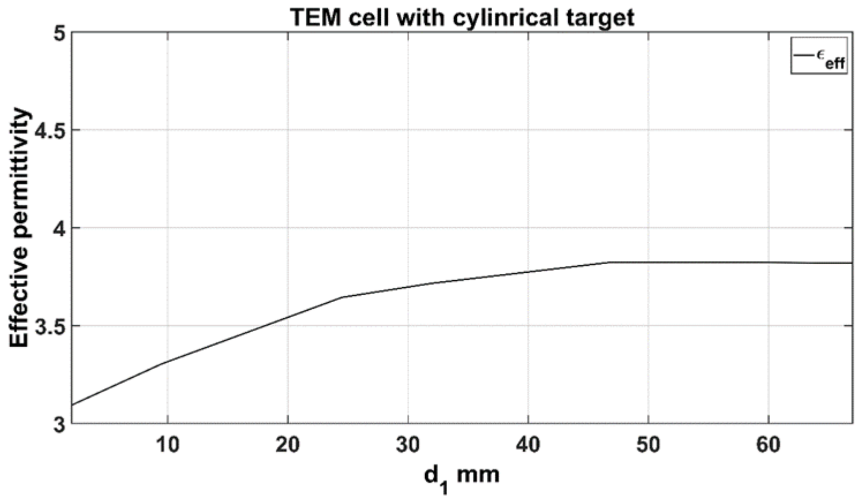

Figure 3-30 Extracted effective permittivity versus d_1, where permittivity of cylinder is 25 and of MUT is 2.5

In the following simulation study, we fixed the parameters of the closed TEM cell and we tune ε_1 as presented in Table 3-5.

Table 3-5 Parameters of the simulated closed TEM cell

Parameters	ε_1	ε_2	d (mm)	d_1 (mm)	H (mm)	H_1 (mm)	W (mm)	W_1 (mm)
Value	[2, …, 5]	25	56	32	162	80	50	$(2d_1 + d)$

The extracted effective permittivity that plotted in Figure 3-31 is situated near to the permittivity of 21. That is related to the side area which has a permittivity of 25 and it is intuitive to have these values as we explained before. In addition, it is noted the increase in the effective permittivity while the increasing of ε_1. This is proving that the effective permittivity should be a value between ε_1 and ε_2, and should not exceed that range of permittivity.

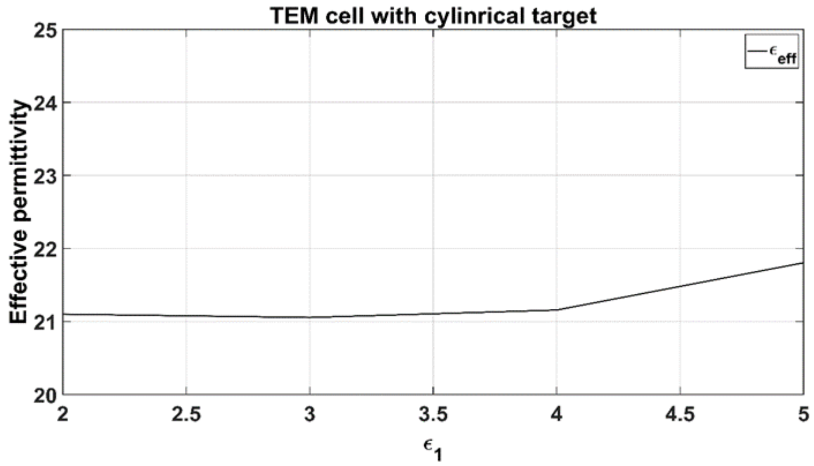

Figure 3-31 Extracted effective permittivity versus ε_1, where permittivity of cylinder 2-5 and of MUT is 25

The last case is simulating the change effect of ε_2 on the effective permittivity when all the remaining parameters are fixed.

Table 3-6 Parameters of the simulated closed TEM cell

Parameters	ε_1	ε_2	d (mm)	d_1 (mm)	H (mm)	H_1 (mm)	W (mm)	W_1 (mm)
Value	2.5	[20,…, 50]	56	32	162	80	50	$(2d_1 + d)$

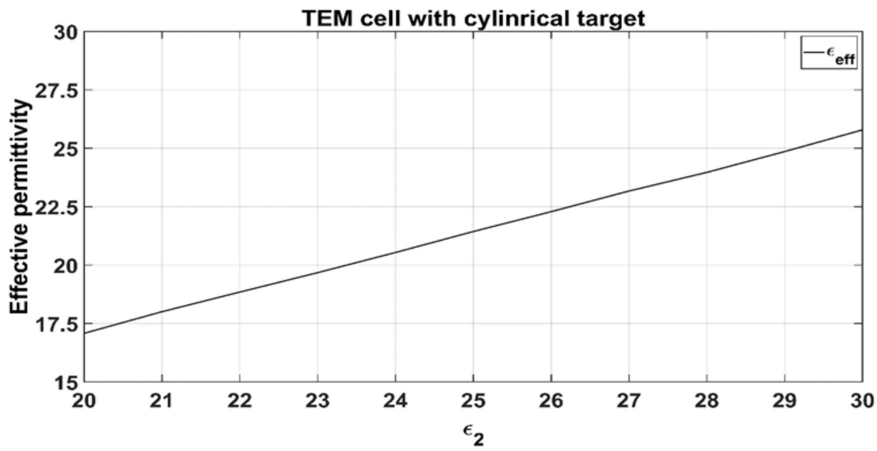

Figure 3-32 Extracted effective permittivity versus ε_2, where permittivity of cylinder is 2.5 and of MUT is 20-30

Figure 3-32 plots the response of the effective permittivity versus ε_2. The cylindrical target has a permittivity of 2.5 and the MUT permittivity varied from 20 till 30. As expected the effective permittivity increases with the increasing of ε_2.

At the end of this study, we can conclude that the extracted effective permittivity of a composition of material using closed TEM cell is equal the MUT permittivity plus or minus value related to the permittivity of the target and its size.

3.6.4 Material characterization measurement of homogeneous material

After the simulation validation study that accomplished in section 3.6.1 for the electromagnetic material characterization using a closed TEM cell, we will move to the material characterization measurement application using the closed TEM cell that proposed in section 3.4.2. The different parts of the closed TEM cell are shown in Figure 2.33, these components are sufficient to implement the diverse measurement configurations that displayed in Figure 3-23.

Figure 3-33 The closed TEM cell that used for material characterization application

Since we are interested in the characterization of targets buried in the soil, we use first the closed TEM cell to measure the permittivity of homogeneous samples of sand and soil. The Measured permittivity results for the sand and soil are exhibited respectively in Figure 3-34 and Figure 3-35.

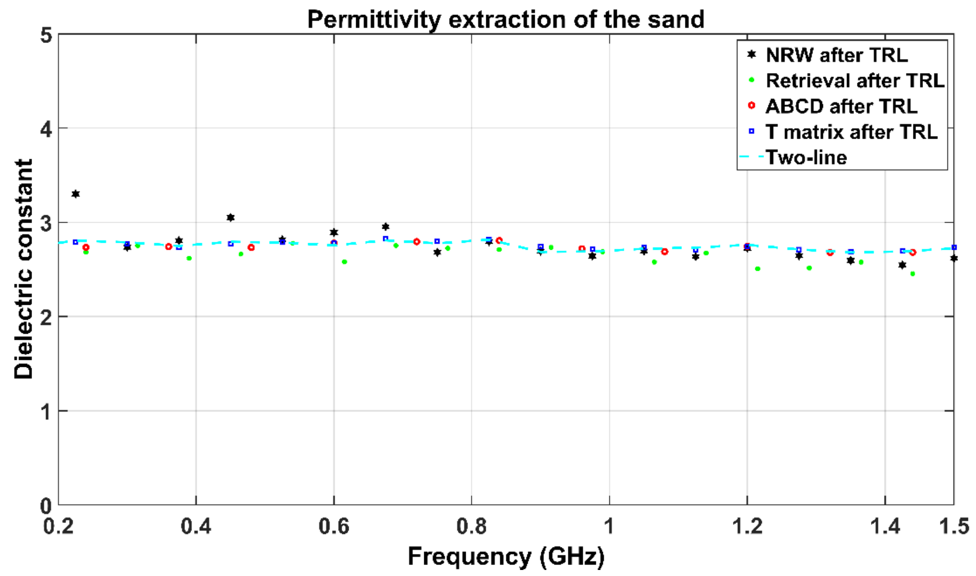

Figure 3-34 Permittivity extraction of the sand using the closed TEM cell and comparing different conversion methods

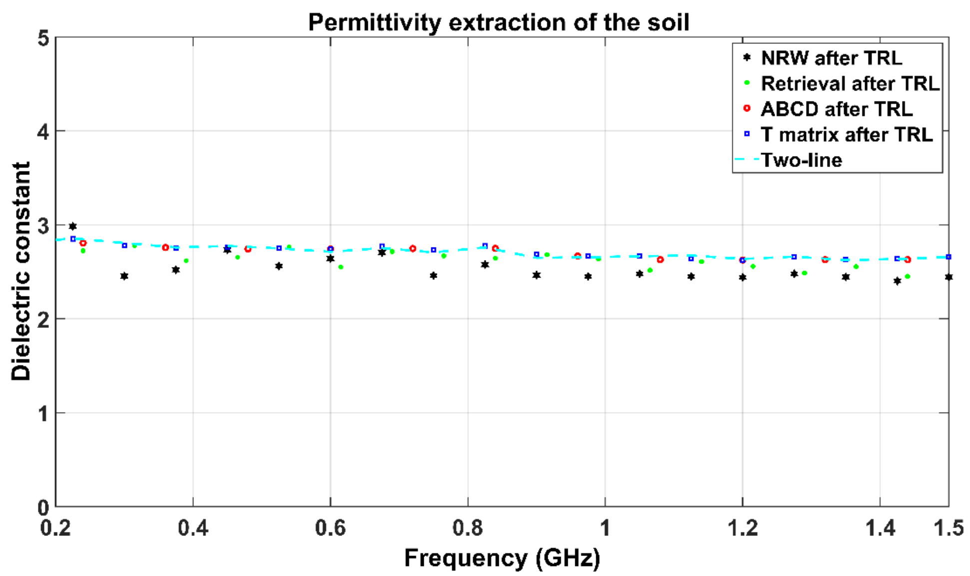

Figure 3-35 Permittivity extraction of the sand using the closed TEM cell and comparing different conversion methods

It is noticed from the results that the extracted permittivity situated in the commonly known permittivity range of the soil and sand. Based on the earlier simulation studies, the Two-line conversion method is considered as a method among the most accurate conversion methods. The extracted permittivity results using Two-line method for sand and soil are presented in a separate plot. The comparison between the permittivity of the sand and the soil is shown in Figure 3-36.

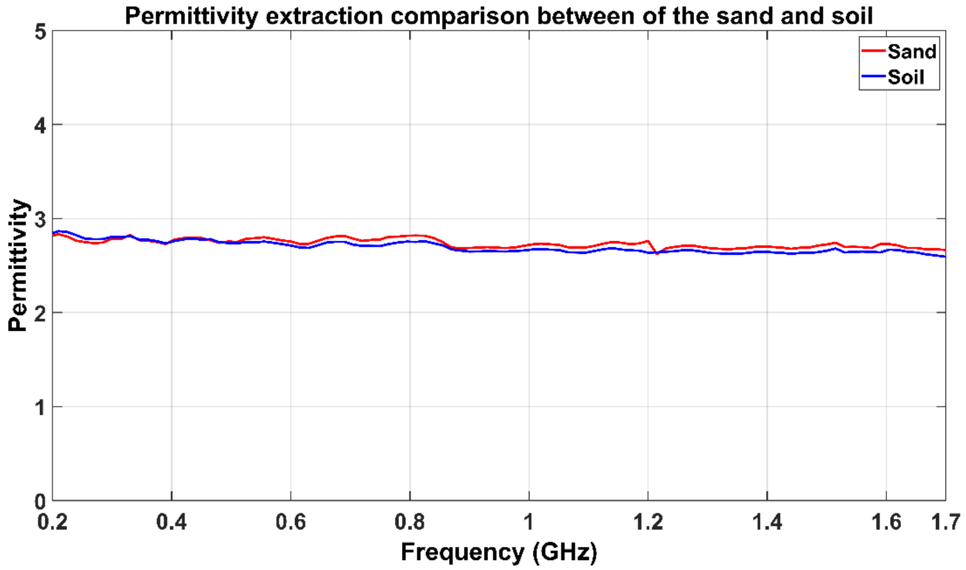

Figure 3-36 Permittivity comparison between the sand and soil

The comparison of the dielectric loss tangent are presented in Figure 3-37

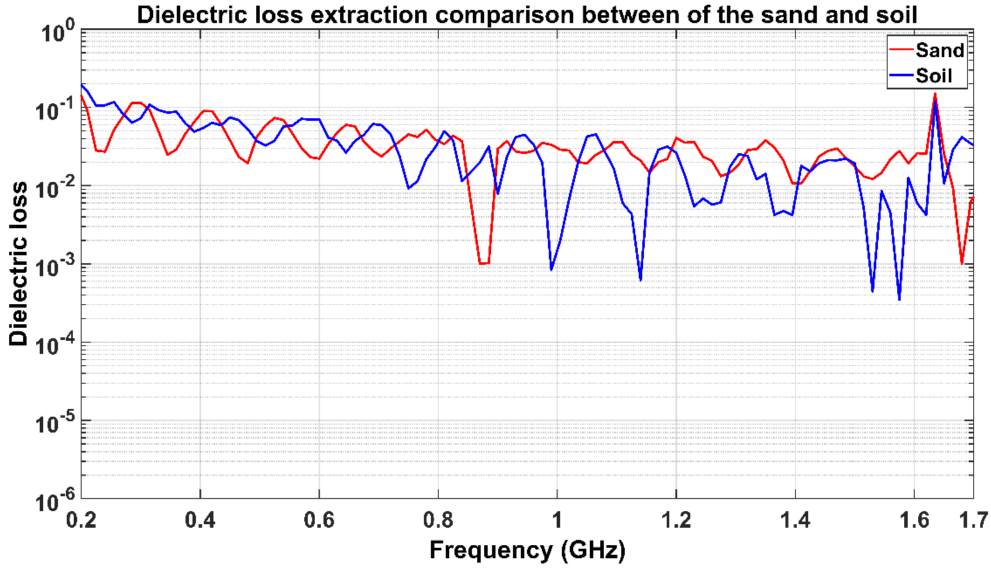

Figure 3-37 Dielectric loss comparison between the sand and soil

3.7 LANDMINES CHARACTERIZATION USING CLOSED TEM CELL

In earlier, the landmines problem and its impact on human life were discussed. Now in order to expand the scientific knowledge in a research topic that potentially leads to enhance the detection of the landmines, the effective permittivity of two kinds of antipersonnel landmines is determined. The idea is to use the closed TEM cell as a measurement device for MUT that consists of soil and landmine. Basing on subsection 3.6.3 we can select a suitable dimension of closed TEM cell to use it in the simulation. The dimension of the used TEM cell depends on landmine and soil sample size. In our case, we selected the parameters presented in Table 3-7 since we already studied the TEM cell size variation impact on effective permittivity.

Table 3-7 Parameters of the used closed TEM

Parameters	ε_1	ε_2	H (mm)	H_1 (mm)	W (mm)	W_1 (mm)
Value	Landmine	Dry soil ($\simeq 2.5$) or wet soil ($\simeq 20$)	162	80	50	120

Then one of the conversion methods used in subsection 3.6.1 can be employed to get the effective permittivity of the landmine inserted in a soil sample. The simulation configuration of closed TEM cell in case of measuring the M14 with soil case is displayed in Figure 3-38.

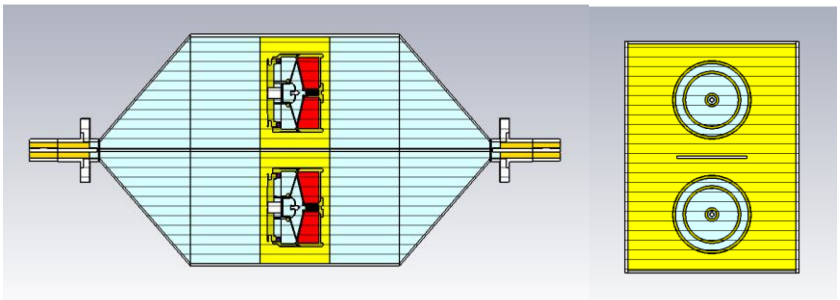

Figure 3-38 Side and cross views of the TEM cell fitted with soil and M14 landmine

Two M14 landmines were placed above and below the septum of the TEM cell with the aim of conserving the symmetricity in an electrical and physical point of view. We started the study by simulating two cases, first dry soil alone, and seconde dry soil with M14. The MUT sample length was 5 cm in this simulation the comparison of the two cases is shown in Figure 3-39. A slight difference is observed in the extracted effective permittivity for the two cases. The permittivity difference is around 0.1. In addition, a relatively small resonance occurs at around 1.3 GHz and this is due to the presence of the M14 landmine.

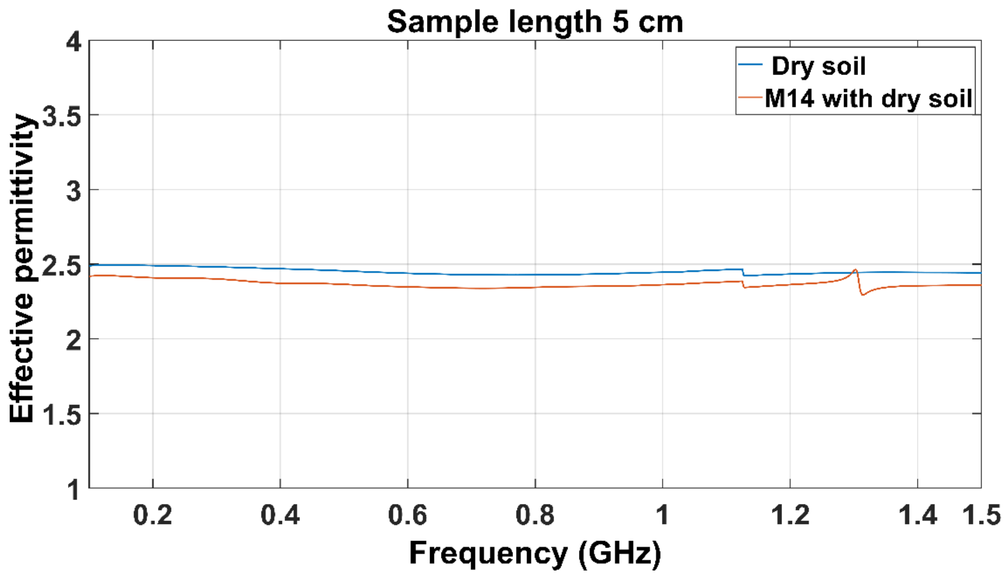

Figure 3-39 Permittivity comparison between the dry soil and M14 with dry soil

Another scenario is studied in this work is for the case of wet soil. It is known that the permittivity of the water is high and have a value around 80. So when the humidity of the soil increases its permittivity should also increase due to the water content growing in the medium. We used wet soil which has a permittivity of about 20. The effective permittivity comparison of the wet soil with the presence or not of the M14 is exhibited in Figure 3-40. A relatively high difference between the two effective permittivities is noticed in the result of value around 3.

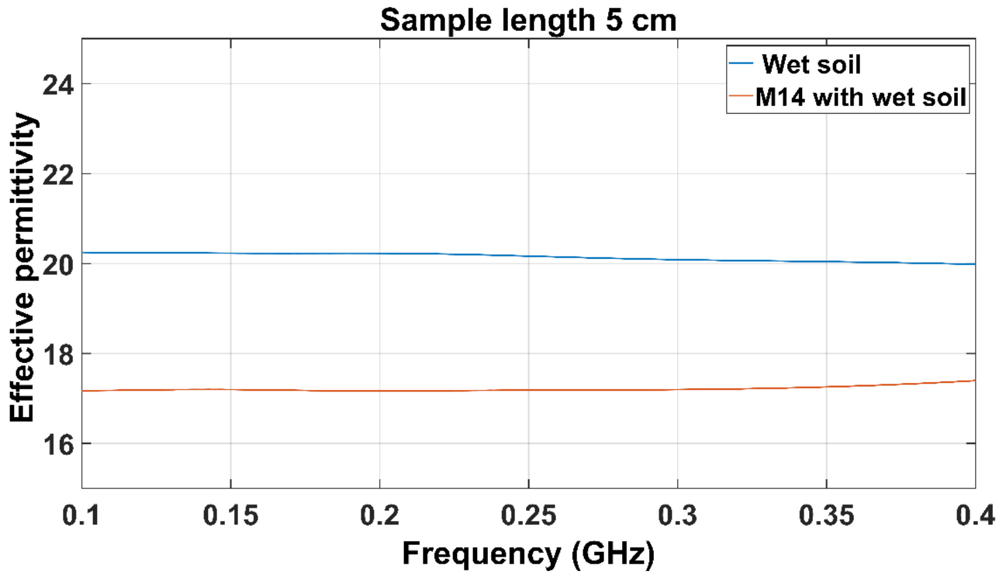

Figure 3-40 Permittivity comparison between the wet soil and M14 with wet soil

Now, the same simulation scenarios are performed again with the use of M59 landmine.

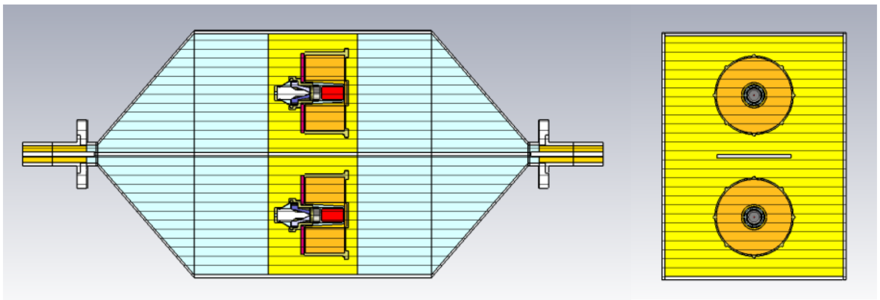

Figure 3-41 Side and cross views of the TEM cell fitted with soil and M59 landmine

The M59 has a different size comparing to M14. Thus, a different MUT sample length of 6 cm is used for covering all the mine body with soil. The simulation configuration of the M59 inside the closed cell is displayed in Figure 3-41. The effective permittivities of the dry soil with and without M59 are plotted in Figure 3-41. The permittivity difference is almost zero in this case. A small resonance occurs at around 1.23 GHz due to the presence of the landmine.

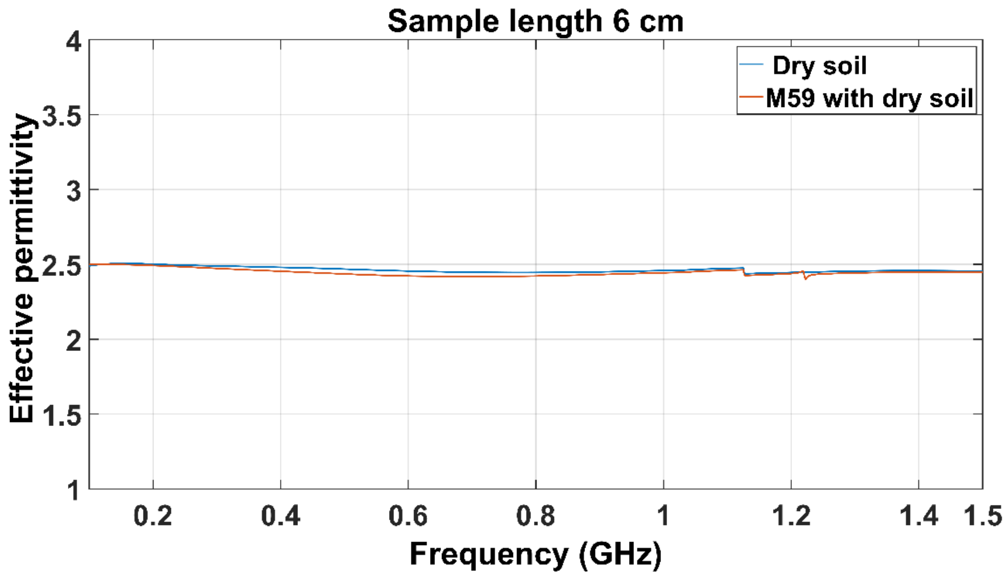

Figure 3-42 Permittivity comparison between the dry soil and M59 with dry soil

The last case is the simulation of wet soil with the presence or not of M59 landmine. This case gives a permittivity difference of about 2 as shown in Figure 3-43. Interesting results were obtained in this study, we saw that the effective permittivity of the dry soil is very near to effective permittivity of the dry soil with M14 and almost the same with M59. In the other side, the effective permittivity difference was clearly found with the wet soil case. So taking into consideration this observation in addition to the small resonance occurred in dry soil case with the landmines, a new enhancement could be applied to the detection process of the landmine.

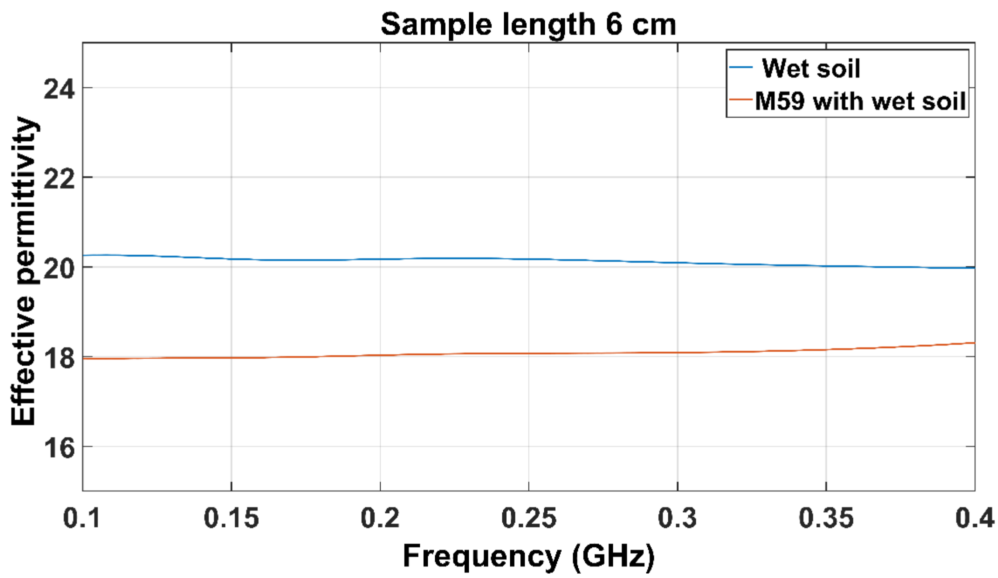

Figure 3-43 Permittivity comparison between the wet soil and M59 with wet soil

3.8 CONCLUSION

In this chapter, a full theoretical review of the TEM cell is reported. The different types of TEM cell including closed and open are numerically and experimentally implemented. In addition, the bandwidth limitation due to the presence of the higher order mode resonances is discussed and several solutions for expanding the operational bandwidth are proposed. Furthermore, the use of the closed TEM cell for material characterization application is first introduced in this work. Where a novel fabricated model of closed TEM cell is exhibited for electromagnetic material properties measurement. The TEM cell's dimension impact on the extracted effective permittivity is studied. Two kinds of antipersonnel landmines with their surrounding environment were numerically characterized in order to provide the GPR system with helpful data for detection enhancement.

3.9 REFERENCES

[1] Crawford, Myron L. "Generation of standard EM fields using TEM transmission cells." *IEEE transactions on Electromagnetic Compatibility* 4 (1974): 189-195.

[2] Satav, Sandeep M., and Vivek Agarwal. "Do-it-yourself fabrication of an open TEM cell for EMC pre-compliance." *IEEE EMC Society Newsletter* 218 (2008): 66-71.

[3] Clemens, Icheln. "The construction and application of a GTEM cell. Diplomityö. Verkkodokumentti." (2013).

[4] Cai, X-D. "Analysis of asymmetric TEM cell and its optimum design of electric field distribution." In *IEE Proceedings H-Microwaves, Antennas and Propagation*, vol. 136, no. 3, pp. 191-194. IET, 1989.

[5] Arezoomand, Masoud, Mohsen Kalantari Meybodi, and Narges Noori. "Design of a TEM cell using both multi-step and piecewise linear tapering." In *2016 8th International Symposium on Telecommunications (IST)*, pp. 571-574. IEEE, 2016.

[6] Boriraksantikul, Nattaphong. "A TEM cell design to study electromagnetic radiation exposure from cellular phones." PhD diss., University of Missouri--Columbia, 2008.

[7] Kim, Y. D., Y. V. Prokopenko, and Y. M. Poplavko. "TEM cell electromagnetic field simulation." In *1999 9th International Crimean Microwave Conference'Microwave and Telecommunication Technology'. Conference Proceedings (IEEE Cat. No. 99EX363)*, pp. 40-43. IEEE, 1999.

[8] Song, Chunjiang, and Xiaoyao Feng. "A new design and implementation of expanding testing space of a transverse electromagnetic cell." In *2016 IEEE International Conference on Microwave and Millimeter Wave Technology (ICMMT)*, vol. 2, pp. 967-969. IEEE, 2016.

[9] Fei, Dai, Wang Mi, and Su Donglin. "A design of new twin TEM cells." In *2005 IEEE International Symposium on Microwave, Antenna, Propagation and EMC Technologies for Wireless Communications*, vol. 1, pp. 10-13. IEEE, 2005.

[10] Cai, X-D., and G. I. Costache. "Theoretical modeling of longitudinal variations of electric field and line impedance in TEM cells." *IEEE transactions on electromagnetic compatibility* 35, no. 3 (1993): 398-401.

[11] Tippet, John C., and D. C. Change. "Radiation characteristics of dipole sources located inside a rectangular, coaxial transmission line." *NASA STI/Recon Technical Report N* 76 (1976).

[12] Das, Sisir K., and B. K. Sinha. "Numerical solution of higher order mode cut-off frequencies in symmetric TEM cells using finite element method (EMI measurement applications)." *IEEE Transactions on Electromagnetic Compatibility* 32, no. 4 (1990): 264-268.

[13] Hill, Douglas A. "Bandwidth limitations of TEM cells due to resonances." *Journal of Microwave Power* 18, no. 2 (1983): 181-195.

[14] Ipc-2141A, "Design Guide for High-Speed Controlled Impedance Circuit Boards," *Ipc*, no. April 1996. pp. 16–19, 2004.

[15] Deng, Shaowei, David Pommerenke, Todd Hubing, and Dongshik Shin. "An experimental investigation of higher order mode suppression in TEM cells." *IEEE transactions on Electromagnetic Compatibility* 50, no. 2 (2008): 416-419.

Chapter 4: Permittivity Extraction Using GPR

Contents

4.1 INTRODUCTION

The dielectric constant of the soil is varied from test site to other. These variations in electrical properties of the soil directly affect the GPR response of a buried target since the reflection coefficient between the soil and target is related to their permittivity contrast. That is lead to obtaining different GPR responses for the same target at the same depth in tow different fields [1].

So knowing the permittivity of the working minefield is an essential issue for enhancing the GPR detection and localization process. In Chapter 3 we proposed a TEM cell technique for extracting accurately the permittivity of homogenous or mixed soil (or any complicated mixture).

In several applications, the permittivity extraction using a non-contacting method has great value, especially in the case of working in a real minefield that any pressure on the ground surface is prohibited.

This chapter discusses the use of the GPR system in permittivity extraction of the ground. The extraction theory is reported. In addition, a numerical study was performed in order to find the optimal configuration of a GPR system in order to raise the accuracy of the extracted permittivity.

4.2 PERMITTIVITY EXTRACTION THEORY USING GPR

The GPR system is introduced in earlier. **Error! Reference source not found.** hows the configuration of a general GPR system. Two antennas are used in bistatic configuration facing the soil surface to measure the reflected signal.

The frequency-domain method is chosen in this study to estimate the permittivity of the soil since it is less complex than the time-domain method. The S parameters represent the frequency domain data required to extract the permittivity.

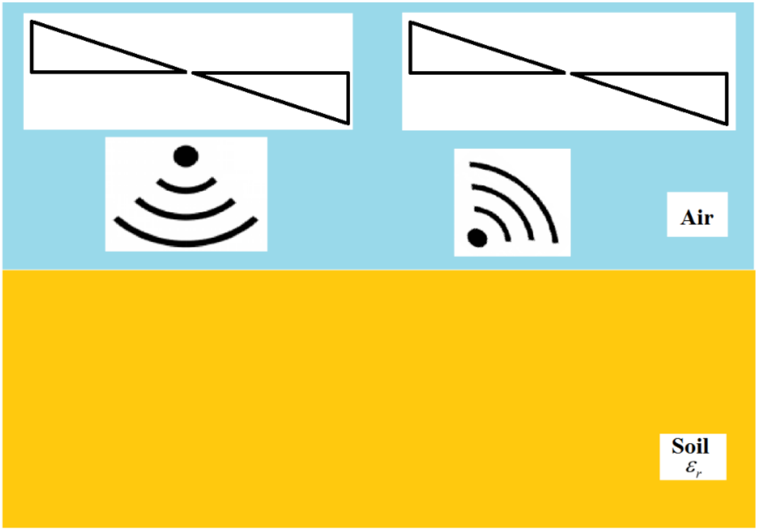

Figure 4-1 General configuration of GPR

The reflection coefficient of the reflected electric field at the interface between the two mediums can be expressed as follow [2]:

$$\Gamma = \frac{\eta_2 - \eta_1}{\eta_2 + \eta_1} \tag{4.1}$$

Where η is the intrinsic impedance of the medium

$$\eta = \eta_0 \sqrt{\frac{\mu_r}{\varepsilon_r}} \tag{4.2}$$

Here $\eta_0 = 377\Omega$ denotes the intrinsic impedance of the free space. Since we are considering the medium is nonmagnetic, the relative permeability is $\mu_r = 1$. Typically in the GPR system, the first medium is the air as exhibited in Figure 4-1, So the relative permittivity of the first medium is $\varepsilon_r = 1$. Then by substitute Eq. (4.2) in Eq. (4.1), the reflection coefficient becomes:

$$\Gamma = \frac{1-\sqrt{\varepsilon_r}}{1+\sqrt{\varepsilon_r}} \tag{4.3}$$

The permittivity of the MUT is deduced from the inversion of the above equation and will result in:

$$\varepsilon_r = \left(\frac{1+\Gamma}{1-\Gamma}\right)^2 \tag{4.4}$$

Indeed, the reflected signal that we sense at the received antenna in the GPR system consists of the direct coupling between the antennas, the multi-paths of transmission and reflection in addition to the reflection that comes directly from the soil (or any MUT). Furthermore, several parameters can have an influence on the overall GPR system such as antenna directivity and its radiation pattern.

Treating all these responses and the effect of the parameters makes the problem more complex and time-consuming. Therefore, a calibration procedure should be performed to cancel out the noise involved in the received response.

The idea of the calibration is to measure the GPR response for a reference material that its reflection coefficient is known. The metal could be a good reference since we know its interaction behavior with the EM wave. The good conductor plate will act as a total reflector of the EM field but with a 180^0 of phase difference. Using this fact, we can investigate the calibration process in both time and frequency domain.

In the frequency domain analysis, we need the S parameters of the GPR system. Where S_{11} and S_{22} denote return losses of the first and the second antennas respectively, while S_{21} denotes transmission from the first to the second antenna. These parameters can be measured using a VNA.

In the fact that the measured S_{21} of the GPR system includes the reflection coefficient of the air-MUT interface in addition to all noise parameters that we already mentioned, we can obtain the calibrated reflection coefficient of the air-soil interface by dividing the transmission of the air-soil interface by the transmission air-metal interface [3][4].

$$\Gamma_{calibrated} = \frac{S_{21material}}{S_{21metal}} \tag{4.5}$$

Here, $S_{21material}$ and $S_{21metal}$ represent the transmission from the first to the second antenna when the GPR is facing the soil (or any MUT) and the metal plate respectively.

$$\Gamma_{calibrated} = \frac{\Gamma_{material}}{\Gamma_{metal}} = \frac{\Gamma_{material}}{-1} \tag{4.6}$$

The division in Eq. (4.5) will give the division of the reflection coefficient of the material by the reflection coefficient of the metal.

Later on, the permittivity of the soil can be extracted using the calculated $\Gamma_{calibrated}$ in Eq. (4.4).

Now, for the time domain analysis, the same measurement procedure should be applied but with the reading of the amplitude of the reflected signal versus time. The permittivity can be calculated using the expression below[5][6][7][1]:

$$\varepsilon_r = \left(\frac{1 + A_{material} / A_{metal}}{1 - A_{material} / A_{metal}} \right)^2 \tag{4.7}$$

Where $A_{material}$ is the surface reflection amplitude of the soil, and A_{metal} is the metal plate reflection amplitude.

4.3 GPR SYSTEM DESIGN AND SIMULATION

The simulated testbed model of the used GPR system is displayed in Figure 4-2. The system includes two antipodal Vivaldi antennas and the soil. As we reported earlier, the GPR performance related to many factors as for example antenna type, antenna operational bandwidth, the space between antennas, and the space between antennas and soil surface.

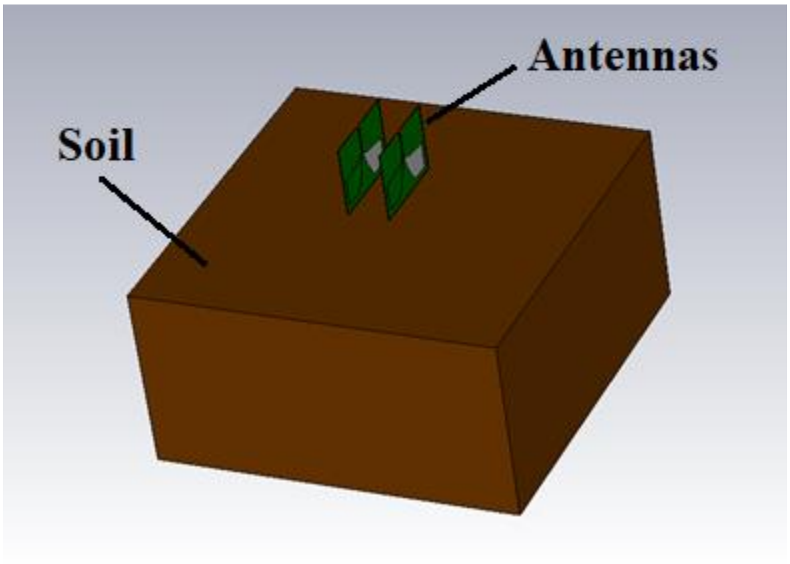

Figure 4-2 Simulated model of the GPR system

In this work, several factors were taken into consideration during the simulation study in order to find the optimal configuration for extracting the soil permittivity.

In this work we will use the frequency domain analysis, So the S_{21} is required to extract the permittivity as stated in the theoretical section. In the following, three different cases were simulated to clarify the transmission responses between the antennas.

The first case is the simulation comparison of two S_{21} responses for two scenarios when the two antennas are separated by a reflector or not. The reflector here can be any plate of metal, and its aim is to reduce the direct coupling between the antennas.

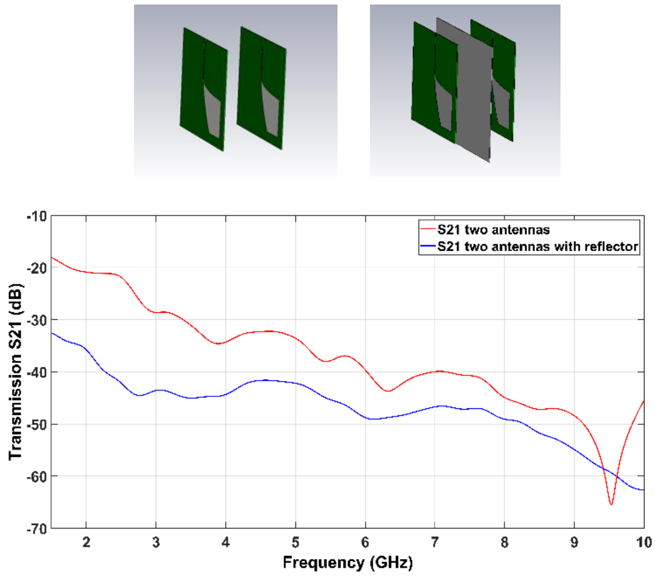

Figure 4-3 The transmission parameter S_{21} comparison between antennas with and without reflector

Figure 4-3 exhibits the S21 comparison between antennas with and without a reflector. It is clearly noticed the decreasing of the S21 in case of placing the reflector. This way of isolation could be an important factor for the GPR system performance.

In the second case, the comparison is made between the transmission parameters S_{21} when the antennas opposite the free space and a plate of metal. The results are displayed in Figure 4-4. The presented result is intuitive since we are expecting to receive more power when the metal plate is placed. This measurement is important in the permittivity extraction process because it is considered as the reference measurement needed for the calibration.

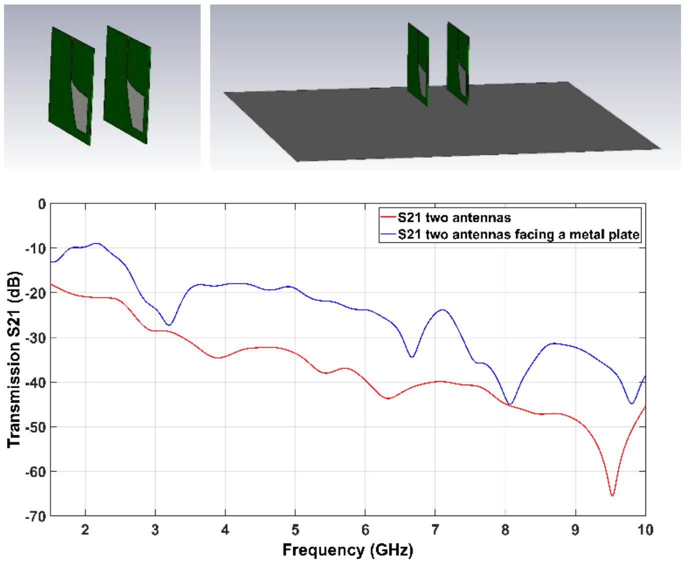

Figure 4-4 The transmission parameter S_{21} comparison between antennas fronting the metal plate or not

The last case is when the antennas fronting the soil. In Figure 4-5 the comparison of the transmission parameters S_{21} is plotted for two scenarios when the antennas in front of the soil or not.

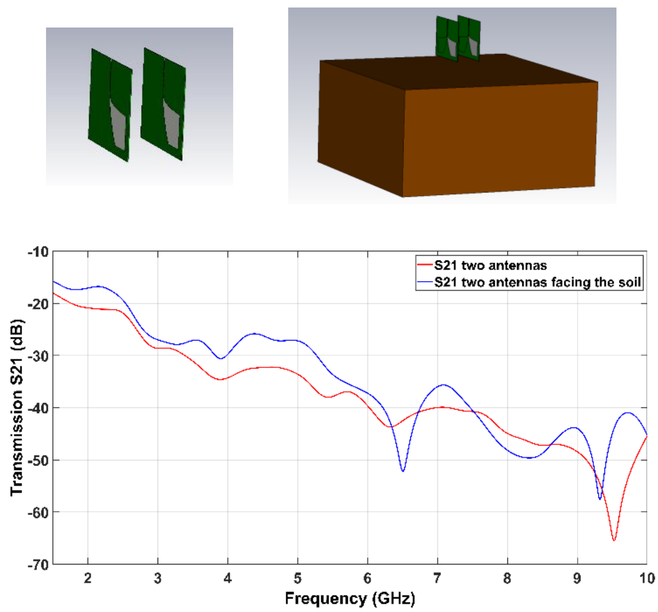

Figure 4-5 The transmission parameter S_{21} comparison between antennas facing the soil or not

Now, the transmission parameters S_{21} can be extracted from the EM software in order to use them in the permittivity extraction expression.

4.4 PERMITTIVITY EXTRACTION USING TWO ANTIPODAL VIVALDI ANTENNAS OPERATE WITHIN 1.5-10 GHZ RANGE

We start the permittivity extraction simulation study by using a GPR system consists of two antipodal Vivaldi antennas operate from 1.5 GHz to 10 GHz. The idea is to modify the different parameters of the system to find the optimal configuration for permittivity estimation. The design details of the used antenna are given in the next subsection.

4.4.1 Antipodal Vivaldi antenna

Vivaldi antennas are preferred in several applications, including GPR, due to their wideband properties, directional pattern, high gain, simple structure and easy fabrication [8][9]. An antipodal Vivaldi antenna is designed and simulated. The design model and its dimensions are given in Figure 4-6. The substrate of this antenna is the FR4 with a thickness of 1.6 mm.

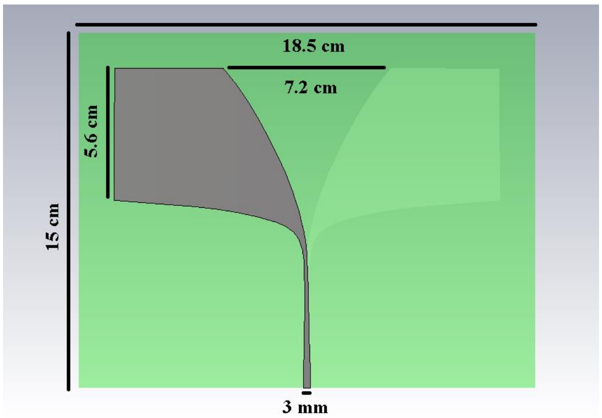

Figure 4-6 Dimensions of the first designed antipodal Vivaldi antenna

The reflection parameter S_{11} of the antenna is exhibited in Figure 4-7, where an operation is proven in the frequency range from 1.5 to 10 GHz. This is considered where S_{11} stays below -10 dB.

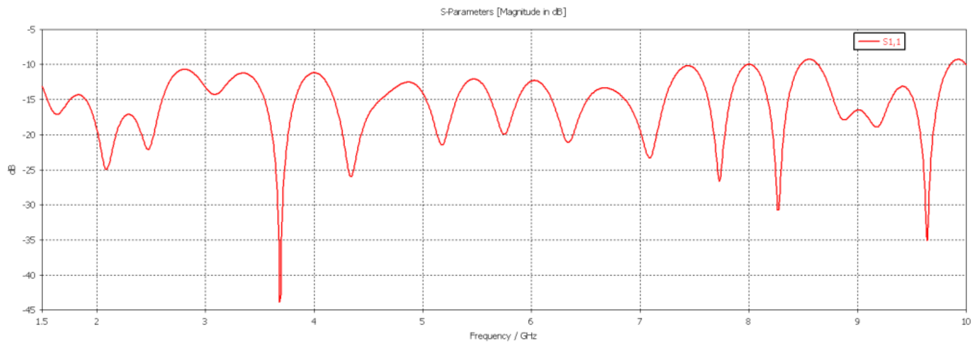

Figure 4-7 The simulated reflection coefficient result of the antenna

The radiation pattern of the presented antenna at 5 GHz is exposed in Figure 4-8.

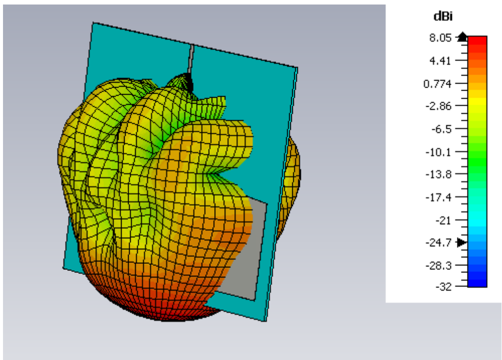

Figure 4-8 Farfield Radiation pattern at 5 GHz

4.4.2 Two antennas without reflector first configuration

The first configuration is to put the two antennas in a parallel manner to each other above the soil surface.

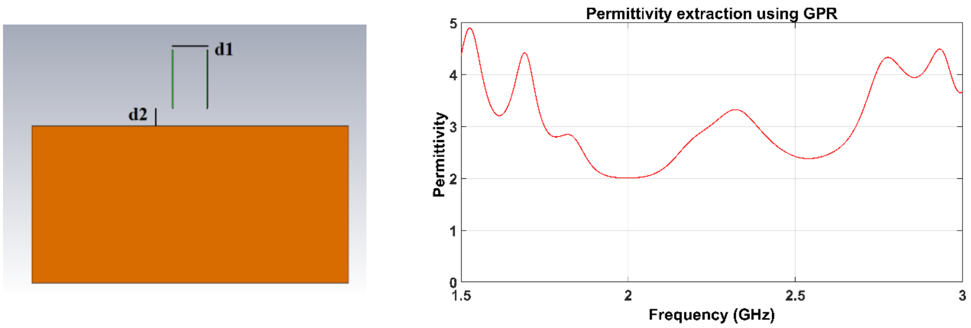

Figure 4-9 Extracted permittivity d1=88mm and d2=50mm

Two parameters were used here related to the system configuration, the separation distance between the antennas and the distance between the soil surface and antennas. They denoted respectively by d1 and d2 terms as shown in Figure 4-9. In this simulation case, d1=8.8 cm and d2=5 cm. The extracted permittivity is also plotted in Figure 4-9 over the 1.5-3 GHz bandwidth.

4.4.3 Two antennas with reflector first configuration bandwidth effect

We did again the same simulation case but with an added reflector between the two antennas. The aim of placing this reflector is to reduce the direct coupling between the antennas. Here d1 is 8.8 cm, d2 is 5 cm and the simulation is performed over the 1.5-3 GHz bandwidth. The extracted permittivity is shown in Figure 4-10.

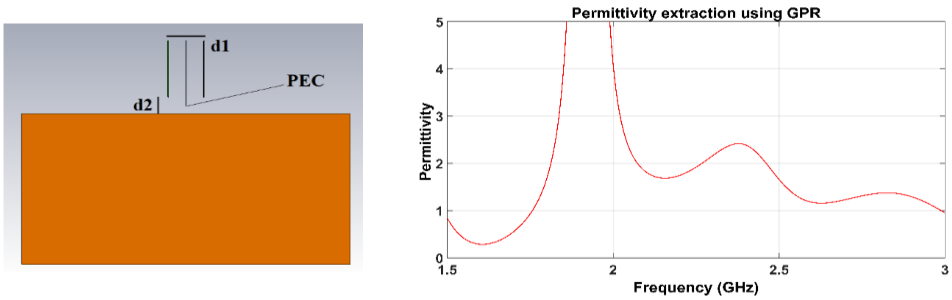

Figure 4-10 Extracted permittivity d1=88 mm d2=50 mm, over 1.5-3 GHz bandwidth

Later on, we run the same simulation case but over different bandwidth to see its influence on the extracted permittivity. The bandwidth in this simulation is 4-8 GHz. The extracted permittivity for this case is displayed in Figure 4-11

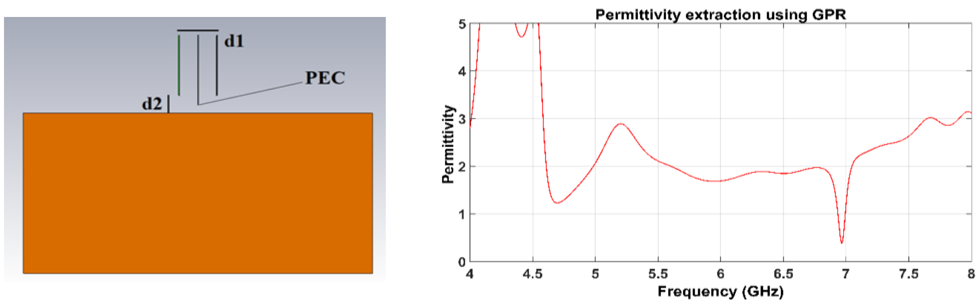

Figure 4-11 Extracted permittivity d1=88 mm d2=50 mm, over 4-8 GHz bandwidth

4.4.4 Two antennas with reflector first configuration and d1 variation effects

Now, the effect of the antennas separation distance is studied by the tuning of d1 parameter. Where d2 is fixed to 5 cm, d1 is taking the values of 100, 200, and 300 mm. The extracted permittivity over 1.5-3 GHz range is given in Figure 4-12 for different d1 values.

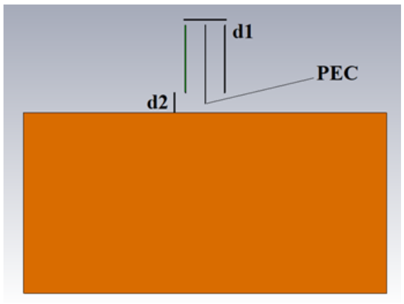

(a)

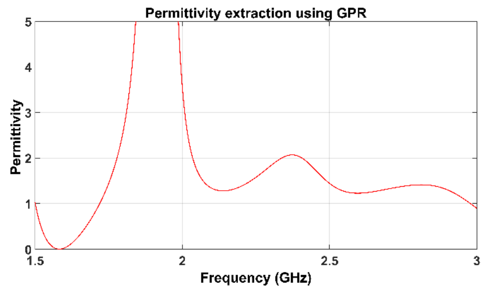

(b)

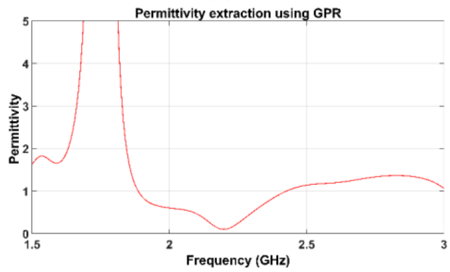

(c)

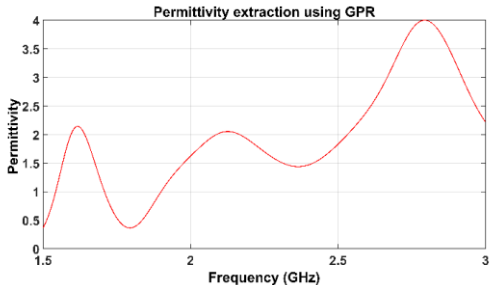

(d)

Figure 4-12 (a) GPR system with reflector, (b) extracted permittivity d1=100 mm, d2=50 mm, (c) extracted permittivity d1=200 mm d2=50 mm, (d) extracted permittivity d1=300 mm d2=50 mm

4.4.5 Two antennas with reflector first configuration and d2 variation effects

The permittivity is extracted in this case with the changing of the antennas soil distance value for showing its effect. d1 is fixed to 8.8 cm and d2 parameters take the values of 25, 100, 200 and 500 mm. The permittivity results for the different values are exhibited in Figure 4-13 over 1.5-3 GHz bandwidth.

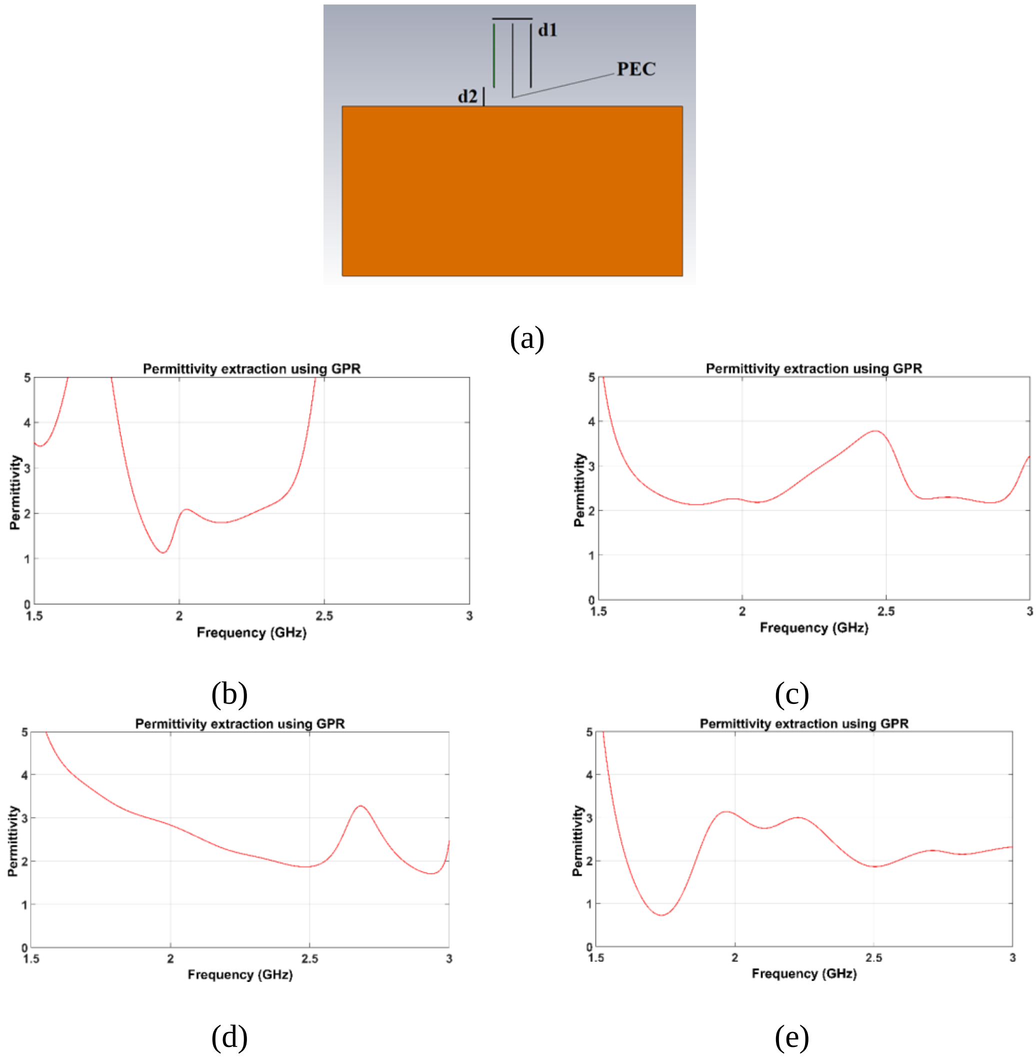

Figure 4-13 (a) GPR system with reflector, (b) extracted permittivity d1=88 mm, d2=25 mm, (c) extracted permittivity d1=88 mm, d2=100 mm, (d) extracted permittivity d1=88 mm, d2=200 mm, (e) extracted permittivity d1=88 mm, d2=500 mm

4.4.6 Two antennas with reflector first configuration 1.5-10 GHz

In this case, we implement the simulation over the complete bandwidth from 1.5 to 10 GHz. The selected parameters here are 8.8 cm for d1 and 10 cm for d2. The extracted permittivity is shown in Figure 4-14.

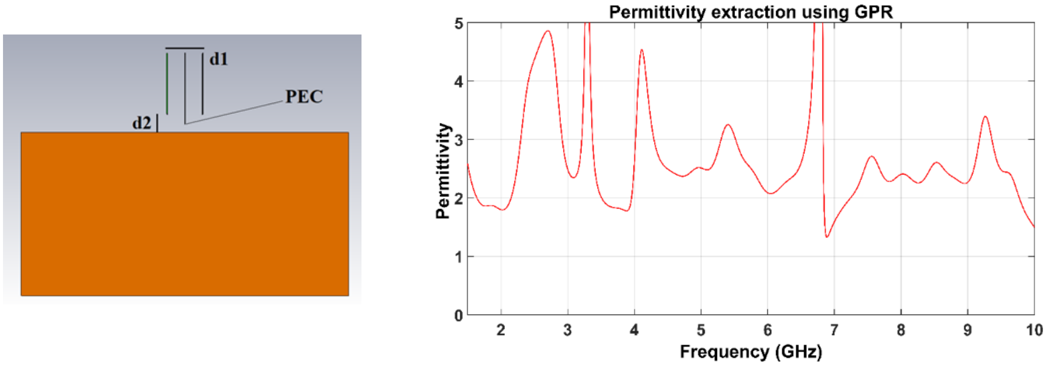

Figure 4-14 Extracted permittivity, d1=88 mm, and d2= 100 mm

4.4.7 Two antennas without reflector second configuration d2 variation effect

The second configuration which is mentioned in the title means that the two antipodal Vivaldi antennas are cascaded in the same plane as shown in Figure 4-15.

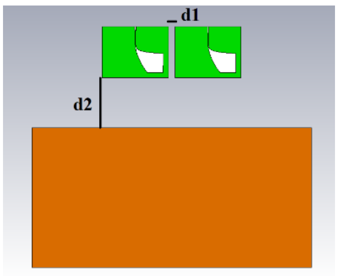

(a)

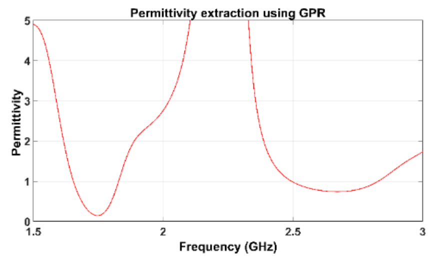

(b)

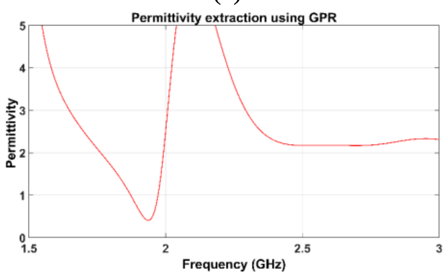

(c)

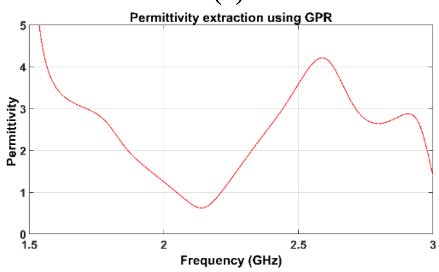

(d)

Figure 4-15 (a) GPR system without reflector second configuration, (b) extracted permittivity d1=20mm d2=50mm, (c) extracted permittivity d1=20mm d2=100mm, (d) extracted permittivity d1=20mm d2=200mm

The effect of the d2 parameter is studied here by varying its value from 50 mm to 200 mm, while d1 fixed to 2 cm. the extracted permittivity is also displayed in Figure 4-15.

4.4.8 Two antennas without reflector second configuration 1.5-10 GHz

The first configuration is simulated here over the entire bandwidth from 1.5 to 10 GHz. The separation distance between the antennas is 2 cm and the distance between the antennas and the soil surface is 15 cm. Figure 4-16 plots the extracted permittivity using the GPR system.

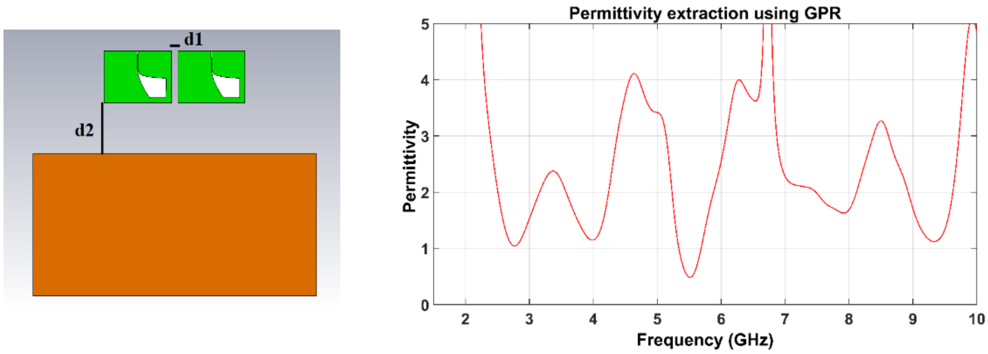

Figure 4-16 Extracted permittivity d1=20 mm d2=150 mm

4.4.9 Two antennas with rotating angle effect simulated with frequency-domain solver

In this case, the antennas are placed in the first configuration form but with a tilted angle of 40.5^0 as shown in Figure 4-17. The distance between the reflector and the soil surface is 75 mm. The simulation is performed over the 1.5-3 GHz bandwidth and the extracted permittivity is displayed in Figure 4-17

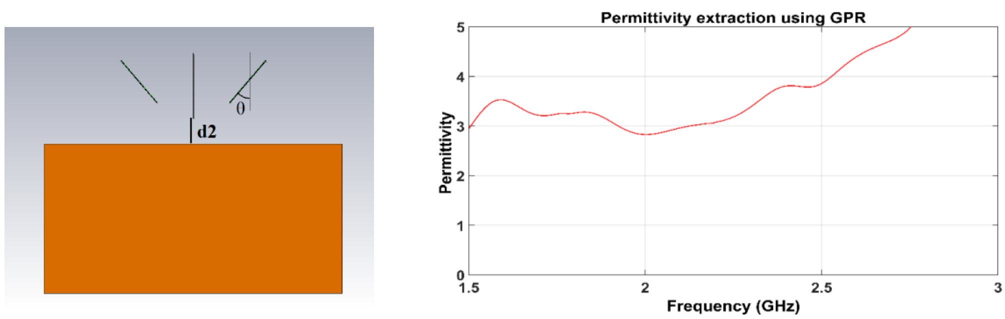

Figure 4-17 Extracted permittivity angle $=40.5^0$, d2=75 mm

There is a technical problem in the EM software simulator in the time domain when we are running this configuration. The excitation wave port can not be unaligned with the coordinate system. So, the simulation was done with the frequency domain solver with the aim of skipping this obstacle. We should mention here that the frequency domain solver in our case has several disadvantages such as the long run time and the week accuracy. Due to that the simulation study that intentions to obtain the optimum angle is stopped.

4.5 PERMITTIVITY EXTRACTION USING TWO ANTIPODAL VIVALDI ANTENNAS OPERATE WITHIN 12-18 GHZ RANGE

From the observation of the previous extracted permittivity results, we can say that with this inaccuracy of extraction the system did not achieve its goals in permittivity retrieval and this limitation is not a strange behavior since we still work with relatively low-frequency range. Hence, another GPR system is designed in order to enhance the permittivity extraction accuracy. The new system is based on the use of an antipodal Vivaldi antenna which covers higher frequency band (12-18 GHz). It is expected to get better extraction efficiency since we are going higher in the frequency.

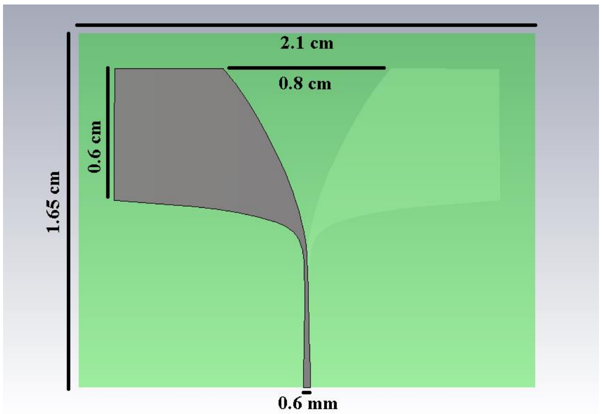

Figure 4-18 Dimensions of the second designed antipodal Vivaldi antenna

Figure 4-18 exhibits the dimensions of the new antennas. While Figure 4-19 displays the reflection coefficient S_{11} of the antipodal Vivaldi antenna which proves an operational frequency bandwidth from 12 GHz till 18 GHz.

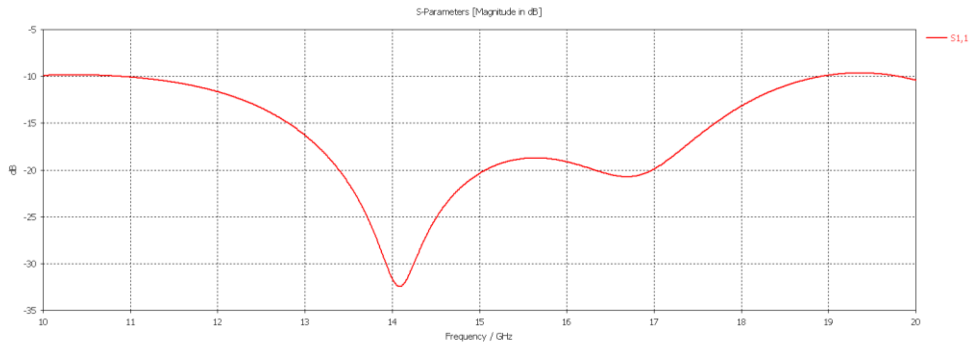

Figure 4-19 The simulated reflection coefficient result of the antenna

The far-field radiation pattern of the antenna at 15 GHz is presented in Figure 4-20.

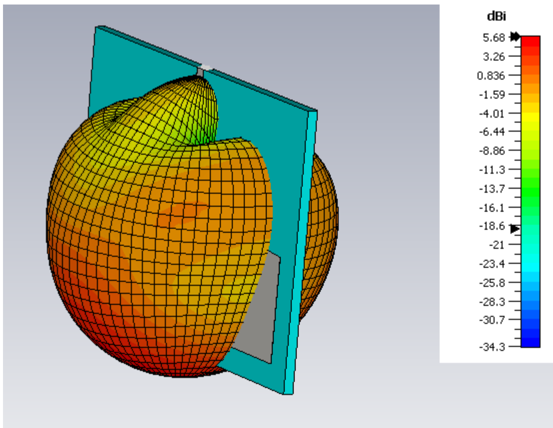

Figure 4-20 Farfield Radiation pattern at 15 GHz

4.5.1 Two antennas without reflector, d1 variation effect

In the first case of this numerical study, the antennas are placed in the first configuration form without a reflector isolates them. The separation distance represented by the parameter d1 is tuned here with two values 3 and 5 cm. While the soil surface to antennas distance is fixed to 5 cm. The extracted permittivity is plotted in Figure 4-21.

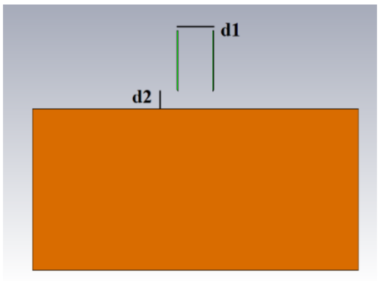

(a)

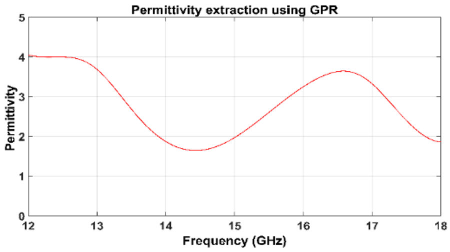

(b)

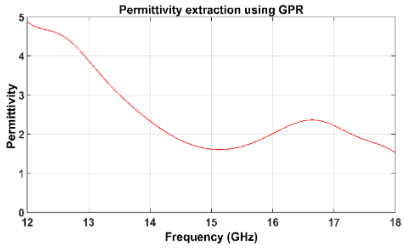

(c)

Figure 4-21 (a) GPR system without reflector first configuration, (b) extracted permittivity d1=30 mm, d2=50 mm, (c) extracted permittivity d1=88 mm, d2=50 mm

4.5.2 Two antennas with reflector, d1 variation effect

Now the antennas are separated by a reflector and the d1 parameter value is changed to take the values of 10, 30, 50 and 88 mm. Where the value of d2 parameter is fixed to 100 mm. The results of the extracted permittivity using the GPR system with this scenario are shown in Figure 4-22. The results prove an enhancement in the permittivity extraction accuracy especially in the case of d1=50 mm and d2=100 mm.

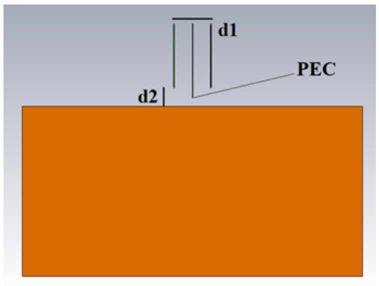

(a)

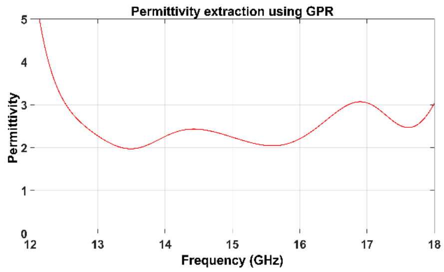

(b)

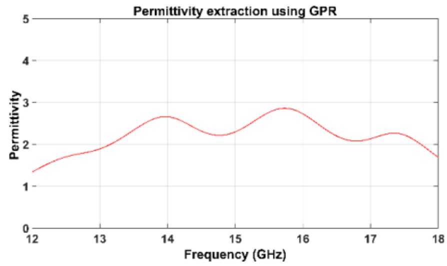

(c)

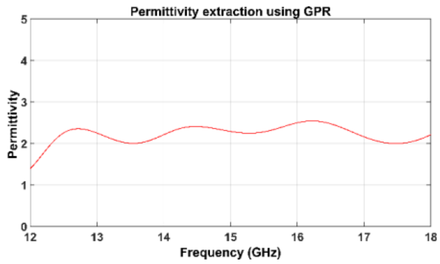

(d)

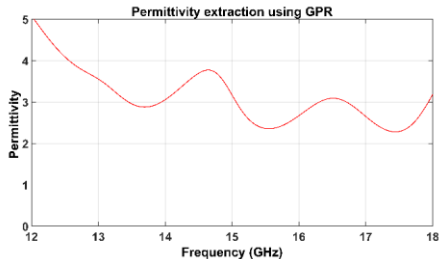

(e)

Figure 4-22 (a) GPR system with reflector, (b) extracted permittivity d1=10, d2=100, (c) extracted permittivity d1=30, d2=100, (d) extracted permittivity d1=50, d2=100, (e) extracted permittivity d1=88, d2=100

4.5.3 Two antennas with reflector, d2 variation effect

The variation effect of the d2 parameter is studied here. Two antipodal Vivaldi antennas were placed in the first configuration form and separated by a reflector. Then, d1 is fixed to 88 mm while d1 takes 50, 100, 150 and 200 mm values. The extracted permittivity is exhibited in Figure 4-23. Taking into consideration the results presented in subsections 4.5.2 and 4.4.5, we can select the optimal configuration parameters of the GPR system. The selected parameters are d1=50 mm and d2=100 mm.

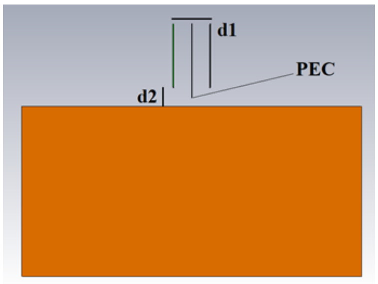

(a)

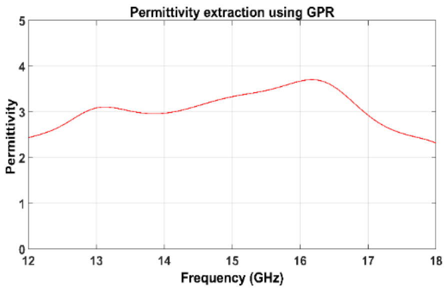

(b)

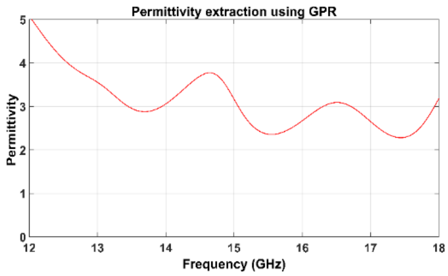

(c)

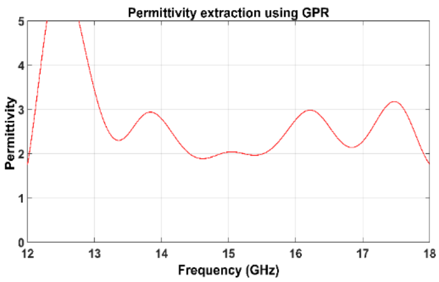

(d)

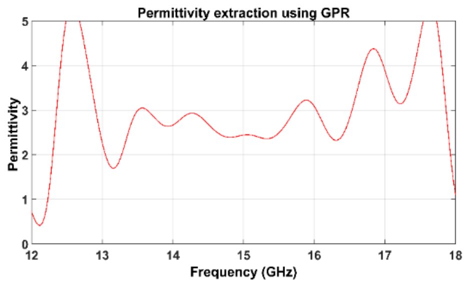

(e)

Figure 4-23 (a) GPR system with reflector, (b) extracted permittivity d1=88mm d2=50mm, (c) extracted permittivity d1=88mm d2=100mm, (d) extracted permittivity d1=88 d2=150, (e) extracted permittivity d1=88 d2=200

4.5.4 Optimal configuration for antipodal Vivaldi antennas with permittivity variation effects

To validate the optimal configuration that is found for the GPR system, we tried to simulate the optimal parameters for extracting different permittivity values (2.5, 5 and 10). The results below show that the use of the antipodal Vivaldi antennas for permittivity extraction is having acceptable accuracy for low permittivity and low accuracy for high permittivity.

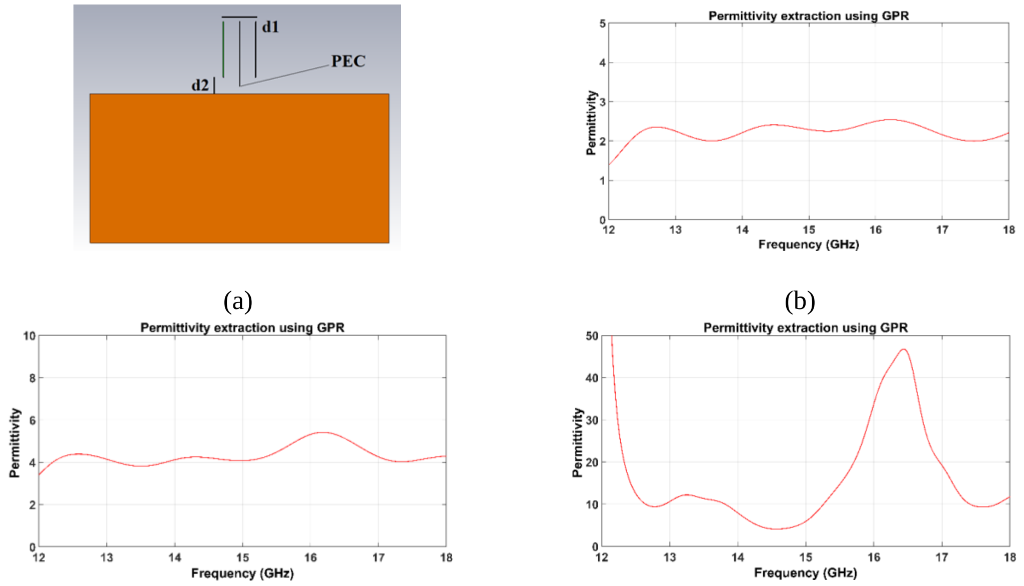

(a) (b)

(c) (d)

Figure 4-24 (a) GPR system with reflector first configuration, (b) extracted permittivity d1=50 mm, d2=100 mm, permittivity= 2.5, (c) extracted permittivity d1=50 mm, d2=100 mm, permittivity= 5, (d) extracted permittivity d1=50 mm, d2=100 mm, permittivity=10

4.6 PERMITTIVITY EXTRACTION USING TWO HORN ANTENNAS OPERATE WITHIN 12-18 GHZ RANGE

In the preceding simulated study, the extracted permittivity results using the antipodal Vivaldi antenna was not convinced enough. Therefore, a horn antenna was designed to be used in the GPR system instead. The horn antenna has higher directivity and power gain. The dimensions of the designed horn antenna are given in Figure 4-25.

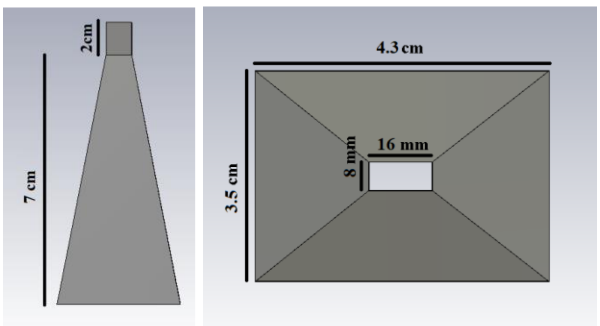

Figure 4-25 Dimensions of the designed horn antenna

The S_{11} response of the horn antenna is plotted in Figure 4-26. This antenna can work properly over the whole bandwidth from 12 till 18 GHz and this is considered when S_{11} stays below -10 dB.

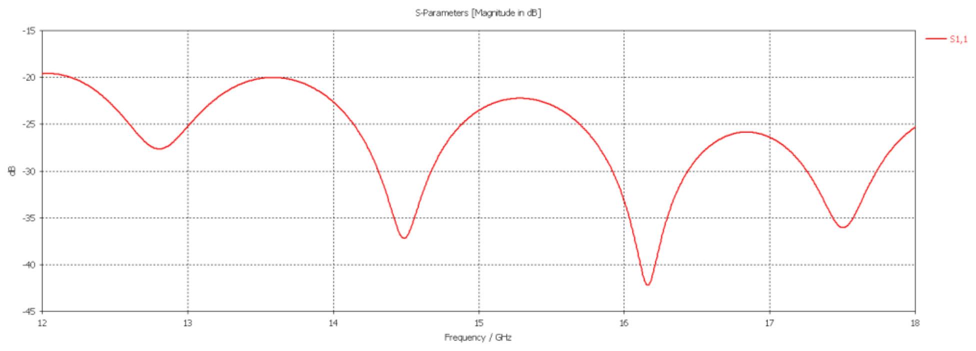

Figure 4-26 The simulated reflection coefficient result of the horn antenna

The far-field radiation pattern of the horn antenna at 15 GHz is displayed in Figure 4-27. The directivity property of the horn antenna lets the emitted EM wave to be focused on a smaller soil area.

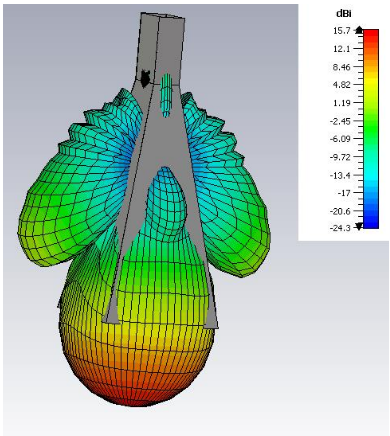

Figure 4-27 Farfield Radiation pattern at 15 GHz

4.6.1 Two horn antennas, and d2 effect

In this simulation case, two horn antennas were put above the ground surface that has a permittivity of 2.5. The antennas are placed away from each other 5 cm. where the distance between the antennas aperture and soil surface is tuned (d2= 50, 200, 300 and 400 mm). The extracted permittivity result for different values of d2 is shown in Figure 4-28. After the simple analysis of the obtained results, we can say that the extracted permittivity accuracy becomes satisfied when d2 is 300 mm and higher. And this distance might belong to the far-field range condition of the horn antenna.

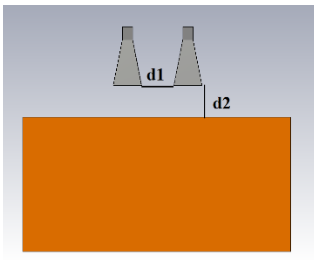

(a)

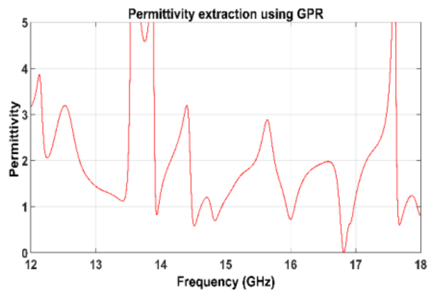

(b)

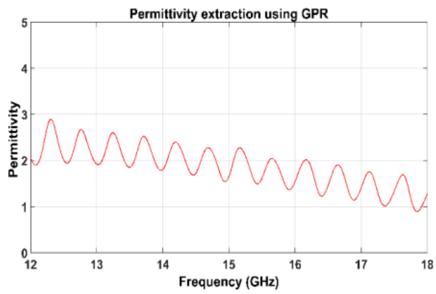

(c)

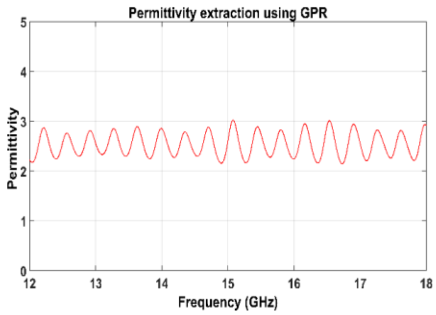

(d)

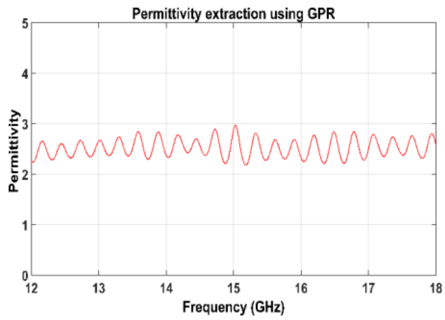

(e)

Figure 4-28 (a) GPR system, (b) : d1=50 mm, d2=50 mm permittivity= 2.5, (c) d1=50 mm, d2=200 mm, permittivity= 2.5, (d) d1=50 mm, d2=300 mm, permittivity= 2.5, (e) d1=50 mm, d2=400 mm, permittivity= 2.5

The incident electromagnetic wave to the soil surface is considered as a plane wave if the following condition is satisfied [10]:

$$d_2 > \frac{2D^2}{\lambda} \tag{4.8}$$

Where λ is the wavelength of the operating electromagnetic wave and D is the largest dimension of the antenna aperture. In our case the largest distance is the diagonal of the horn aperture which is 56 mm. So, at 12 GHz d_2 should be larger than 250 mm that explains why the 300 mm distance gives a more stable result.

4.6.2 Two horn antennas, d2 effect

Now, we studied again the effect of the parameter d2 on the permittivity extraction but with a different value of permittivity. The permittivity of the soil is set to 10. Here the distance between the antennas is also 5 cm. While the distance between the antennas and soil surface is changed to take the values of 50, 100 and 300 mm. The extracted permittivity is given in Figure 4-29. The results show acceptable accuracy when the d2 parameter is 300 mm and that agrees with the precedent observation in subsection 4.6.1.

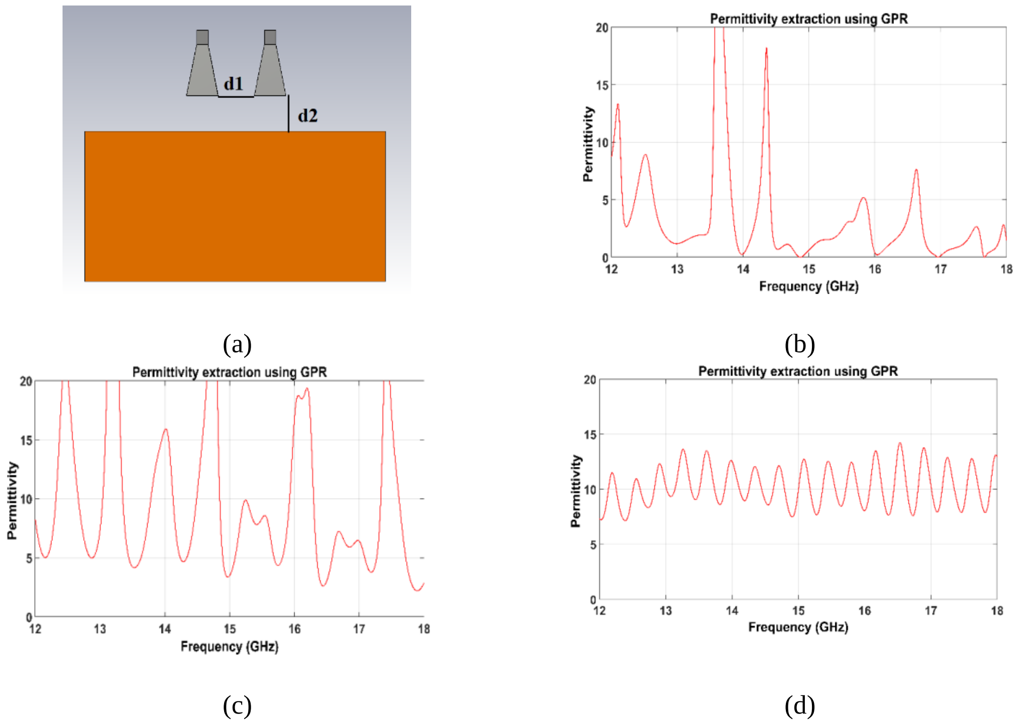

Figure 4-29 (a) GPR system without reflector first configuration, (b) d1=50 mm, d2=50 mm, permittivity= 10, (c) d1=50 mm, d2=100 mm, permittivity= 10, (d) d1=50 mm, d2=300 mm, permittivity= 10

4.6.3 Two horn antennas, d1 effects

In the last case, we simulate the effect of the d1 parameter on the extracted permittivity by varying its value (10, 50 and 80 mm). In addition, the distance between the antennas and the soil surface is fixed to 300 mm. The permittivity of the soil is given now as 2.5. The extracted permittivity using the GPR system is exposed in Figure 4-30. The results show that the separation distance between the antennas has no serious effect and that is due to the high directivity of the horn antenna.

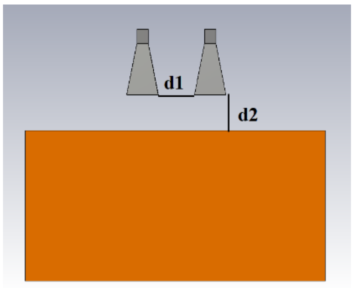

(a)

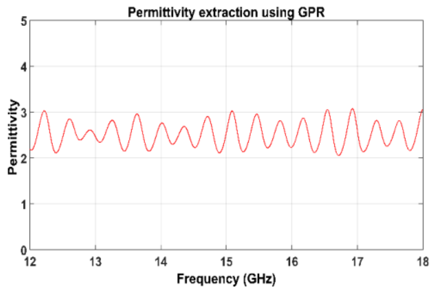

(b)

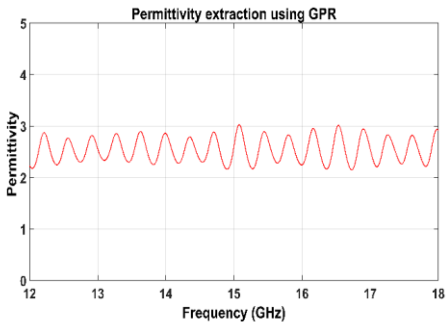

(c)

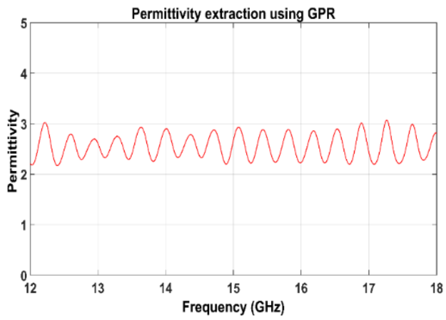

(d)

Figure 4-30 (a) GPR system with horn antenna first, (b) d1=10 mm, d2=300 mm, permittivity= 2.5, (c) d1=50 mm, d2=300 mm, permittivity= 2.5, (d) d1=80 mm, d2=300 mm, permittivity= 2.5

4.6.4 Permittivity filtering

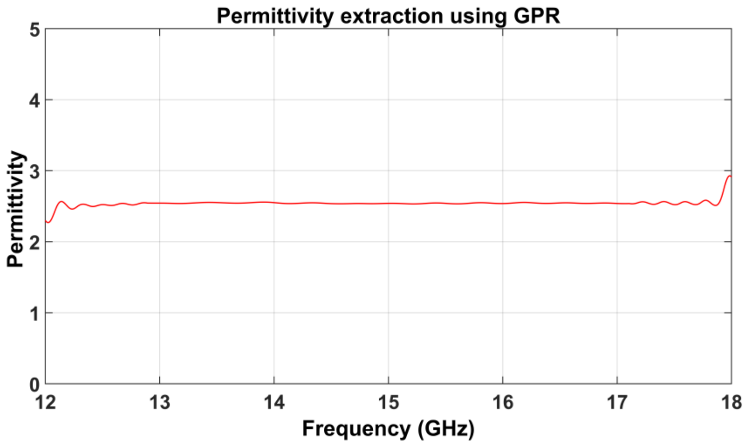

Figure 4-31 Filtered permittivity

The extracted permittivity can be filtered using a simple filter. A smoothing filter was applied to the extracted permittivity and the result is displayed in Figure 4-31. The result is very convincing and proves how the proposed configuration of the GPR system becomes efficient in permittivity extraction.

4.7 PERMITTIVITY EXTRACTION MEASUREMENT

Unfortunately the setup used in the simulation is not available to do an experimental validation, instead another setup used for permittivity extraction measurement based on Cayenne UWB radar and robotic rail as shown in Figure 4-32 Radar test setup.

Figure 4-32 Radar test setup

This radar can measure the reflected signal in voltage versus time. So relying on equation (4.7) the permittivity of the soil could be extracted experimentally after two measurements configuration.

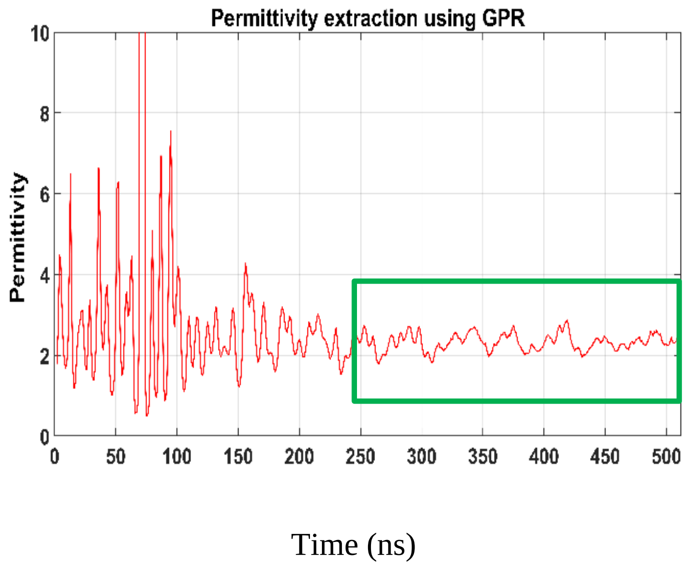

Figure 4-33 measured permittivity using a time domain ground penetrating radar

The figure above displayed the measured permittivity at a single position versus time. it is noticed that after a certain time the permittivity becomes relatively stable (in the green rectangular) that is due to the absence of the direct coupling after this time.

4.8 CONCLUSION

In this chapter, a non-destructive method for permittivity extraction is described theoretically and implemented numerically and experimentally for the application of ground characterization. The use of the GPR system in permittivity extraction is studied with different types of antennas and over different frequency ranges. The higher frequency range shows better accuracy in permittivity estimation, and the horn antennas exhibit higher efficiency in permittivity retrieval compared to the antipodal Vivaldi ones. In addition, optimal parameters for the finest GPR configuration were proposed for the measurement of permittivity.

4.9 REFERENCES

[1] Fishel, Marie, Phillip Koehn, and Erik Rosen. "Comparisons of ring resonator relative permittivity measurements to ground penetrating radar data." In *Detection and Sensing of Mines, Explosive Objects, and Obscured Targets XIX*, vol. 9072, p. 90720O. International Society for Optics and Photonics, 2014.

[2] Pozar, David M. Microwave engineering. John Wiley & Sons, 2009.

[3] Hammoud, Bilal, Fabien Ndagijimana, Ghaleb Faour, Hussam Ayad, Majida Fadlallah, and Jalal Jomaah. "Reflection-coefficient experimental extraction from S21-parameter for radar oil-spill detection application." (2018).

[4] N. Ganchuluun, "Design of GPR system for Dielectric Constant Measurement," [online]. Available: *http://magnet.cneas.tohoku.ac.jp/satolab/theses/gan_master.pdf*

[5] A. Lalagüe, "Use of Ground Penetrating Radar in quality assurance of new asphalt pavements," 2014. [Online]. Available: *http://www.nvfnorden.org/library/Files/Utskott-och-tema/Belaggning/FoU/Silkeborg_DK2014/NO FoU 2014 Radar in quality assurance of new thickness pavements Lalagüe.pdf.*

[6] Huisman, Johan Alexander, Susan Sharpess Hubbard, J. David Redman, and A. Peter Annan. "Measuring soil water content with ground penetrating radar." *Vadose zone journal* 2, no. 4 (2003): 476-491.

[7] Guo, Chen, Li Zhao, Yan Chen, Wei Li, and Richard C. Liu. "Extraction of the pavement permittivity and thickness from measured ground-coupled GPR data using a ground-wave technique." *IEEE Geoscience and Remote Sensing Letters* 14, no. 3 (2017): 399-403.

[8] Fishel, Marie, Phillip Koehn, and Erik Rosen. "Comparisons of ring resonator relative permittivity measurements to ground penetrating radar data." In *Detection and Sensing of Mines, Explosive Objects, and Obscured Targets XIX*, vol. 9072, p. 90720O. International Society for Optics and Photonics, 2014.

[9] Gibson, P. J. "The vivaldi aerial." In *1979 9th European Microwave Conference*, pp. 101-105. IEEE, 1979.

[10] Li, Li, Xinlin Xia, Yu Liu, and Tao Yang. "Wideband balanced antipodal Vivaldi antenna with enhanced radiation parameters." *Progress In Electromagnetics Research* 66 (2016): 163-171.

[11] Chen, Lin-Feng, C. K. Ong, C. P. Neo, V. V. Varadan, and Vijay K. Varadan. *Microwave electronics: measurement and materials characterization*. John Wiley & Sons, 2004.

Chapter 5: Novel Approach to Landmine Detection

Contents

5.1 INTRODUCTION

Diverse methods for landmine detection were described in Chapter 1. GPR is one of the most efficient methods that currently uses. Several limitations are existing in the GPR method. In the following relying on several references, we will indicate some points for showing these limitations.

In general, the GPR is inefficient in wet soil and its performance varies with the variation in the type of soil [1]. Using the GPR in inhomogeneous soil that contains clutters (e.g. stones, roots) will lead to an increase in the false alarm [2]. Another issue is related to the detection failure of small mines buried at shallow depth due to the reflection response interfering between the soil surface and the landmine [3]. In addition, EM waves at higher frequencies are strongly attenuated within a certain type of conductive and wet soils such as clay. On the other side, in very dry soil case the permittivity contrast between the dry soil and the plastic casing of the mines is low and therefore these types of landmines may not be detected [4].

It is known that there is no perfect method for all soil conditions, for that reason two methods can be combined to enhance the detection process. As an example of this combination is the use of the GPR and the metal detector simultaneously [5]. Even with this combination the limitations still affect the detection efficiency. So, we are writing this chapter for proposing a novel approach that could be useful in solving the weak points of the GPR method.

5.2 NEW APPROACH CONCEPT

Due to GPR limitations and its negative influence on the landmines detection process, a new approach for mine searching is presented here for covering these limitations. The idea is to sense directly the effective permittivity of the scanned area instead of collecting the reflected signals and doing complicated processing. In this way, we can detect the effective permittivity signature of buried landmines at a shallow depth where the traditional use of GPR fails. The proposed concept could be very efficient in wet soil since the permittivity contrast between the landmines and the surrounding soil is larger.

The effective permittivity signature of the buried landmines is related to its size and the frequency range that we are working on. In order to extract the effective permittivity of buried landmines, two different methods are suggested in this work. The first method is the use of the TEM cell in the effective permittivity extraction of landmines as demonstrated in Chapter 3. There is a bandwidth limitation in this method since the TEM cell has a limitation in its usable frequency range as explained in Chapter 3 also. The second method could be a real measurement extraction using the GPR system or another permittivity sensor as shown in Chapter 4. We should mention here that the second method has the advantage of extracting the effective permittivity at higher frequencies.

5.3 HOMOGENIZATION CONCEPT

Inhomogenous material is one of the complicated cases that you can deal with. Taking into account the EM interactions with each element of the overall mixture can lead to making the analysis more complex and time-consuming. Hence, it is possible to use another concept to overcome the inhomogeneity problem based on the homogenization concept.

The homogenization concept is the replacement ability of any inhomogeneous material sample by its alternative homogeneous material sample that has the same effective permittivity (same response) [6].

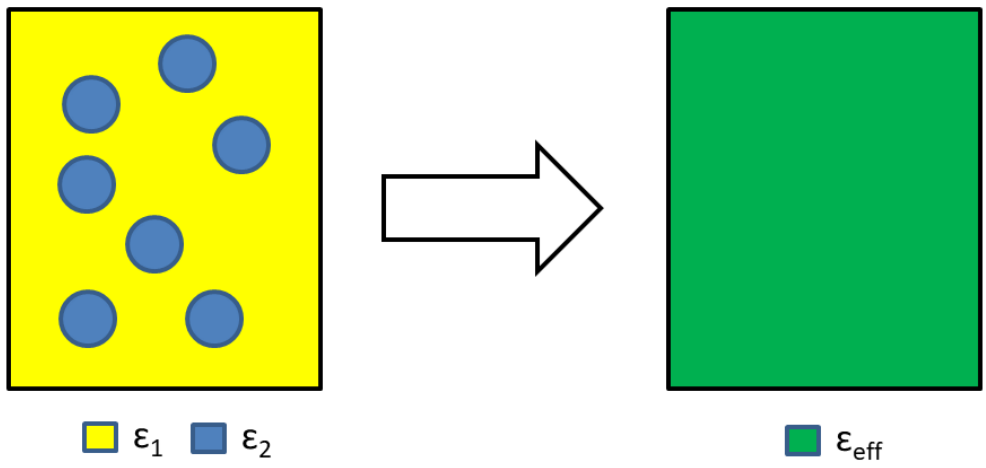

Figure 5.1 Homogenization concept applied to replace inhomogeneous material by its alternative effective material properties

For example, Figure 5.1 shows a composite material sample consists of two different permittivities ε_1 and ε_2, then by implementing the homogenization concept we can replace the composite material by a homogeneous material that has the same response. The effective permittivity (ε_{eff}) here is a function of (ε_1 and ε_2) but we do not have to find this relation since we are able to measure it directly using the proposed methods in earlier.

For our application, the inhomogeneous material represented by the landmine with its surrounding soil. In chapter 3 the effective permittivity of this mixture (landmine, soil) was extracted using the TEM cell.

So, make use of the homogenization concept in addition to the extracted effective permittivity we can replace the complex material structure (landmine, soil) by a homogeneous material.

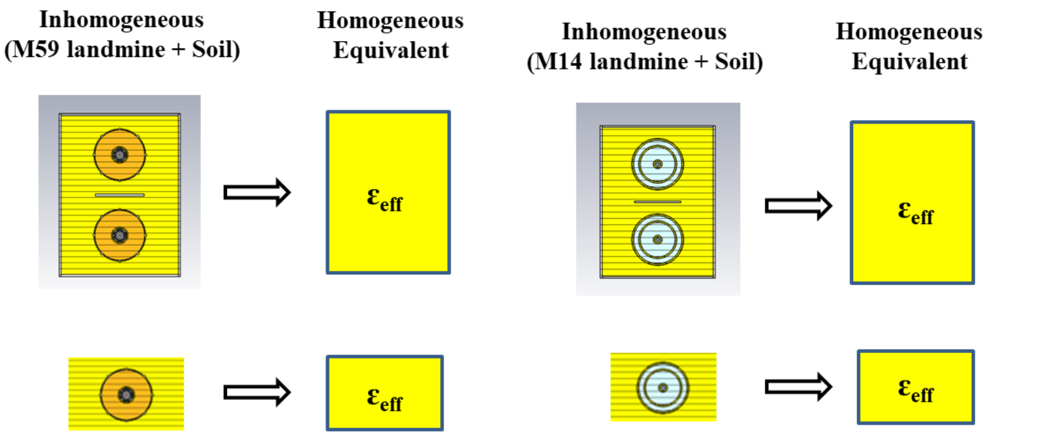

Figure 5.2 Landmines/soil homogenization implementation relying on the effective permittivity that computed using TEM cell

5.4 NUMERICAL VALIDATION OF THE NOVEL APPROACH

With the aim of validating the efficiency of the novel approach in landmine detection, a numerical study was implemented with difficult minefield conditions where the traditional use of GPR fails. The difficult conditions are represented by placing the landmine at a shallow depth in wet soil. These conditions are referring to the limitation points of the GPR method that are reported in the introduction of this chapter.

Moreover, For avoiding the long run time of the simulation with the presence of the complex landmine model and with the relatively high permittivity of the wet soil, the landmines with its surrounding environment were replaced by their alternative homogeneous material that already studied using the closed TEM cell. The alternative homogeneous material is represented in yellow color as shown in Figure 5.3 and becomes the target that we are looking for since it has the same effective permittivity of the landmine.

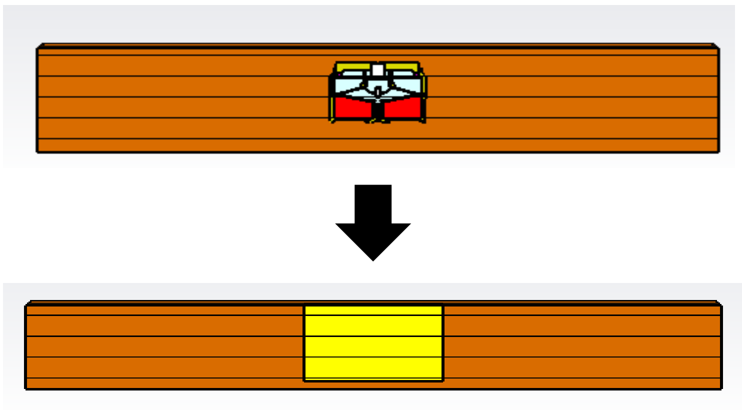

Figure 5.3 Replacing buried M14 landmine by its alternative homogeneous material

Using a 3D electromagnetic simulator software, the test setup for the detection scenario was modeled as displayed in Figure 5.4. The testbed consists of soil denoted by the brown color that has 20 as permittivity value for representing the wet soil condition, the target denoted by the yellow color which has a permittivity value of 17, and that belonging to the effective permittivity of the landmine that extracted using the TEM cell in Chapter 3. Furthermore, two horn antennas were placed in the optimal parameters configuration that has been studied in Chapter 4 with the intention of extracting accurately the permittivity of the area under test. In addition, the boundary conditions were taken care of to reflect the fact the soil model edges (sides and bottom) are continuing to infinite. In this way, we can eliminate any undesired reflections from boundaries.

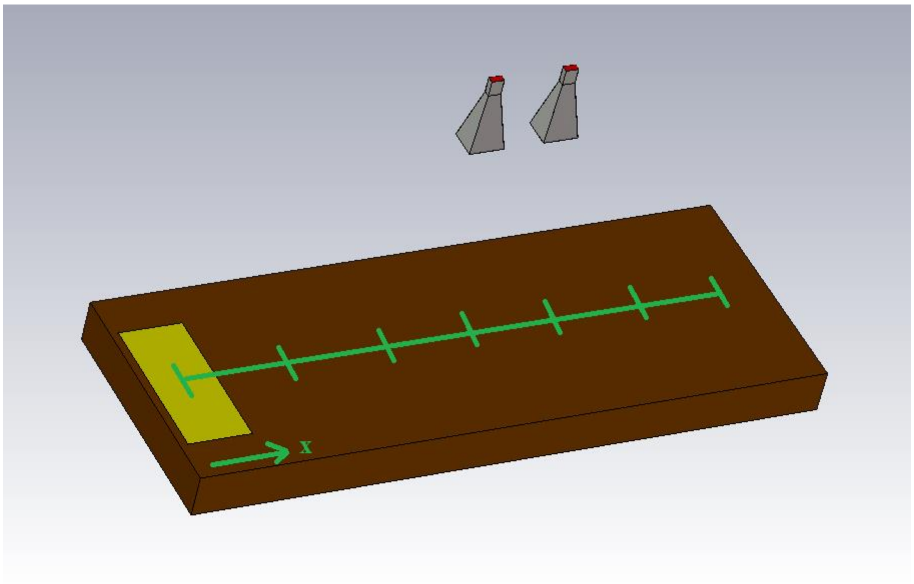

Figure 5.4 The simulated test setup for landmine detection scenario using GPR system

Now the target starts moving from -35 cm to 35 cm in the *x*-axis direction. The target takes 7 positions as marked in green color in the figure above. At each position, the GPR system (two antennas) will extract the permittivity of the scanned area following the procedure in Chapter 4. In this study we are moving the target instead of moving the antennas because in this action less size is needed to represent the test setup model, as a result, shorter simulation run time is required.

The extracted permittivity result versus *x* position is shown in Figure 5.5. For each position, the extracted permittivity is the average of the permittivity values at all simulated frequencies. By having a look at the presented permittivity result, the GPR system is reading 20 as permittivity value for the area under the spot and that occurs when the target is away from the antennas. While the GPR system reads lower permittivity value when the target directly existed under the antennas at position zero.

So, relying on this drop in the extracted permittivity we can detect the presence of buried landmines. This drop is related directly to the permittivity contrast between the mine and its surrounding soil. When the permittivity contrast increases the drop response will clearly found and when the permittivity contrast decreases this drops will decrease.

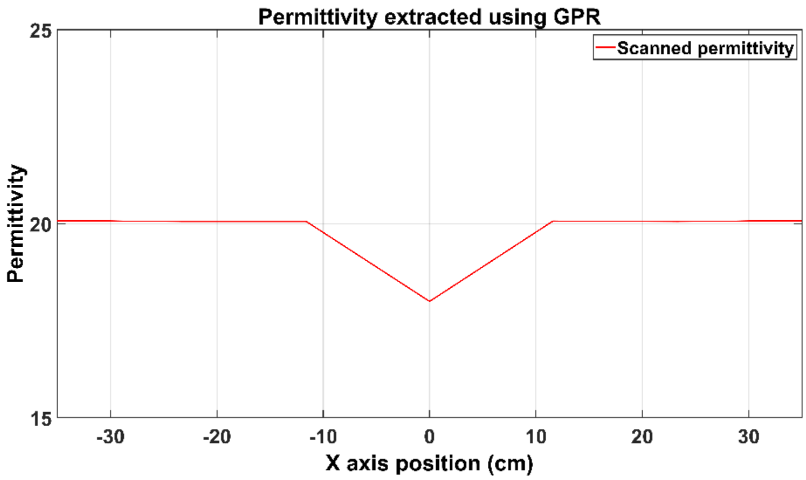

Figure 5.5 The extracted permittivity versus x position

Many cases and scenarios still have to be studied for experimental validation of the proposed method. Nevertheless, one of the potential difficult cases that may face the proposed method is the discrimination between mine and clutter (e.g., stone, roots, and etc.). Fortunately, natural clutter such as stones and woods can absorb water [74]. On the other side, the landmine casing is made of plastic or metal and will not absorb water. That is mean the differentiation between landmine and natural clutter is still possible.

5.5 PROPOSED PERMITTIVITY SENSORS

In the current study, the GPR system was employed for permittivity extraction but other permittivity sensors can be developed or used. In this subsection, three different sensors were proposed. These kinds of sensors can be mounted on drones or vehicles for scanning the contaminated area within a faster time in compered to the existing demining method. We should mention here that the novel approach is open in its implementation with any new efficient permittivity sensor.

5.5.1 One horn antenna

One horn antenna can be used as a permittivity sensor by relating the reflection coefficient of the antenna to the relative permittivity of the MUT. The high gain and high directivity specifications of the horn antenna can play an important role in permittivity extraction efficiency since higher power may be needed in such soil probing applications.

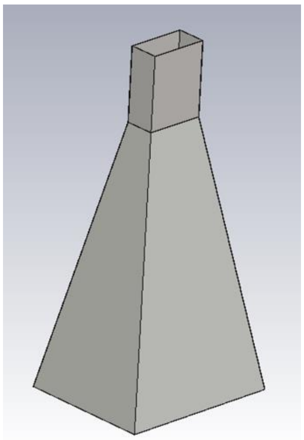

Figure 5.6 Horn antenna for permittivity measurement

5.5.2 Split ring resonator

Resonator sensors could be used also for permittivity measurement. Usually, the split ring resonator is widely used for permittivity measurement of liquid or solid material. This method has a high accuracy of permittivity extraction and could be an interesting sensor to be used with the proposed method for landmine detection.

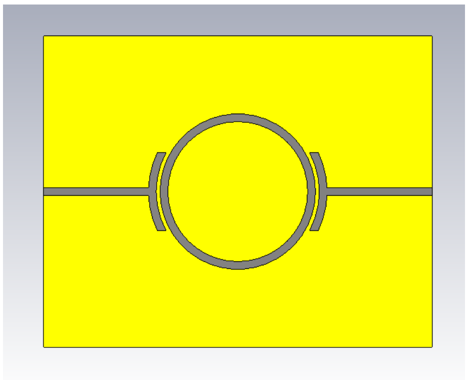

Figure 5.7 Split ring resonator for permittivity measurement

5.5.3 Parallel trace

Another type of permittivity probe could be a planar parallel trace. This kind of planar sensor changes its reflection response due to the presence of any MUT that will interact with the electric field generated between the traces.

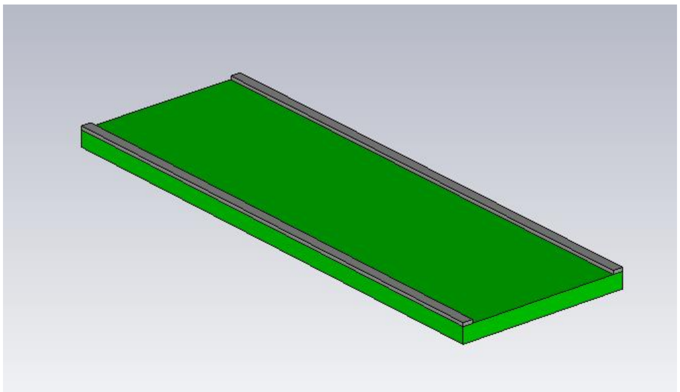

Figure 5.8 Parallel traces probe for permittivity measurement

5.6 CONCLUSION

I this chapter a novel approach for mine searching is proposed. The new concept is developed for overcoming several limitations exist in the traditional GPR method. The new method aims to detect the landmine based on its effective permittivity signature. The effective permittivity signature is studied in Chapter 3 but it can be measured directly using the proposed permittivity measurement systems in a real minefield. The detection scenario was numerically validated with the use of the GPR system for permittivity extraction.

5.7 REFERENCES

[1] Bhope, Pankaj C., and Anjali S. Bhalchandra. "Various Landmine Detection Techniques: A Review." *International Journal of Innovative Research in Science, Engineering and Technology* 4, no. 6 (2015).

[2] Abujarad, Fawzy. "Ground penetrating radar signal processing for landmine detection." (2007).

[3] Cardona, Lorena, Jovani Jiménez, and Nelson Vanegas. "Landmine detection technologies to face the demining problem in Antioquia." *Dyna* 81, no. 183 (2014): 115-125.

[4] Kasban, H., O. Zahran, Sayed M. Elaraby, M. El-Kordy, and FE Abd El-Samie. "A comparative study of landmine detection techniques." *Sensing and Imaging: An International Journal* 11, no. 3 (2010): 89-112.

[5] Druyts, P., Y. Yvinec, and M. Acheroy. "Relating soil properties to performance of metal detectors and ground penetrating radars." In *Using Robots in Hazardous Environments*, pp. 189-220. Woodhead Publishing, 2011.

[6] R. C. Rumpf, “Homogenization and Parameter Retrieval,” pp. 124–140, 2018.

[7] Bapna, P., and S. Joshi. "Measurement of dielectric properties of various marble stones of Mewar region of Rajasthan at X-band microwave frequencies." *International Journal of Engineering and Innovative Technology (IJEIT)* 2, no. 7 (2013): 180-186.

General Conclusion

Different technological topics were studied and discussed in this thesis with the aim of enhancing the landmine detection process. The landmine problem was clearly defined in order to show the humanitarian motivation behind this work. In addition, the state of the art of the landmines detection methods was introduced with an indication of their advantages and limitations. Under the fact that GPR system becomes popular in use for humanitarian demining work, an overview of its operation principle and its limitations and advantages were reported. Since the GPR system is an EM based method, the interaction behavior between the EM wave and the matter should be studied if any enhancement was expected to be found.

In chapter two, the microwave methods for material characterization were presented in detail to be as good reference material. Different calibration and conversion methods were described and implemented. Also, two uncalibrated methods were given to overcome the calibration complexity in some measurement situations. Furthermore, several materials related to our application were characterized such as plastic, sand, and soil. Based on chapter two the electromagnetic properties of dielectric materials that represent the behavior between an EM wave and matter become able to be measured.

In chapter three, TEM cell theory and design were introduced. The closed TEM cell was employed for the first time in the material characterization application. A new design of closed TEM cell was fabricated for providing the possibility to implement different calibration and conversion methods. Owing to the relatively big test space provided by the TEM cell different types of landmines surrounded by soil were effectively characterized. The extracted effective permittivity of the landmines with soil shows that the permittivity contrast increased in the wet soil condition.

In chapter four, the GPR system was numerically implemented and used for non-destructive permittivity extraction applications. The required theory was reported and the optimal configuration for using a GPR system for permittivity extraction was given after a parametric effect study.

In the fifth chapter, a novel approach for landmines detection was proposed based on the studies performed in the previous chapters. The new concept uses the effective permittivity of the target as a signature for detection. The new approach can cover some GPR limitations especially in the case of shallow depth mines in wet soil conditions. A detection scenario for buried landmine was numerically validated using the GPR system as a permittivity sensor. The proposed detection method can be implemented using other permittivity sensors which may have higher permittivity extraction precision.

At the end, several innovative ideas were presented in this work; first 3D printed low cost and lightweight TEM cell fabricated that can be used for EMC and EMI tests, first closed TEM cell for material characterization application was fabricated that might be useful in GPR and other applications, A novel approach to landmine detection was proposed which cover some GPR limitations in demining work. The most important thing in this work is the trying of making a scientific contribution to the demining work with the aims of saving lives.

Abstract

Landmines contamination is a widespread problem in many countries. Indeed, thousands of people around the globe are living in daily threats due to these hidden traps. The clearance process of the contaminated areas for humane purposes is known as humanitarian demining. Current demining methods are mostly manual and rely on metal detectors and ground penetrating radar (GPR). In some cases, the metal amount that exists in the landmine is very small and is not sufficient for being sensed by the metal detector. On the other side, the GPR can detect and locate the buried landmine in the soil relying on the fact that the reflected signal is related to the permittivity of the materials at interface. The GPR system needs complicated processing of the received signals to identify the presence of mine or not. One of the GPR disadvantages is its inability to detect the landmines at shallow depth. In addition, its detection efficiency is limited in the case of wet soil. The high cost and effort necessitate the work on related research topics that can enhance the existing demining techniques or even develop a newer one.

This Ph.D. research work aims to study the effective permittivity of the buried landmine with its surrounding soil. Knowing more information about the interaction between the electromagnetic wave and the buried target can be very useful to enhance the GPR detection process. In this work, the different methods of microwave material characterization were described in detail in order to provide the literature with a good material reference. The characterization of landmines implies the search for a suitable test fixture that can be used in effective permittivity extraction. Since the traditional transmission lines are not compatible in use with landmines characterization due to their material insertion complexity and size limitation, the transverse electromagnetic (TEM) cell was selected as the test fixture owing to its advantage in the size and material insertion easiness. In this research work, the use of the closed TEM cell for material characterization is attempted for the first time. A novel design for closed TEM cell is proposed, this design allows the implementation of the different material characterization techniques. The proposed TEM cell can be used to characterize both homogenous and inhomogenous (including landmines) materials. The effective permittivity of two different types of landmines was extracted using the proposed closed TEM cell technique. Correspondingly, the GPR system configuration and its use in permittivity extraction of soil are studied and implemented numerically. The optimal configuration of the GPR system is obtained after a parametric effects study for different cases and scenarios. The main disadvantage in the simulation study of the GPR system is the long run time, especially with the presence of the buried landmines which has a complex shape. Thus, make use of the homogenization concept, we can replace any inhomogeneous material by its alternative homogenous material which has the same response (has the same effective permittivity). So, instead of simulating the landmine with its surrounding soil we can simulate its homogenous material equivalence that has been studied in the TEM cell. In this way, we can reduce the time of the simulation. Furthermore, a novel approach for landmines detection is proposed in this work based on the effective permittivity signature. This method is dedicated to shallow depth detection of landmines and its detection efficiency increases in the case of wet soil, and that is covering the current GPR technique limitations.

Finally, this work opens new prospects for humanitarian demining research. And its promising results can lead to enhance detection technology, in other meaning a reduction in the loss of life.

Keywords: Material characterization, TEM cell, GPR, effective permittivity, landmines

Résumé

La contamination par les mines antipersonnel est un problème répandu dans de nombreux pays. En effet, des milliers de personnes à travers le monde vivent des menaces quotidiennes à cause de ces pièges cachés. Le processus de dépollution des zones contaminées à des fins humanitaires est appelé déminage humanitaire. Les méthodes actuelles de déminage sont principalement manuelles et reposent sur des détecteurs de métaux et un radar à pénétration de sol (GPR). Dans certains cas, la quantité de métal présente dans la mine terrestre est très petite et ne suffit pas pour être détectée par le détecteur de métal. De l'autre côté, le GPR peut détecter et localiser la mine enfouie dans le sol en s'appuyant sur le fait que le signal réfléchi est lié à la permittivité des matériaux à l'interface. Le système GPR nécessite un traitement compliqué des signaux reçus pour identifier la présence du mien ou non. L'un des inconvénients du GPR est son incapacité à détecter les mines terrestres à faible profondeur. De plus, son efficacité de détection est limitée dans le cas de sol humide. Les coûts élevés et les efforts nécessaires nécessitent des travaux sur des sujets de recherche connexes pouvant améliorer les techniques de déminage existantes ou même en développer de nouvelles.

Ce doctorat Les travaux de recherche visent à étudier la permittivité effective de la mine enfouie dans le sol environnant. Connaître plus d'informations sur l'interaction entre l'onde électromagnétique et la cible enterrée peut être très utile pour améliorer le processus de détection GPR. Dans ce travail, les différentes méthodes de caractérisation des matériaux à micro-ondes ont été décrites en détail afin de fournir à la littérature une bonne référence matière. La caractérisation des mines antipersonnel implique la recherche d'un dispositif d'essai approprié pouvant être utilisé pour l'extraction par permittivité effective. Étant donné que les lignes de transmission traditionnelles ne sont pas compatibles avec la caractérisation des mines antipersonnel en raison de la complexité de leur insertion de matériau et de leur taille limitée, la cellule électromagnétique transverse (TEM) a été choisie comme appareil d'essai en raison de son avantage en termes de facilité d'insertion de taille et de taille. Dans ce travail de recherche, l'utilisation de la cellule TEM fermée pour la caractérisation du matériau est tentée pour la première fois. Une nouvelle conception de la cellule TEM fermée est proposée. Cette conception permet la mise en œuvre des différentes techniques de caractérisation des matériaux. La cellule TEM proposée peut être utilisée pour caractériser des matériaux homogènes et non homogènes (y compris les mines terrestres). La permittivité effective de deux types différents de mines antipersonnel a été extraite à l'aide de la technique proposée de cellules TEM fermées. De manière correspondante, la configuration du système GPR et son utilisation dans l'extraction de permittivité du sol sont étudiées et mises en œuvre numériquement. La configuration optimale du système GPR est obtenue après une étude paramétrique des effets pour différents cas et scénarios. Le principal inconvénient de l'étude de simulation du système GPR est la longue durée de vie, en particulier avec la présence des mines terrestres enfouies qui ont une forme complexe. Ainsi, en utilisant le concept d'homogénéisation, nous pouvons remplacer n'importe quel matériau non homogène par son matériau homogène alternatif qui a la même réponse (a la même permittivité effective). Ainsi, au lieu de simuler la mine avec le sol qui l'entoure, nous pouvons simuler son équivalence matérielle homogène qui a été étudiée dans la cellule TEM. De cette façon, nous pouvons réduire le temps de la simulation. En outre, une nouvelle approche de la détection des mines terrestres est proposée dans ce travail, basée sur la signature de permittivité effective. Cette méthode est dédiée à la détection de mines terrestres à faible profondeur et que son efficacité de détection augmente dans le cas de sols humides, et couvre les limitations actuelles de la technique GPR.

Enfin, ce travail ouvre de nouvelles perspectives pour la recherche sur le déminage humanitaire. Et ses résultats prometteurs peuvent conduire à améliorer la technologie de détection, autrement dit à réduire le nombre de pertes de vies humaines.

Mots clés: Caractérisation des matériaux, cellule TEM, GPR, permittivité effective, mines terrestres